NASA Contractor Report 189127

Fluid Mechanics Experiments in Oscillatory Flow

Volume I–Report

J. Seume, G. Friedman, and T.W. Simon
University of Minnesota
Minneapolis, Minnesota

March 1992

Prepared for
Lewis Research Center
Under Grant NAG3–598

National Aeronautics and
Space Administration

DISCLAIMER

ABSTRACT

Results of a fluid mechanics measurement program in oscillating flow within a circular duct are presented. The program began with a survey of transition behavior over a range of oscillation frequency and magnitude and continued with a detailed study at a single operating point. Such measurements were made in support of Stirling engine development. Values of three dimensionless parameters, Re_{max}, Re_w, and A_R, embody the velocity amplitude, frequency of oscillation and mean fluid displacement of the cycle, respectively. Measurements were first made over a range of these parameters which included operating points of all Stirling engines. Next, a case was studied with values of these parameters that are representative of the heat exchanger tubes in the heater section of NASA's Stirling cycle Space Power Research Engine (SPRE). Measurements were taken of the axial and radial components of ensemble-averaged velocity and rms-velocity fluctuation and the dominant Reynolds shear stress, at various radial positions for each of four axial stations. In each run, transition from laminar to turbulent flow, and its reverse, were identified and sufficient data was gathered to propose the transition mechanism. Models of laminar and turbulent boundary layers were used to process the data into wall coordinates and to evaluate skin friction coefficients. Such data aids in validating computational models and is useful in comparing oscillatory flow characteristics to those of fully-developed steady flow.

Data were taken with a contoured entry to each end of the test section and with flush square inlets so that the effects of test section inlet geometry on transition and turbulence are documented.

The following is presented in two volumes. Volume I contains the text of the report including figures and supporting appendices. Volume II contains data reduction program listings and tabulated data (including its graphical presentation).

ACKNOWLEDGEMENTS

The following work was sponsored by the Lewis Research Center of NASA under grant NASA/NAG3-598. The authors thank the grant monitors, James Dudenhoefer and Roy Tew for their guidance.

Consultation on instrumentation and 3D graphics was provided by Robert Hain, the comparison of data to steady-flow correlations in this report was done by Terry Johnson and much of the document preparation was with the aid of Phillip Tuma and Amy Johnson.

CONTENTS VOLUME I

CONTENTS VOLUME II

NOMENCLATURE

Symbol	Units	Explanation
$A_R = \frac{2x_{m,max}}{l}$		Relative stroke or amplitude of fluid displacement
A^+		Empirical effective sublayer thickness for Van Driest model
$c_f = \frac{2u_*^2}{u_m^2}$		Skin-friction coeffificent (also = Fanning friction factor = Darcy friction factor ÷ 4)
D	m	Piston diameter
d	m	Duct inner diameter
f	sec^{-1}	Frequency
k_T		Correction factor for tangential cooling of hot-wire sensor
l	m	Duct length
P	bar	Fluid static pressure
p^+		Pressure gradient parameter
$\bar{p}$	bar	Average pressure
r	m	Cross-stream coordinate, measured from the duct centerline
R	m	Pipe inner radius
$Re_d = \frac{u_m d}{\nu}$		Reynolds number for steady flow, based on the duct diameter and the bulk-mean velocity
$Re_{max} = \frac{u_{m,max} d}{\nu}$		Reynolds number based on the duct diameter and the amplitude of the bulk-mean velocity
$Re_\omega = \frac{\omega d^2}{4\nu_o}$		Kinetic Reynolds number, or Valensi number
$Re_\delta = u_{m,max}\, \delta/\nu$		Reynolds number based opon Stokes layer thickness

Symbol	Units	Explanation
$Re_{\delta_2} = \delta_2 u_m / \nu 2$		Momentum thickness Reynolds number
s	m	Streamwise distance measured from open end of duct, or the stroke of the piston
$Str = \frac{\omega d}{u_{m,,max}} = \frac{4Va}{Re_{max}}$		Strouhal Number
t	sec	Time
T	℃	Fluid temperature
u	m/sec	Instantaneous velocity
$\overline{u}$	m/sec	Streamwise component of ensemble-averaged velocity
$u' = \sqrt{\overline{u'^2}}$	m/sec	Streamwise component of rms-velocity fluctuation
u_{eff}	m/sec	Effective cooling velocity
u_∞	m/sec	Freestream velocity
u_m	m/sec	Bulk-mean velocity
$u_{m,max}$	m/sec	Amplitude of the bulk-mean velocity
u_n	m/sec	Velocity component normal to sensor
u_T	m/sec	Velocity component tangential to sensor
$u_* = \sqrt{\frac{\tau_w}{\rho}}$	m/sec	Friction velocity
$u^+ = \frac{u}{u_*}$		Nondimensional velocity, in wall coordinates
$\overline{v}$	m/sec	Radial component of ensemble-averaged velocity
v'	m/sec	Radial component of rms-velocity fluctuation
V	volts	Transducer voltage
$Va = \frac{\omega d^2}{4\nu_o}$		Valensi number
$-\overline{u'v'}$	m^2/sec^2	Reynolds shear stress

Symbol	Units	Explanation
x	m	Streamwise distance, measured from drive end of duct
x_m	m	Amplitude of displacement of bulk fluid
y	m	Cross-stream coordinate, measured from the duct wall
$y^+ = \frac{yu_*}{\nu}$		Distance normal to the wall in inner coordinates
Greek		
$\alpha = \sqrt{Va}$		Womersely parameter
$\delta = (2\nu / \omega)^{1/2}$	m	Stokes-layer thickness
δ_2	m	Momentum thickness
θ	(°)	Crank angle within the cycle
κ		Karman constant
μ	N•sec/m^2	Dynamic viscosity
ν	m^2/sec	Kinematic viscosity
ν_o	m^2/sec	Kinematic viscosity at the reference state
ρ	kg/m^3	Density
τ	Pa	Shear stress
$\psi = \overline{u'v'} / u' \bullet v'$		Correlation coefficient
$\omega = 2 \pi f$	rad/sec	Angular frequency
Superscripts		
+		Wall coordinate
*		Normalized quantity, except where used in friction velocity, u_*
Subscripts		
m		Average over cross-section of duct
max		Maximum during one cycle
o		Reference state
w		At the wall

LIST OF FIGURES

LIST OF TABLES

1. Introduction

1.1. Motivation

This study was initiated to understand the fluid mechanics and heat transfer in oscillating flows. In reviewing the literature and in taking the initial measurements, it became clear that laminar-to-turbulent transition in oscillating flows must first be understood and characterized, then flow losses and heat and momentum transfer in the laminar, transitional and turbulent flow were to be investigated.

Although the ultimate motivation is heat transfer and flow friction losses in oscillating flows for application to Stirling engines, no heat transfer is discussed in the present paper. Heat transfer is the topic of the continuing activity.

With regard to engine design, this study was initiated to (1) gain experience with oscillating flow effects that would be useful in making engine design decisions, to (2) help validate existing computational models (Koehler, 1990), and to (3) aid in the development of new codes for use in Stirling engine heat exchanger design (Tew, Thieme, and Dudenhoefer, 1990). The work also represents an opportunity to further the understanding of the fluid mechanics of oscillating flows and associated flow regime transition processes. The initial emphasis of this study was on understanding the mechanisms by which transition takes place in oscillating flow and generally characterizing the fluid mechanics. Next, detailed measurements were conducted at a particular operating point, that of the heater tubes in NASA's Space Power Research Engine (SPRE); dimensionless parameters for the engine and the test are presented in Table 1. Such detailed measurements at the SPRE operating point are useful in characterizing attributes of oscillating flow, including flow phenomena observed in the near-wall region, at flow reversal, and during the transition process, and the effects of inlet boundary conditions on downstream points of the test section. The data also help to isolate the effect of oscillation on pipe flow in the laminar, transitional, and turbulent regimes. Hypotheses associated with oscillating flow can be tested, in particular those which compare spatial acceleration and temporal acceleration in terms of their influences on boundary layer transition. Further details from this study are reported by Seume (1988) and Friedman (1991).

	SPRE heater tubes	Oscillating flow experiment
Re_{max}	1.17×10^4	1.184×10^4
Va	80.0	80.2
A_R	1.03	1.22
l/d	71.0	60.0

Table 1: SPRE operating point parameter values.

1.2. Background

For the purpose of this study, oscillating duct flow is defined as flow in which fluid reciprocates in a duct such that the net mass transfer along the duct axis is zero. By this convention, the term pulsatile flow is reserved for situations where there is a reciprocating velocity component superimposed on a steady flow so that the net mass transfer is not zero. Pulsatile flow has been studied in physiology as an approximation to the flow in blood vessels and oscillating flow approximates the flow in the alveoli of lungs. Oscillating laminar flow has been suggested for efficient heat and mass transfer between the two ends of ducts, Kurzweg (1985). The present study is motivated by the oscillating flow conditions encountered in Stirling engine heat exchangers (Simon and Seume 1988c, Seume and Simon 1986 and 1988a, b, and Friedman 1991).

The appropriate similarity parameters may be derived by normalizing the governing differential equations and the boundary conditions. Normalizing velocity with the amplitude of the bulk-mean velocity, u_{max}, length with the pipe radius, d/2, time with the period of oscillation, $2\pi/\omega$, and fluid properties with the properties at some reference state, "$_0$", the normalized momentum equation becomes:

$$Va\frac{\partial\vec{u}^*}{\partial t^*}+\frac{Re_{max}}{2}\vec{u}^*\bullet\nabla^*\vec{u}^*=-\frac{Re_{max}}{2}\frac{\nabla^*P^*}{\rho^*}+\nu^*\nabla^{*2}\vec{u}^* \qquad (1)$$

Dimensionless parameters which appear are the Reynolds number, here based on the amplitude of the bulk-mean velocity, u_{max},

$$Re_{max}=u_{m,max}d/\nu_0 \qquad (2)$$

and the Valensi number (Park and Baird 1970),

$$Va=\frac{\omega d^2}{4\nu_0} \qquad (3)$$

where ν_0 is the kinematic viscosity at the reference state. Valensi (1947) made the first attempt to characterize the turbulent and laminar flow regimes using similarity parameters. The Valensi number, Va, represents a dimensionless frequency, or acceleration. It has been referred to also as kinetic Reynolds number by White (1974). It is a multiple of the Stokes number (Grassmann and Tuma, 1979) and is proportional to the square of the Womersley parameter, which is the ratio of pipe radius (d/2) to Stokes-layer thickness $\delta = \sqrt{2\nu/\omega}$.

A slightly rearranged version of the normalized momentum equation is:

$$\frac{Str}{2}\frac{\partial \vec{u}^*}{\partial t^*} + \vec{u}^* \bullet \nabla^* \vec{u}^* = -\frac{\nabla^* p^*}{\rho^*} + \frac{2}{Re_{max}} \nu^* \nabla^{*2} \vec{u}^* \qquad (4)$$

for which $Str = \omega d/u_{m,max} = 4\ Va/Re_{max}$ is the Strouhal number.

1.3. Review of Oscillating-flow Research

1.3.1. Laminar

Measurements by Richardson and Tyler (1929) first indicated differences between steady and oscillating flow. They found velocity maxima near the wall for oscillating pipe flow. Sexl (1930), Womersley (1955), and Uchida (1956) have since confirmed the presence of maxima by analysis of sinusoidally and non-sinusoidally oscillating, spatially fully-developed flows. At low frequencies (Va = 1), the flow is quasi-steady. At higher frequencies (Va = 30), the velocity profiles exhibit inflections and flow reversals, relative to the bulk flow, near the wall. Because of fluid inertia, the velocity becomes increasingly out of phase with the pressure gradient as frequency increases, particularly near the centerline, where the fluid inertia is highest. At high frequencies, the fluid near the centerline lags the pressure gradient by approximately 90° and viscous effects are confined to a thin Stokes layer near the wall (Va = 100). Analytical solutions of fully-developed oscillating laminar duct flow can, by superposition with the steady-flow solution, be used to predict pulsatile flows (Uchida, 1956).

1.3.2. Transitional

Transition in unidirectional steady flow is known to be sensitive to bulk- mean velocity and spatial acceleration. Lower velocities and acceleration stabilize, whereas higher velocities and deceleration destabilize. Since, in oscillating flow, velocity and acceleration vary throughout the cycle, flow regimes may change from laminar to turbulent and back throughout the cycle. Hino, et al. (1976) probed an oscillating pipe flow with a single hot-wire and recorded traces of absolute value of the velocity. The traces show a laminar-like flow during the period of strong acceleration and a turbulent-like flow when there was little or no acceleration. With increased Re_{max}, the turbulent portion consumed more of the acceleration phase of the cycle. From these traces, one would expect transition to extend over a broad range of Re_{max}. This expectation is consistent with measurements taken by Ohmi, et al. (1982) where a wide range in Re_{max} was observed between fully laminar and fully turbulent oscillating flows.

Ohmi, et al. (1982) studied forced oscillations of a gas in a straight pipe. They found that the velocity profiles during the laminar part of the cycle agree well with the theoretical oscillating flow laminar solution and that the velocity profiles during the turbulent part agree well with the 1/7-power law for steady turbulent pipe flow. Dijkstra (1984) observed, in flows which displayed transition, that water in the pipe at the time of flow reversal appeared to be laminar and remained laminar during acceleration in the reverse direction while water entering the pipe during the reverse flow was turbulent and remained turbulent as it was convected downstream.

Figure 1 shows experimental observations of transition in terms of Re_{max} and Va. Below the transition lines, the flow is laminar; above them, the flow is turbulent for a portion of the cycle. These experiments are next discussed.

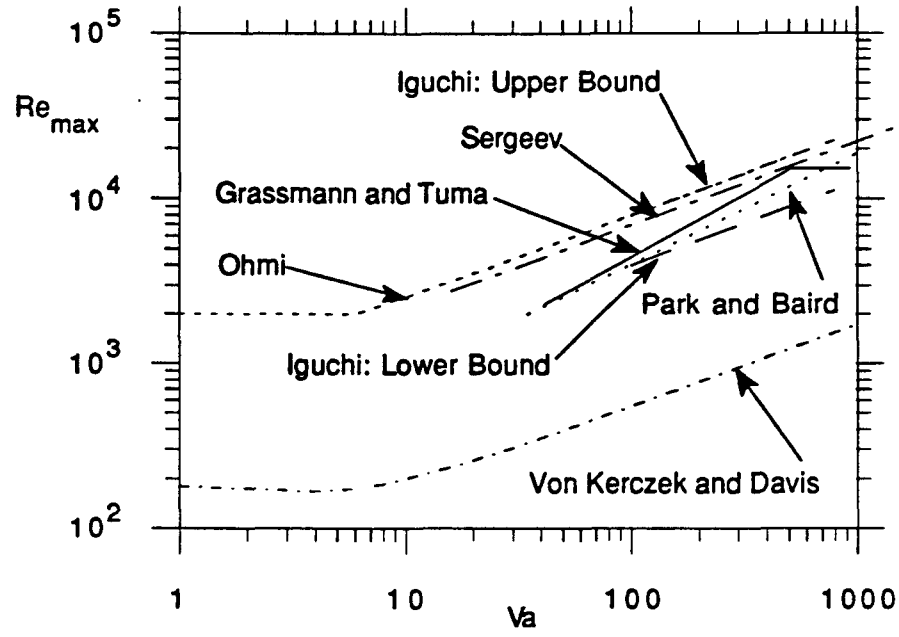

Figure 1: Observations of transition in oscillating flow

Iguchi et al. (1982) observed free oscillations of a liquid column in a U-tube. They located their lower line, which indicates the change from laminar to transitional flow, to be where the amplitude of oscillation begins to deviate from that predicted by the analytical solution for laminar flow. Above this upper line, which separates transitional from fully-turbulent flow, measured amplitudes of oscillation agree with those computed with the 1/7th-power profile. Because of the bend in the U-tube facility and the effect of oscillations on flow through it, a direct comparison with straight-duct transition is difficult. Park and Baird (1970) studied the decay of free oscillations of a liquid in a manometer as well. They assumed transition to occur when the maximum wall shear stress, calculated from the laminar prediction, exceeded that calculated from the 1/7th-power profile. They attribute their data scatter to end effects in the liquid column which are a function of $L^2\omega/\nu$, where L is the length of the liquid column.

Sergeev (1966) did not state his criterion, but, since he used aluminum particle flow visualization, it is assumed that transition was observed through the transparent walls as a change in the particle appearance indicating a change in the flow structure. He studied forced-oscillation flow in a straight tube with square entrances.

Grassmann and Tuma (1979) used an electrolytic technique to observe turbulent fluctuations in the wall-averaged wall mass transfer rate, thus locating transitional behavior. Merkli and Thomann (1975) studied transition from laminar to turbulent oscillating flow at dimensionless frequencies that are beyond the range presented in Figure 1 (Va = 2500 ... 4000). Their apparatus was a piston oscillating in a tube at near resonance. They noticed a weak vortex motion outside the oscillating flow boundary layer.

Though the transition predictions differ with criteria, the researchers agree that Re_{max} of transition increases with Va raised to a power; Grassmann and Tuma suggest $Va^{0.75}$, Park and Baird suggest $Va^{2/3}$, the remaining researchers agree on $Va^{1/2}$. The order of the transition predictions can be rationalized by considering the criteria used by the researchers. The lower line of Iguchi et al. (1982) is based on the first sign of deviation from laminar behavior. The Grassmann and Tuma (1979) criterion is based on fluctuations of mass transfer at the pipe surface. These fluctuations are likely to occur at about the same Va as that established by Sergeev (1966) using the onset of turbulent motion of aluminum tracer particles. Finally, the upper line of Iguchi, et al. (1982) is based on agreement with the 1/7th-power law. It agrees with the observations by Ohmi (1982) in forced oscillation of gas in a straight pipe.

Von Kerczek and Davis (1972) used the energy method to predict a lower bound for the instability of Stokes layers on a flat plate. Figure 1 shows their results as the critical value of Re_{max} below which the oscillating flow cannot go unstable. This lower bound under predicts the measured transition Reynolds numbers by roughly one order of magnitude. The trends of their results, however, agree with Ohmi's results, in particular the $Va^{1/2}$-dependence of the critical value of Re_{max}. Cayzac, et al. (1985) presented predictions for the lower-bound of stability in oscillating pipe flow. Like the results of Von Kerczek and Davis, their computed results agree qualitatively with experiments but show a discrepancy of one order of magnitude. For steady pipe flows, they predicted the lower-bound for instabilities to be Re = 750 while Re = 2300 is the well-known experimental value for high-disturbance ("engineering") flows. The theoretical prediction of the lower-bound of instability by the energy method apparently does not yield results that are useful for "engineering" flows. Other analyses of the stability of oscillating flows are given by Davis (1976).

Hino, et al. (1983) conducted an extensive study of oscillating flow in a rectangular duct using both LDV and hot-wire anemometry. Their work focused on the turbulence structure of the flow, including studies of wall shear stresses, turbulent fluctuations, Reynolds shear stresses, energy balances between production and dissipation, and coherent structures in turbulence. They found that in the deceleration phase, turbulence is generated

vigorously in the near-wall region and spreads to the core flow. Comparisons were made between the basic processes of turbulence production identified in oscillating and steady flows. The present study supplements their careful work while expanding the operating regime. The present work also attempts to provide a physical explanation of transition in oscillating flow exploring the effects of similarity parameters on transition.

Eckmann and Grotberg (1991) studied transition to turbulence in a straight, circular tube for oscillating flows over a wide range of tidal amplitude (A_R) and Womersley parameter, α, using both laser Doppler velocimetry (LDV) and hot-film anemometry. Central to their investigation were three issues: (1) whether, upon transition to turbulence for high-frequency operation, the inviscid core flow remains free of turbulence; (2) whether the presence of a hot-wire probe in the flow affects the transition Reynolds number; and (3) how the results of hot-film measurements compare with those from an LDV system. Among their observations were: (1) post-transition turbulence was confined to a thin region near the wall for Reynolds numbers (based on the Stokes-layer thickness--$Re_\delta = u_{m,max}\delta/\nu$ greater than 500 and high frequencies and (2) although the hot-film probe tripped instabilities, the disturbances did not appear to be convected back over the probe during the second half-cycle, thus affecting the measurement.

Akhavan, et al. (1991a) performed a similar experiment, then followed with an analysis of the flow (Akhavan, et al. 1991b) solving the Navier-Stokes equations using a spectral method. The experiment was performed with LDV measurement in a water facility. Three operating points were investigated -- all displayed transition twice per cycle. The tube was long and the piston stroke short so that the amplitude of any given fluid element was short relative to the tube length. They evaluated instantaneous wall shear stresses by three parallel means, achieving reasonable agreement. Similarity analysis was applied to derive three dimensionless quantities which characterize velocity profile shapes. Four cases, based on the relative sizes of these quantities, were discussed. Regarding transition, they noted an immediate transition to turbulence which they refer to as the "Snap-through transition mechanism," characterized by high production later followed by a return to equilibrium between production and dissipation. In the analysis, Akhavan, et al. found that a two-dimensional perturbation and a model which allows secondary instabilities to create three-dimensional structures were sufficient to predict transition of the flow.

1.3.3. Turbulent

Dijkstra (1984), Köhler (1990), Seume and Simon (1988a), and Vasiliev and Kvon (1971) applied turbulence models taken from steady flow to oscillating and pulsatile pipe flows. The results reported by Ohmi, et al. (1982) and discussed above in which quasi-steady behavior was observed in the turbulent part of the cycle seem to justify this practice for high Re_{max}. They stated that quasi-steady turbulent flow was observed for $Re_{max} > 2800\sqrt{Va}$. They applied a quasi-steady, 1/7-power-law velocity profile and found that it agreed well with measured velocity profiles. Taylor and Aghili (1984) found that their experimental results for pressure drop in oscillating pipe flow do not agree with quasi-steady predictions. The data in their paper is not sufficient to locate their experiments on the Re_{max}, Va parameter map (Fig. 1), however. Kirmse (1979) compared Vasiliev and Kvon's model to his experimental data for large-amplitude, pulsatile flow and concluded that their quasi-steady prediction was not adequate. Akhavan, et al. (1991a) noted that a developing laminar pipe flow solution, beginning with the fluid at rest, yields nearly the measured wall shear stresses during the accelerating portion of the cycle and that fully-developed turbulent pipe flow correlations yield, approximately, the measured wall shear stresses for the remainder of the cycle.

The literature discussed in the previous section suggests that the enclosed portions (both within the dashed and solid lines) of the operating map shown in Figure 2 may be characterized by transition from laminar to turbulent flow, twice within each cycle. They also indicate that detailed measurements are needed to further understand and characterize transition in oscillating flows. Thus, numerous measurements for characterizing transition have been made at the points indicated in Fig. 2 and are reported herein. Further, detailed measurements were taken at a single operating point which simulates the NASA SPRE Space Power Engine, as noted in Table 1, and are also reported herein.

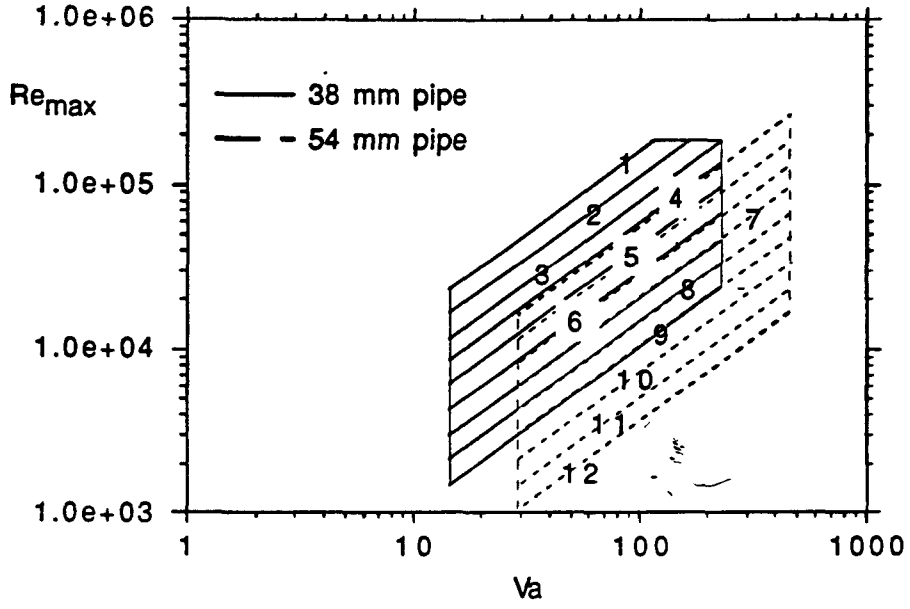

Figure 2: Operating range of the oscillating flow experiment

2. Experimental Setup and Procedure

2.1. Apparatus and Operating Range

2.1.1. Dimensionless Operating Range

Figure 2 shows the range of parameters over which the apparatus to be discussed in this section can operate. On this plot, lines of slope 1 represent conditions of constant Strouhal number (Str). The geometry for the flow in this study is a round, straight pipe. The length-to-diameter ratio (l/d) of the pipe does not appear in Fig. 2. It forms an additional parameter as is next discussed.

In oscillating flow, the displacement of the fluid during a cycle is limited. For a typical fluid particle, this distance is stated as $2\,x_{max}$, or twice the amplitude of fluid displacement during each half-cycle computed as if the fluid moved as a slug. The ratio of the fluid displacement between flow reversals to the pipe length is an important parameter to the problem. It is identified as A_R ($=2x_{max}/l$), the relative stroke or amplitude of fluid motion. The parameter A_R is not an independent similarity parameter but a combination of similarity

parameters which have been introduced. In sinusoidally oscillating flow, $u_{max} = \omega x_{max}$ and, therefore:

$$A_R = \frac{1}{2}\frac{d}{l}\frac{Re_{max}}{Va} = \frac{2}{Str}\frac{d}{l}$$

In Figure 2, lines of slope 1 are lines of constant Str and, thus, are lines of constant A_R if (l/d) is fixed.

2.1.2. Dimensional Operating Range

The dimensional parameters which may be attained with the current apparatus are listed in Table 2. The numbers refer to the numbers for the lines in Figure 2.

bore	stroke	Str		line no.	
(mm)	(mm)	38 mm dia. pipe	54 mm dia. pipe	38 mm dia. pipe	54 mm dia. pipe
356	356	0.00246	0.00699	1	4
356	252	0.00348	0.00989	2	5
356	127	0.00492	0.0140	3	6
216	356	0.00667	0.0190	4	7
216	252	0.00944	0.0268	5	8
216	127	0.0133	0.0379	6	9
127	356	0.0193	0.0548	7	10
127	252	0.0273	0.0775	8	11
127	127	0.0386	0.1097	9	12

Table 2: Nominal operating conditions available (by drive configuration)

2.1.3. Apparatus

Drive Mechanism

From a review of previous research, it became clear that it is desirable to have very nearly sinusoidal fluid motion (cf. Simon and Seume, 1988c). This is particularly important in the transition study since transition is expected to be sensitive to acceleration and deceleration. Various mechanical drives whose kinematics closely approximate a sinusoidal variation of piston position with crank angle were examined. They are not suitable because, though their displacements are nearly sinusoidal, the piston acceleration deviates strongly from that of a sinusoid. This is because the higher harmonics are amplified by differentiation:

$$x_p = a_1 \sin(\omega t) + a_2 \sin(2\omega t) + a_3 \sin(3\omega t) + \ldots$$

$$\frac{\partial x_p}{\partial t} = a_1 \omega \cos(\omega t) + 2\, a_2 \omega \cos(2\omega t) + 3\, a_3 \omega \cos(3\omega t) + \ldots$$

$$\frac{\partial^2 x_p}{\partial t^2} = - a_1 \omega^2 \sin(\omega t) - 4\, a_2 \omega^2 \sin(2\omega t) - 9\, a_3 \omega^2 \sin(3\omega t) + \ldots$$

With some of the drives that were considered, particularly one that uses the slider-crank mechanism, the degree of approximation of the sinusoid varies with the stroke length. Plots of velocity against time reported by Hino, et al. (1983) and Ohmi, et al. (1982) appear to exhibit deviations from sinusoidal behavior due to their use of a slider-crank mechanism. In the present study, a scotch yoke mechanism is used because it produces precise sinusoidal variation of piston position, velocity, and acceleration with crank angle. To attain sinusoidal piston motion with time, the angular velocity of the drive must be constant, however. Thus, heavy flywheels are employed. A sketch of the facility (Figure 3) shows the yokes and flywheels. Flywheels are shown behind the yokes. A second set of flywheels, in front of the yokes, is not shown in the sketch. There are two sets of flywheels, one (fore) set for the working drive and one (aft) set for the balancing drive. The latter balances the linear inertia forces which act in the direction of the test-section axis, caused by the acceleration and deceleration of the yoke, piston rod, and piston. The piston rod is guided by linear bearings, as is the rod that holds the counterweight on the balancing drive. Counterweights on the flywheel balance the rotating components of the scotch-yoke mechanism, i.e. the crank-pin and the rotary bearing.

A flexible joint between the test section and the drive isolates the test section from any motion of the drive. It is designed to allow translational motion of the drive relative to the test-section in all directions. The test-section is bolted to the floor. The drive is powered by a variable-speed motor via a variable-speed transmission, both of which are mounted on the floor. A drive-shaft provides the power to a right-angle gear box which is located under the frame of the drive. Through a torque-limiter, the power is transmitted to another right-angle gear box which has two counter-rotating output shafts. These shafts drive the main and balancing flywheel shafts via timing belts and pulleys to ensure synchronization of the counter-rotating flywheels.

Flow Delivery

Guided by piston-rod linear bearings, the piston reciprocates in the cylinder. The piston is sealed in the cylinder with leather-cup seals in both directions. Stroke and cylinder bore are variable which allows coverage of the operating range of Fig. 2. The stroke is varied by inserting the crank-pin in different radial positions in the flywheel. Three strokes are easily accessible: 356 mm, 252 mm, 178 mm. Note that reducing the stroke results in increased dead-space within the cylinder in that the distance from the flywheel axis to the top end of the cylinder remains fixed. Piston sizes of 356mm, 216mm and 127mm diameter are accommodated with different cylinder liner inserts.

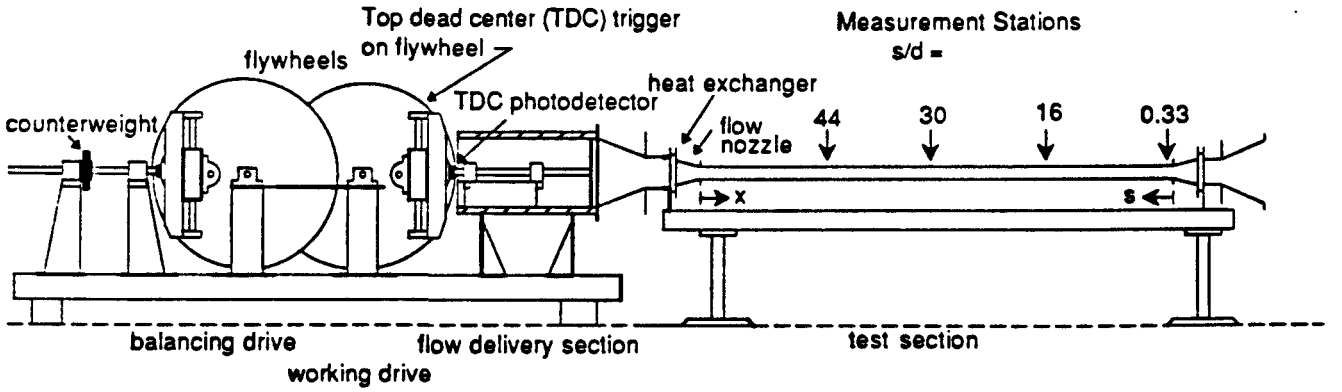

Figure 3: Side view of oscillating flow facility.

Test Section

For most of the cases presented herein, a smooth nozzle, rather than a square pipe-entrance, was employed to keep the flow from separating upon entry. Its contour consisted of two intersecting cubic splines such that the tangents are parallel to the centerline at the inlet and the outlet. At the intersection of the splines, the diameter and its first derivative with respect to axial direction are continuous. Two nozzles provide contraction from the 152 mm diameter entry flow arriving from each heat exchanger to either 38 mm or 54 mm diameter test-sections. For the flush-square entry case, the nozzles, heat exchangers, and conical contractions are removed and the test section is the point of flow entry and exit. The test sections are constructed from cast polyacrylic pipe. Hot-film and hot-wire probes are inserted through horizontal holes in the wall. The probe holder is mounted on an x-y-table which is used to traverse the probe radially in the horizontal direction and vertically within the probe hole. The traversing device is mounted so that there is no relative motion between the test section and the probe holder. The probe hole is sealed around the probe with a black rubber foam sleeve. When the hole is not in use, it is sealed with a plastic plug which has an inner surface that is flush with the inner surface of the tube.

The inflow conditions at the two ends of the test section are nearly symmetric. One exception is that the flexible joint between the conical contraction and heat exchanger at the drive end is 92.1 mm long. While at the open end, the joint is rigid and 76.2 mm long. The other exception is that on one end the flow enters the conical contraction from the room while at the other end, it enters from the cylinder. In the flush square entry case, one end of the tube is suspended in the room while the outer end is connected to the cylinder.

Even though heat exchangers are not needed for the present study, they were installed to maintain hydrodynamically similar conditions to heat-transfer experiments to be performed later The heat exchangers, automobile heater core exchangers, provide fine-structure turbulence similar to that produced with hex-cell flow straighteners used in wind tunnels. They break up large-scale turbulence entering from the conical contractions, however, isolating the test section from the large-scale eddies that may be present in the flow in the conical contractions, cylinder and room. They thus create symmetric conditions of the flow in the test section. Symmetry is important because it ensures that observations made in either of the two flow directions are consistent with each other. In the transition measurements reported below, both half-cycles are measured: one represented a particular x/d point where x is the distance from the drive end of the test section while the other represented its complement (s/d = 1 - x/d, where s is the distance from the room end of the test section). Using both directions cut acquisition time in half. In the detailed

measurements at the SPRE operating point data was taken only during the half cycle when flow was entering from the room end of the test section.

2.2. Instrumentation

For the purposes of this study, hot-wire anemometry was chosen to measure velocities. A straight, single hot-film probe and two types of boundary layer hot-wire probes were used: a single-wire probe and a cross-wire probe. Single-sensor probes are capable of measuring the mean and rms-fluctuation of the axial (streamwise) component of velocity, $\bar{u}$ and u', respectively. The cross-wire probe adds the radial component mean and rms-fluctuation of velocity, $\bar{v}$ and v', respectively, and a Reynolds shear stress, $-\overline{u'v'}$.

The data were processed into various forms, including dimensionless values of mean velocity, Reynolds shear stress and skin friction versus dimensionless wall distance. One type of nondimensionalization involves the use of "wall coordinates," which are based upon velocity and length scales computed from the wall shear stress, u_* and ν/u_*, respectively.

Because the working fluid moves in and out of the room, filtering the flow is difficult. Hot-film sensors were initially chosen because they are more likely to withstand the impact of dust particles than would hot wires. It was later found by inspection and by searching for drift from calibration that this concern was unwarranted. Nevertheless, hot-film sensors were used for the measurements intended to locate the time of transition onset. The hot-film sensors were TSI -20 platinum hot films. Hot-wires were used for the remainder of the study.

Hot-wire anemometry is based on the sensitivity of heat transfer from the heated sensor to mass flux around the sensor. In an isothermal and isobaric flow of constant composition, the heat transfer is a function of velocity only. If the density changes, however, there must be a correction to the measurement to determine velocity. In one extremely high Re_{max} case, density varied periodically with a pressure swing of more than 5% of the barometric pressure. Thus, the static pressure transient was measured prior to the velocity measurements. Static pressures are measured with Validyne DP15 variable-reluctance pressure transducers. Diaphragms with the smallest sufficient pressure range (0.125 psid, 0.2 psid, 0.32 psid, 0.8 psid, 2.0 psid, or 3.2 psid) were used with CD19 carrier-demodulators. The pressure transducers were connected to the test-section with Tygon® tubing, after computation of line dynamics showed that it was appropriate to do so for the low frequencies under which the present tests were conducted (<2Hz).

Circular ducts with small cross sections pose some unique challenges to accurate hot-wire measurements. The circular geometry complicates the process of locating the wall, a procedure which often relies on visual confirmation. Although the test section was constructed of clear plastic, there was the difficulty of sighting through two surfaces (inner and outer walls) that had different radii of curvature. Given the wall's small inner radius of curvature, care must be taken to traverse the probe along a diameter, through the center of the duct, if the sensor is to be positioned accurately. In addition, blockage of the probe in the small cross-sectional area may influence the accurate measurement of flow velocities. Techniques employed to handle these measurement difficulties will be discussed below.

2.2.1. Single-Wire Probe Geometry

Two kinds of sensor support geometry were used in the experimental study. The first is a sensor on a straight probe (TSI 1210) where the sensor is in the same plane as the centerline of the probe stem. With this configuration, the stem reduces the flow area on the plane of the sensor. This geometry was used to hold the hot-film sensor for the transition measurements only.

The second is a boundary-layer type probe (TSI 1218) which has the sensor upstream of the probe stem. The prongs are curved upstream. With this configuration, the blockage of the flow due to the stem is reduced for the half-cycle in which the measurements are taken. For the measurement of velocity profiles the sensor was modified as shown in Fig. 4 such that the active length of the sensor could be moved closer to the wall than would have been possible with the commercial TSI 1218 probe. A hot-wire sensor was mounted on a boundary-layer probe in a looped configuration. The sensor is a TSI, T1.5 platinum-coated tungsten wire with a diameter of 0.004 mm (0.000157 inch) and an active length of 1.27 mm (0.050 inch). The boundary-layer type probe was used because it has the advantage of situating the sensor approximately 12.7 mm (0.5 inch) upstream of the probe stem, the largest flow obstruction in this intrusive measurement technique. Since the measurements were in oscillating flow, though, the probe stem and prongs were upstream of the sensor during the second half of the cycle. This disturbance of the flow limited the measurements to the first half of the cycle (0°to 180°).

The sensor geometry is unique in that the wire extends beyond the plane of the prong tips in the radial direction, aiding both in locating the wall of the test section and in taking velocity measurements very close to the wall (see Fig. 4). The loop of the sensor is also important in that it more closely follows the curvature of the pipe wall than does a

straight-mounted sensor, thereby reducing the measurement error arising from spatial averaging over a finite range of radii.

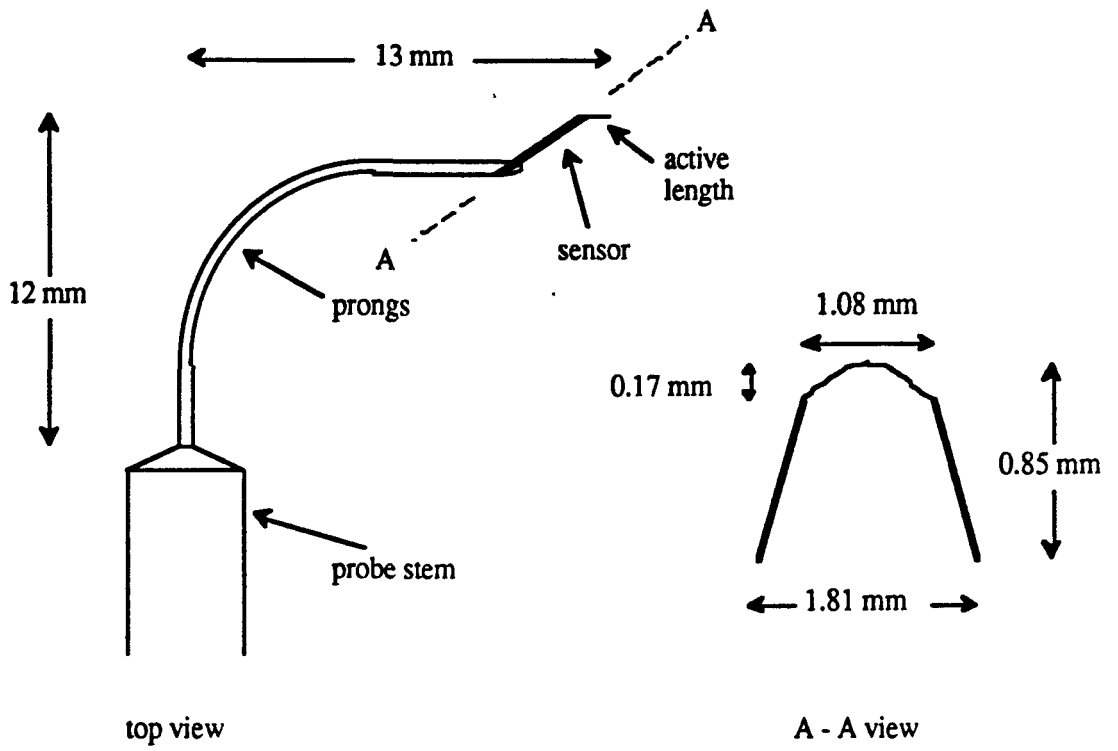

Figure 4: Single-wire boundary layer probe with looped sensor

2.2.2. Cross-Wire Probe Geometry

The cross-wire probe (Fig. 5) consists of two straight wires which are mounted on four prongs at nominally 45° relative to the mean flow direction and 90° relative to each other. The sensors are both of the TSI T1.5 type, 0.004 mm (0.000157 inch) in diameter and 1.32 mm (0.052 inch) active length.

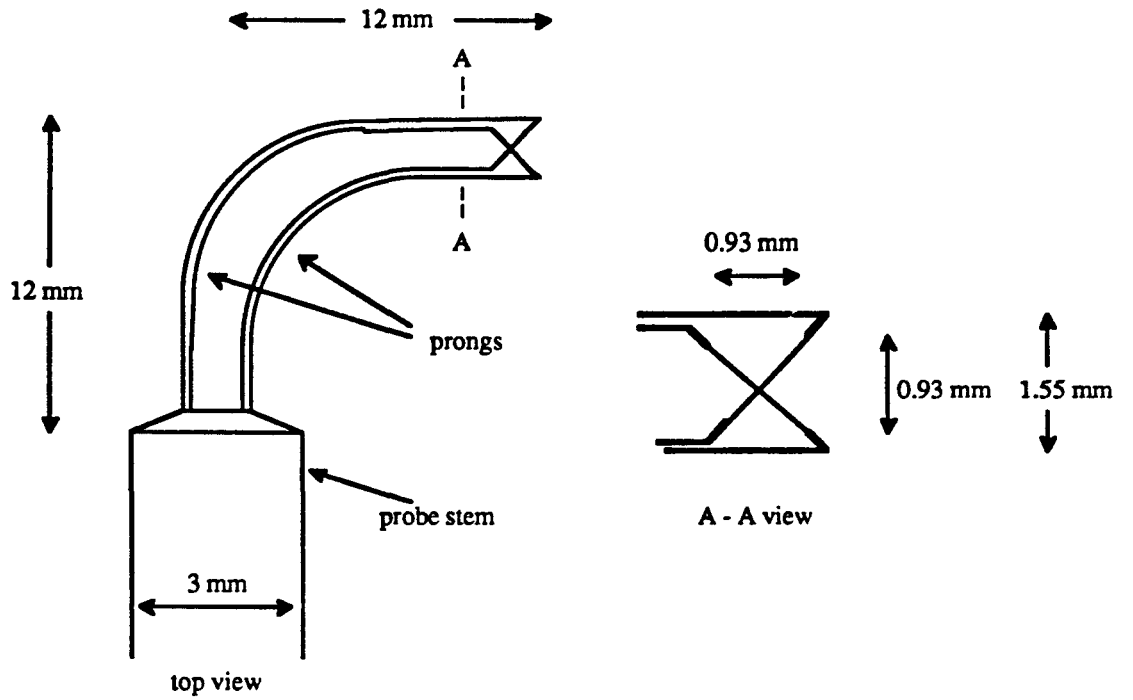

Figure 5: Cross-wire boundary layer probe

As with the single-wire probe, this probe geometry also positions the sensors well upstream of the probe stem. The principal limitation of the probe is its large tip-to-tip spacing, which precludes measuring in the near-wall region below a minimum wall distance of 0.775 mm (0.0305 inch), which is half the tip-to-tip distance and 4% of the radius.

2.3. Calibration

The probes were calibrated in an air jet (Wilson, 1970) which operates at ambient pressure and temperature. Flow rates, and, hence, airstream velocities, were adjustable, allowing calibration over the range of velocities expected in the test section. A micromanometer was used to determine the static pressure, from which the dynamic pressure, and, hence, the velocity, were calculated at the exit plane of the nozzle. A King's law relationship between hot-wire voltage and jet velocity (Eqn. 5) was used to define the calibration equation for velocities with dynamic heads above 0.025 mm (0.001 inch) of water, the minimum reliable reading for the manometer. This corresponds to a velocity of approximately 0.6 m/sec.

$$(\text{voltage})^2 = A + B \cdot (\text{velocity})^n \qquad n = 0.435 \text{ to } 0.5 \qquad (5)$$

For the single-wire probe, it is especially important to have reliable measurements of low velocities if near-wall data are to be used to compute skin friction coefficients. In testing the low velocity measurements, it was found that the calibration voltage for a flow rate of zero is different than the voltage measured in the test section at the point of flow reversal. In the calibration jet, the zero-flow voltage is that for a heated wire under fully-developed natural convection conditions, while flow reversal in the test section is a point of instantaneously zero velocity. Hence, an approximate but reasonable low-velocity portion of the calibration was obtained by connecting the point of minimum velocity that could be accurately measured (and voltage) from the calibration jet with a point located at the minimum voltage recorded in the oscillating flow, assumed to correspond to the instantaneous zero-velocity condition.

For both probes, proper alignment in the calibration jet and in the test section is critical to taking reliable measurements. The single-wire probe is aligned using a carpenters square, with attention paid to both the pitch and yaw of the probe relative to a reference surface, which is either the exit plane of the calibration jet or the wall of the test section. This step is important to the single-wire calibration because the looped sensor's geometry is inherently sensitive to alignment and hence, cooling effectiveness. In the test section, accurate positioning is a prerequisite to reliable near-wall velocity measurements since the flow near the wall is characterized by very steep gradients of velocity.

For the cross-wire probe, cooling of the sensors is by both normal and tangential velocity components. Since these components differ in their cooling

effectiveness, a correction factor, K_T, suggested by Champagne, et al. (1967), was applied to the tangential component, u_T, in both the calibration (Eqn. 6) and acquisition phases. The value of K_T (0.135 for the probe used in these measurements) varies with the ratio of sensor length to sensor diameter. Data acquisition and processing algorithms were written with reference to Kim, 1990.

$$u_{eff} = (u_n^2 + K_T^2 u_T^2)^{1/2} \tag{6}$$

During calibration, the probe was aligned in the center of the exit plane of the calibration jet, where the velocity profile is flat and the jet velocity is axial in direction. Hence, in calibration, the normal and tangential velocity components, u_n and u_T, are functions solely of the jet velocity and the angle between the jet and the normal to the particular hot-wire sensor.

Calibration of the cross-wire sensitivity to yaw-angle alignment was tested in the calibration jet. The alignment was found to be that for which the product of the voltages of the two wires was maximum (see Fig. 6). Since the air supply to the calibration jet had a small but significant long-term unsteadiness, it was necessary to monitor the supply pressure to the jet and correct continuously. To minimize the influence of air supply fluctuations during the alignment test, the product of the two wire voltages was normalized by the fourth root of the pressure transducer voltage, in that the transducer voltage is proportional to the square of velocity and each wire voltage is proportional to velocity to the 1/2 power.

2.4. Data Acquisition

The data acquisition system meets the following specifications:

- Readings are taken at precise crank angle positions for ensemble-averaging.
- Ensemble-averages are taken over 50 and 500 cycles depending on the convergence demands put on particular quantities.
- To get sufficient temporal (crank-angle) resolution, data was taken at every 0.5° of crank angle for the measurements of axial velocity and velocity fluctuation.
- Due to data storage limitations, temporal resolution of the stored data for the measurement of Reynolds stress (u'v') was limited to every 2° of crank angle.

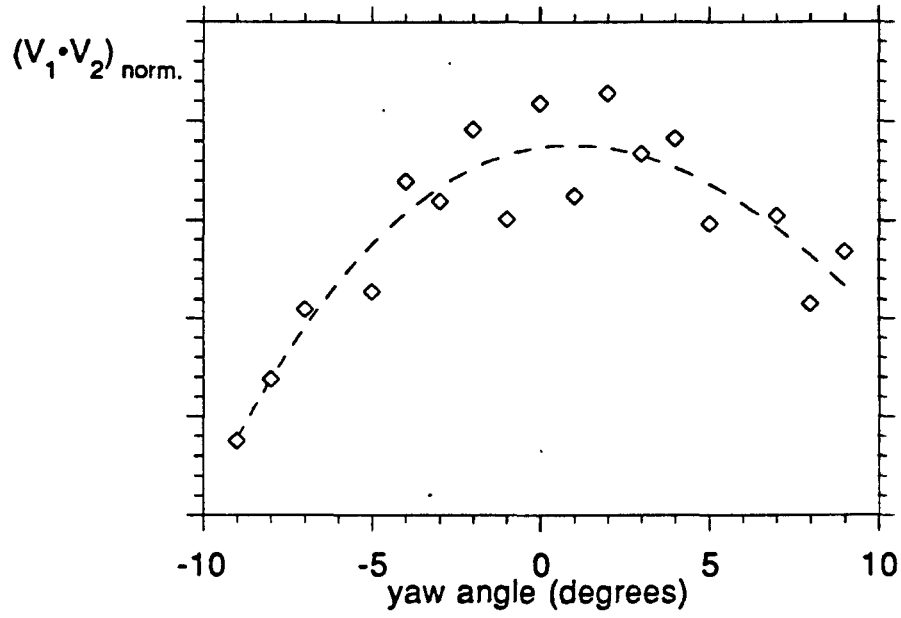

Figure 6: Yaw-angle dependence of cross-wire alignment

A schematic of the hardware and logic is shown in Figure 7. The sensor may be a hot-film, hot-wire, or pressure transducer depending on the measurement to be taken. For velocity measurements, the analog voltage was generated by the hot-wire anemometer bridge; a carrier-demodulator generated the analog voltage signal for the pressure transducers. Analog-to-digital conversion is carried out by a NORLAND Prowler digital storage oscilloscope. It also provided a temporary buffer for 4096 data points. The AT&T 6300 personal computer (PC) controlled the acquisition, read the buffer contents via an IEEE-488 interface bus, and processed the data, including linearization of the hot-wire signal.

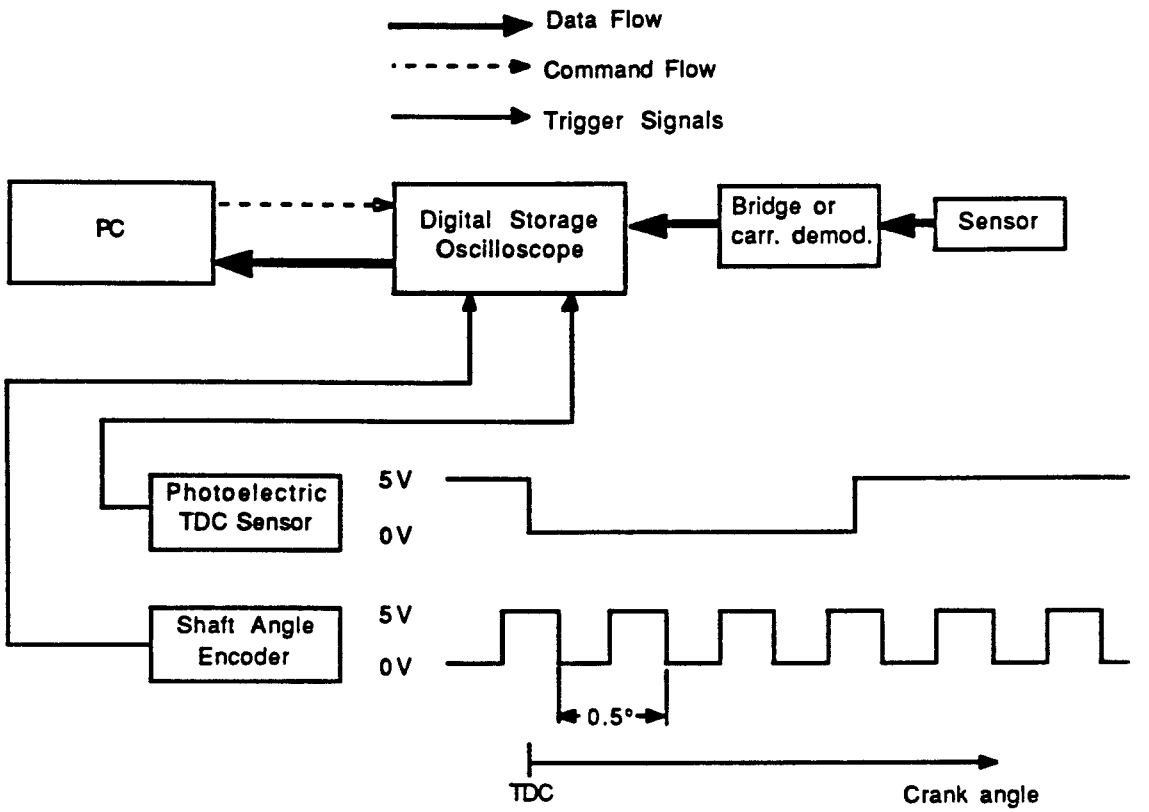

Figure 7: Schematic of data acquisition equipment and logic

A photo-electric switch at the outer edge of one flywheel sensed top dead center (TDC). This signal was passed to the "external trigger" input of the oscilloscope signaling it to store the subsequent 4096 readings. Taking of the individual readings was triggered by the pulses of a shaft-angle encoder mounted on the flywheel shaft, i.e. 720 pulses per cycle were passed to the "sample in" input of the oscilloscope. A simple logic circuit was necessary to convert the signal from the photoelectric switch and the shaft-angle encoder into the TTL signals required for triggering the oscilloscope.

After sampling, the oscilloscope waits until the PC requests the transfer of data to it via the IEEE interface. After transfer, the oscilloscope is instructed by the PC to acquire data and fill the buffer, continuing until the desired number of cycles has been taken.

During the sampling of each cycle, the PC converted the previously sampled voltages into engineering units and updated the sums and sums-of-squares required to calculate ensemble averages, rms-fluctuations and correlations. These data consist of 4096 samples, of which 3600 samples were actually used, corresponding to 5 cycles of 720

samples each (or 900 for 5 cycles of 180 samples each for the shear stress measurements where data was taken at every 2° of crank angle.).

Data are tabulated in Volume 2 of this report. Data acquisition and processing programs are listed in Volume 2.

2.5. Data Processing

Ensemble-averaged axial velocity and rms fluctuation were processed from the single-wire data, while the cross-wire contributed the radial component of velocity and a Reynolds stress. "Ensemble averaged" refers to a quantity which is calculated by summing over multiple events (cycles, in this study) the value of that quantity at a prescribed position in an event. For instance, in this experimental program, the ensemble-averaged velocity, $\bar{u}(\theta)$, is given by Equation 7, for which θ is the crank position within the cycle, u_i is the instantaneous velocity measured in the i^{th} cycle, and N is the number of cycles used to compute the average.

$$\bar{u}(\theta) = \frac{1}{N}\sum_{i=1}^{N} u_i(\theta) \qquad (7)$$

The data can be plotted in a variety of ways, including (1) velocity traces of data taken at designated radial and axial locations for crank positions throughout the cycle, (2) velocity profiles at specific axial positions and times within the cycle, and (3) three-dimensional plots of evolving profiles at particular axial positions throughout the cycle.

Velocities and wall positions were converted into "wall coordinates" using the wall shear stress. In so doing, the Couette flow assumption was employed to determine the expected near-wall profile shape in wall coordinates. The wall shear stress was varied until the experimental data fit the Couette flow model. Two issues complicate the use of this technique in processing experimental data, specifically the uncertainty in wall position and the effect of a time-varying pressure gradient. These are discussed below.

2.5.1. Probe Position

Measurements with both single- and cross-wire anemometer probes were taken at four axial stations, s/d = 0.33, 16, 30, and 44. The parameter s/d relates the axial position of the measurement station, measured from the open end of the test section (Fig. 3), to the pipe diameter. Positions given in terms of x are measured from the opposite end of the test

section, adjacent to the flow delivery section (Fig. 3). The two parameters are related by s=l -x, where l is the test section length. Unless otherwise noted, all the measurements were taken in a 2286 mm (90 inch) test section of 38.1 mm (1.5 inch) diameter, for which the l/d = 60.

For the streamwise velocity component, single-wire measurements were taken at 10 to 20 radial positions for each axial station. Radial spacing of measurements was coarsest in the core, becoming progressively finer as the probe was traversed toward the wall. For the profile measurements, the stations and tabulated measurand values are detailed in Appendix A. Note that in the very near-wall region, radial increments as small as 0.025 mm (0.001 inch) were used. High spatial resolution of velocity measurements in the near-wall region enabled the determination of the wall shear stress in the laminar, transitional and turbulent flow regimes, as will be described. For the two velocity components acquired with the cross-wire probe, measurements at seven radial positions were taken at the four axial stations (see Appendix A).

The operator precisely locates the probe holder with a micrometer head which moves an x-y-table onto which the probe holder is clamped. The location of the various probes was found as follows:

For the hot-film measurements, dummy probes were used to determine the distance of the hot-film from the wall. The dummy probe geometry resembled that of the actual probe. The dummy probe was moved to the wall until it was seen under a microscope to touch its reflection on the inside of the pipe.

For the single-wire, boundary-layer probe, the procedure for accurately locating the probe relative to the wall consisted of two steps which are detailed below. The distance from the wall for the measurements with the hot-wire shown in Fig. 4 was first established roughly (within 0.1 mm) by eye; small corrections (less than 0.1 mm) were later taken after review of the near-wall profiles. Examples of this are the six crank position profiles at the s/d = 0.33 station. Details follow:

The first step requires traversing the probe toward the wall until the wire is observed to flex, slightly. The wire is then backed off the wall until the bend is eliminated. Care is taken to ensure that the sensor is not plastically deformed by the procedure. If that should occur, the wire is recalibrated, since the bend changes the alignment of the sensor relative to the flow and hence, the effectiveness of cooling of the hot-wire.

The second step requires the use of ensemble-averaged velocity profile data which are acquired at a few near-wall radial positions, roughly determined in the first step.

Ensemble averaging over fifty cycles is accurate enough for the wall-finding method. The wall of the test section is determined to within 0.127 mm (0.005 inch) by

extrapolating these initial profiles back through a point of zero velocity. Later when more highly resolved, highly-converged (ensemble averages based upon 500 cycles) data are taken, matching the near-wall profiles to the Couette flow model reduces this uncertainty to approximately 0.025 mm (0.001 inch). When taking near-wall data, there is a region of the flow adjacent to the wall in which the hot-wire indicates that the velocity rises as the wall is approached (see near wall data of Fig. 8, particularly the profiles of low core velocity such as $\theta = 150°$). This artifact of the measurement technique is due to the influence of the wall on the probe, a phenomenon investigated by a number of researchers in unidirectional flow (Bhatia, et al., 1982; Wills, 1962) and also observed in the oscillating flow data of Hino, et al. (1983). This region is identified and eliminated from the profile. Adjacent to this very-near-wall region, the profiles follow a nearly linear shape. It is this data that was used to extrapolate back to zero velocity, as required for compliance with the no-slip wall condition, to determine the probe's position relative to the wall. Intercepts were computed for profiles at every 10 degrees of crank position between 30° and 150° to determine an average shift in y which was applied to the profiles for all crank positions at the particular axial position. Profiles for $\theta < 30°$ or $\theta > 150°$ were excluded from this evaluation of average y-offset to avoid the influence of flow reversal or near-reversal on the calculation of the average y-offset. This average y-offset (one value for each axial station) was applied to the profiles to correct the wall position prior to further processing, plotting, and tabulating. This y-offset was always very small, less than 0.1mm.

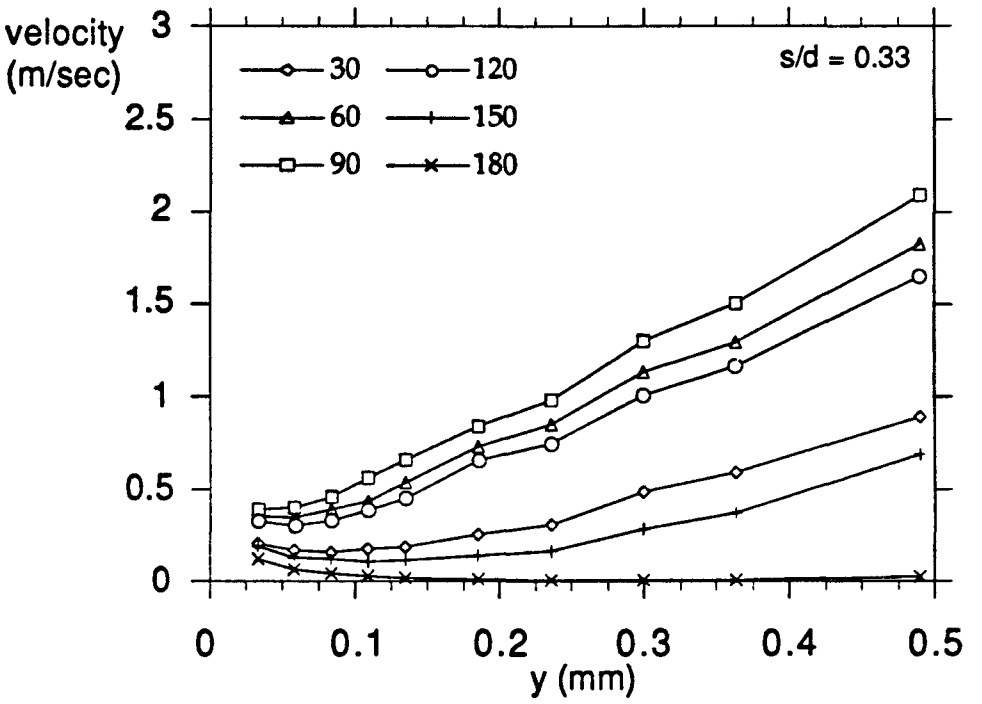

Figure 8: Near-wall profiles of ensemble-averaged velocity at s/d = 0.33

The geometry of the cross-wire probe aided in locating the wall but prevented measuring velocities very close to the wall. The wall position was determined by traversing the probe radially until it touched its reflection, as observed through the pipe wall with the aid of a magnifying lens. From this point, the probe position was finely adjusted until a very slight resistance was felt through the traversing mechanism. The position of the center of the probe, which was taken to be the measuring point, was determined directly from the geometry of the probe.

2.5.2. Pressure Gradient Effect on the Couette Flow Model

In oscillating flow, it is expected that the boundary layer data will not follow the universal flat-plate law of the wall profile due to the influence of the streamwise pressure gradient. Therefore, a modified model from that used for flat-plate comparisons must be devised for processing the data. An analogy is made between spatial and temporal pressure

gradients, and it is assumed that the oscillating flow pressure gradient effect is entirely dependent on the instantaneous temporal pressure gradient, independent of flow acceleration history. The effect of spatial pressure gradient on unidirectional flows is documented in the literature (Kays and Crawford, 1980). For oscillating flow, within a cycle, the pressure gradient changes both in magnitude and sign. During the acceleration phase, the pressure gradient is favorable, decreasing from a maximum at flow reversal to zero at 90°, the point of maximum piston velocity. Beyond this point, the flow undergoes deceleration as the adverse pressure gradient increases to a maximum at 180°, the point of bulk flow reversal. Given that there is a different pressure gradient correction for laminar boundary layer flow than for turbulent flow, the two were processed separately, as discussed below.

Laminar-Like Flow

For laminar-like, steady, boundary layer flow, the momentum equation (Eqn. 8) is employed. For the near-wall region in which the Couette flow assumption is valid, specifically, where the inertial term is small relative to the shear stress and pressure gradient terms, integration of the momentum equation gives the y-dependence of mean velocity on the shear stress distribution and the spatial pressure gradient (Eqn. 9).

The spatial pressure gradient is written in terms of the gradient of freestream velocity (Eqn. 10a). For an internal flow, the bulk-mean velocity, u_m, is used in place of the free-stream velocity (Eqn. 10b). This spatial gradient is converted into a temporal gradient by considering the displacement of the mean flow (Eqn. 11). Combining Equations 10b and 11 gives the temporal pressure gradient in terms of the bulk-mean velocity (Eqn. 12). The temporal gradient of bulk-mean velocity is derived from purely sinusoidal motion of the piston using the continuity equation and geometric parameters of the oscillating flow facility (Eqn. 13). In this analysis, the flow can be treated as incompressible. Combining terms produces the laminar oscillating flow relationship (Eqn. 14) which is employed as the universal shape to which the data is matched by proper choice of u_*.

$$\bar{u}\,\partial\bar{u}/\partial x - \partial\tau/\partial y + d\bar{p}/dx = 0 \quad (8)$$

$$u(y) = (\tau_w/\mu)\,y + (1/2\mu\, d\bar{p}/dx)\,y^2 \quad (9)$$

$$d\bar{p}/dx = -\,d/dx\,(1/2\,\rho u_\infty{}^2) \quad (10a)$$

$$d\bar{p}/dx = -\,\rho u_m\, du_m/dx \quad (10b)$$

$$dx = u_m dt \quad (11)$$

$$d/dx = 1/u_m\, d/dt$$

$$d\bar{p}/dx = -\,\rho\, du_m/dt \quad (12)$$

$$u_m = s\omega(D/d)^2 \sin(\omega t) \quad (13)$$

$$du_m/dt = s\omega^2(D/d)^2 \cos(\omega t)$$

$$u^+(y^+) = y^+ - (\nu/2\, du_m/dt)\, 1/u_*{}^3\, y^{+2} \quad (14)$$

The technique consists of iterating on the friction velocity, shifting the data to match the model. In the oscillating flow model (Eqn. 14) the model parameters as well as the data vary throughout the cycle. As a result, the data is processed against the model specific to each discrete crank position, in this case every 10 degrees. This is done after determining that the flow is laminar-like. Iteration with various values of friction velocity continues until the data fit the model in the near-wall region of the flow where the Couette flow assumption holds.

Turbulent-like Flow

For that portion of the cycle in which the flow is turbulent-like, the data were processed using the Couette flow assumption and the mixing length turbulence closure model, with van Driest damping. In the Prandtl mixing length model (Eqn. 15), the effective sublayer thickness, A^+, is an empirically-based function (Kays & Crawford, 1980) of the pressure gradient (Eqn. 16). Since the model is based on a spatial pressure gradient, an analogy between spatial and temporal gradients is again made (Eqn. 17). This result is combined with the definition of the dimensionless pressure gradient (Eqn. 18) to produce Equation 19. In turbulent flow, the effective shear stress is a function of both the laminar and turbulent (apparent) viscosities (Eqn. 20). Substituting the mixing length model (Eqn. 15) into the relationship for the eddy diffusivity for momentum (Eqn. 21), and the resulting expression into the nondimensionalized form (Eqn. 22) of Equation 20, produces a nondimensional velocity gradient (Eqn. 23) which is solely a function of y^+ and p^+ (contained within A^+). This equation is integrated between the limits of any two consecutive wall distances, $y_1{}^+$ and $y_2{}^+$, to produce a model profile (Eqn. 24) useful in the

processing of oscillating flow data in the turbulent-like portions of the cycle. It is the $u^+(y^+)$ shape from integration of Eqn. 24 that the data is to match by proper choice of u_*.

$$l = \kappa y \left(1 - 1 / e^{y^+/A^+} \right) \tag{15}$$

$$A^+ = 25 / [\, 20.59\, p^+ + 1 \,] \qquad p^+ > 0 \text{ (adverse)} \tag{16}$$

$$A^+ = 25 / [\, 30.175\, p^+ + 1 \,] \qquad p^+ < 0 \text{ (favorable)}$$

$$d\bar{p}/dx = - \rho\, du_\infty/dt = - \rho\, s\omega^2 (D/d)^2 \cos(\omega t) \tag{17}$$

$$p^+ = [d\bar{p}/dx]\, \nu/\rho u_*^3 \tag{18}$$

$$p^+ = s\omega^2 (D/d)^2 \cos(\omega t)\, \nu/u_*^3 \tag{19}$$

$$\tau_w / \rho = (\nu + \varepsilon_m)\, du/dy \tag{20}$$

$$\varepsilon_m = l^2 |du/dy| \tag{21}$$

$$du^+/dy^+ = (1 + \varepsilon_m/\nu)^{-1} \tag{22}$$

$$du^+/dy^+ = \frac{(-1 \pm (1 + 4\kappa^2 y^{+2} (1 - 1 / e^{y^+/A^+})^2)^{0.5})}{2\kappa^2 y^{+2} (1 - 1 / e^{y^+/A^+})^2} \tag{23}$$

$$u^+(y_2^+) = u^+(y_1^+) + \int (du^+/dy^+)\, dy^+ \tag{24}$$

2.5.3. Variation of Ambient Conditions

At each of the four axial measurement stations, data acquisition required between 10 and 11 hours of run time. The ambient temperature and pressure were measured prior to data acquisition at each radial measurement station and supplied to the data acquisition program for appropriate temperature correction to the ongoing hot-wire measurements. For a complete set of measurements at any one of the axial stations, the largest variations were 2.2°C and 0.5% in pressure. For the purpose of processing, fluid properties were evaluated separately for each axial station at the temperature and pressure corresponding to the average values of the ambient conditions recorded for that station's radial positions.

3. Results

3.1. Qualification Tests

Qualification tests include:

- steady-flow measurements to qualify the measurement techniques in a well-documented flow,
- unsteady measurements to ensure a sufficiently large sample size for ensemble-averaging,
- unsteady measurements to document cycle-to-cycle variation in the transition position, and
- a test of the validity of the similarity parameters.

The similarity tests will be discussed in section 3.2.4 because their interpretation requires the transition test results and discussion.

3.1.1. Variation in Flywheel Rotational Speed

As mentioned in the description of the facility (Sec. 2), the rig was designed to deliver smooth, sinusoidal displacement to the fluid. The large, high-inertia flywheels (Fig. 3) are employed to ensure that the rotational speed is nearly constant. Figure 9, a typical trace of flywheel rotational speed, ω, has a peak-to-peak variation of less than 4% for the SPRE operating conditions (Table 1). The small variations in rotational speed are likely due to a cyclically-varying fluid pressure drop in the test section, non-uniform friction in the flow-delivery mechanism, etc.

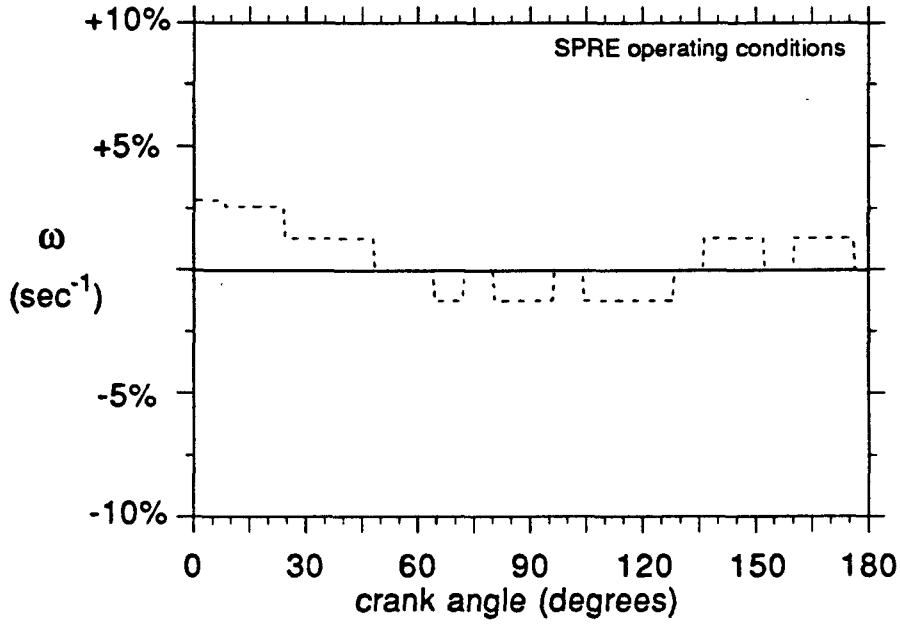

Figure 9: Variation in flywheel rotational speed for SPRE operating conditions

3.1.2. Convergence of velocity measurements in oscillating flow

In hot-wire or hot-film measurements of nominally steady turbulent boundary-layer flows, typically 1000 to 5000 samples are conservatively taken over 30 to 60 seconds to obtain well-converged values of mean velocity and velocity fluctuation. In the present experiment, this practice would require excessive time because of the low frequency of the flow oscillation. Therefore, the minimum acceptable number of cycles required for each ensemble-average was determined early in the program. Convergence with the number of samples was studied using velocity fluctuation measurements because it is known that the higher moments of a distribution converge more slowly than do the lower moments. The "rms velocity fluctuation," u', refers to the root-mean square fluctuation $\sqrt{\overline{u'^2}}$, about the ensemble-averaged velocity, $\bar{u}$, and is represented by $u' = u - \bar{u}$. Figure 10 shows a comparison of rms velocity fluctuations. The boundary layer probe is facing the drive,

therefore only the second half of the cycle is displayed. Part (a) is based on 100 cycles acquired, and part (b) is 50 cycles. The values have not fully converged in either case, as evidenced by the randomness throughout the cycle. The magnitude of velocity fluctuation throughout the cycle and the positions of turbulent flow, indicated by high fluctuation values, are approximately the same for the two sample sizes (50 and 100), however. Thus, a sample size of 50 was used for ensemble-averaging when the transition position was being determined. Because the ensemble-averages are not fully converged, there is a random component of the uncertainty associated with the small sample size to factor into the measurement uncertainty.

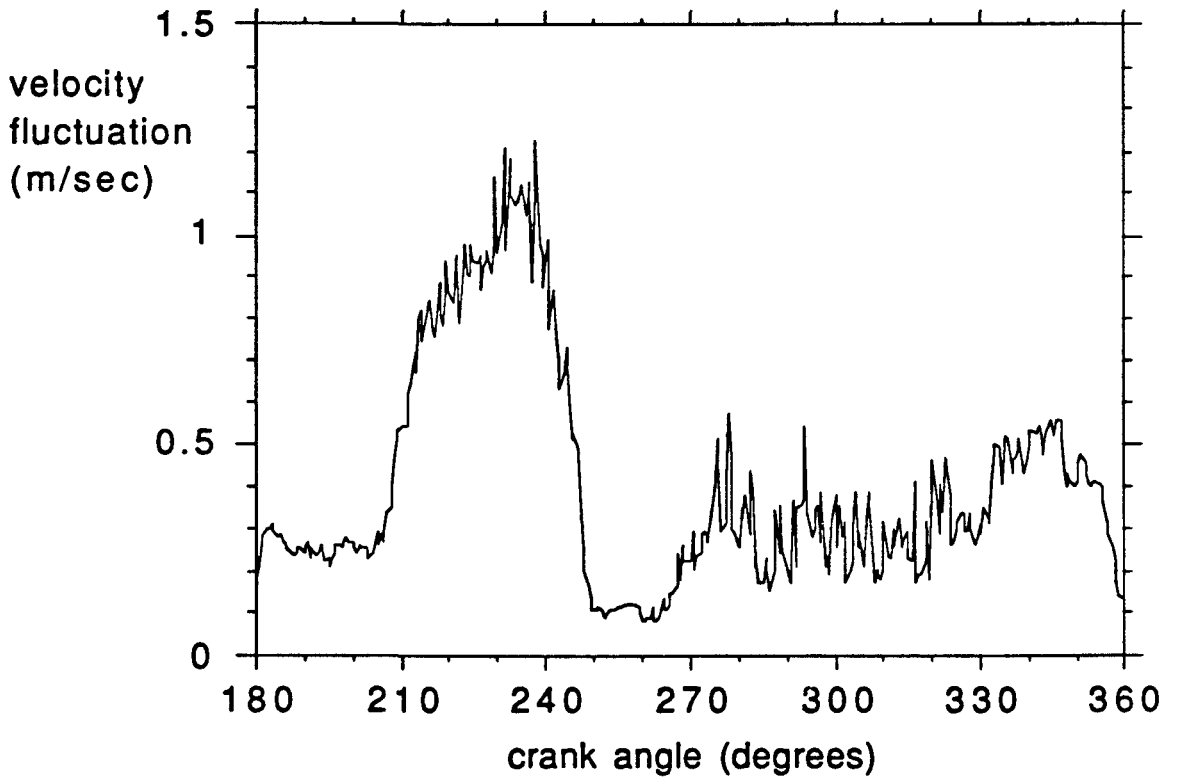

Figure 10(a): Qualification Data; Velocity fluctuations, calculated from 100 cycles, case 1 (see section 3.2) at x/d = 52 and r/R = 0.93, of the l/d = 60 test section.

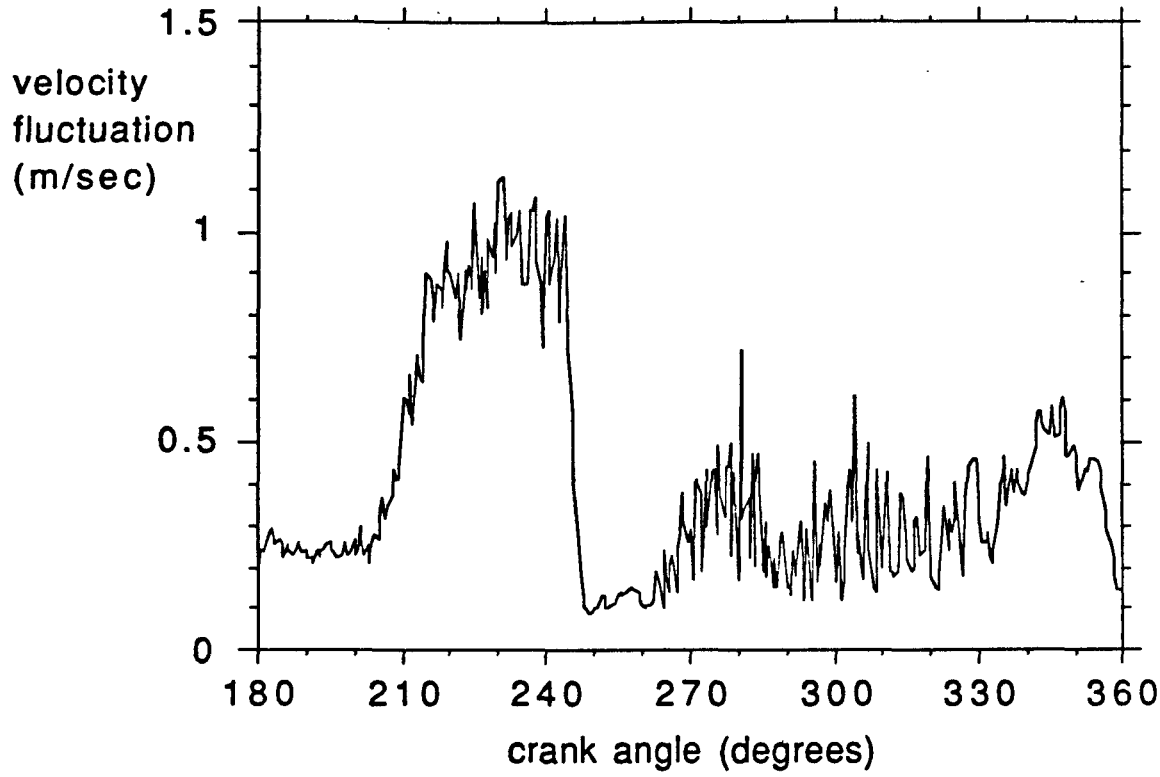

Figure 10(b): Velocity fluctuation, calculated from 50 cycles, case 1 (see section 3.2) x/d = 52, l/d = 60, and r/R = 0.93

For the detailed measurements at the SPRE operating point, the single-wire profile data were ensemble averaged over 500 cycles. Figure 11, a plot of traces of rms-velocity fluctuation at r/R = 0.990 for s/d = 44, illustrates the reduction of cycle-to-cycle variation of velocity fluctuation (indicated by the smoothness of the curves) between 50 and 500 cycles for the SPRE conditions. Note that the trace for 500 cycles is displaced vertically by 0.3 m/sec for ease of interpretation. Residual fluctuations (variations about the mean, in these coordinates) were reduced from 11% to 1.4% at a representative position within the cycle, in this case 120°. It should be noted that, if the number of cycles included in the ensemble average were to be increased to infinity, the residual fluctuations would be effectively eliminated (with the local mean values unaltered) and the curves would become smooth, although there is no strong incentive to approach this in these tests.

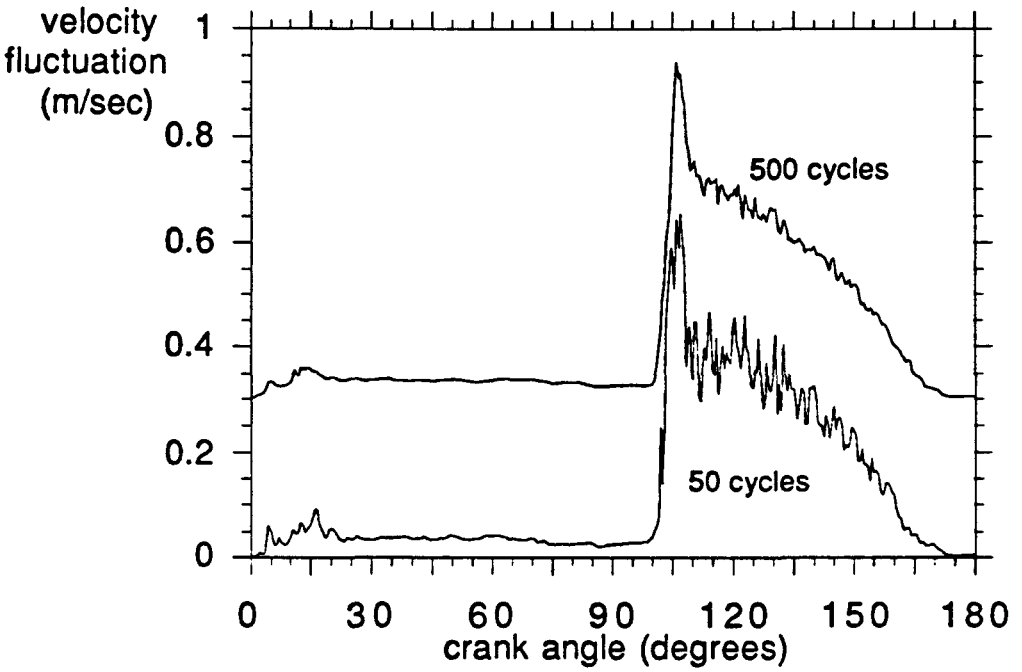

Figure 11: Convergence test of single-wire measurements: rms-velocity fluctuation

The cross-wire data were ensemble averaged over only 150 cycles due to significantly longer data processing times during acquisition. Figures 12 and 13 are traces of streamwise velocity fluctuation, u', and Reynolds stress, $-\overline{u'v'}$, respectively, at r/R = 0.733 and s/d = 0.33. Note that the traces of velocity fluctuation and Reynolds stress at 150 cycles are displaced vertically by 0.2 m/sec and 0.035 m^2/sec^2, respectively, for ease of comparison. Consider the reduction in residual fluctuations for different parts of the cycle. For that portion of the cycle between 30° and 40°, the standard deviation about the mean was reduced by 37% and 44% for the velocity fluctuation and Reynolds stress, respectively, between 75 and 150 cycles. Similarly, between 120° and 130°, the standard deviation was reduced by 51% and 47% for the velocity fluctuation and Reynolds stress terms, respectively. The convergence of the cross-wire data is slower, with increasing record size, than that of the single-wire.

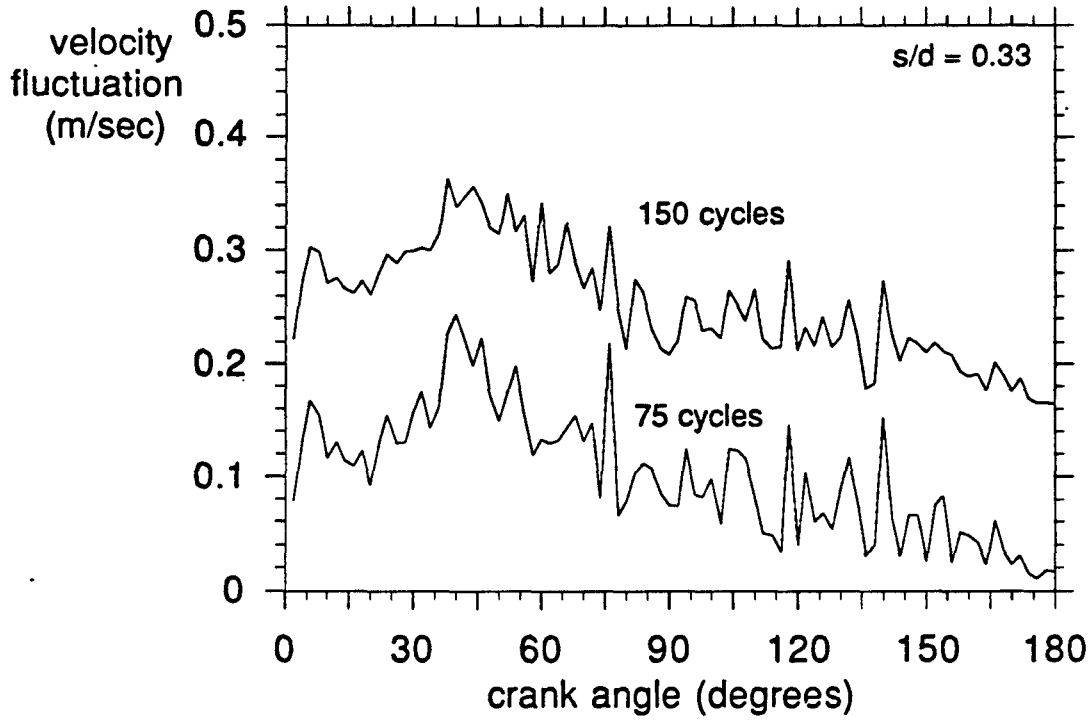

Figure 12: Convergence test of cross-wire measurements: velocity fluctuation at r/R = 0.733 for s/d = 0.33

Cross-wire measurements are likely to converge more slowly due both to the greater sensitivity of the cross-wire to multiple components of velocity and the degree of stiffness of the equations which are used in the data acquisition program to solve for the instantaneous velocity components. Ensemble averaging over 150 cycles was deemed acceptable for the purpose of this investigation.

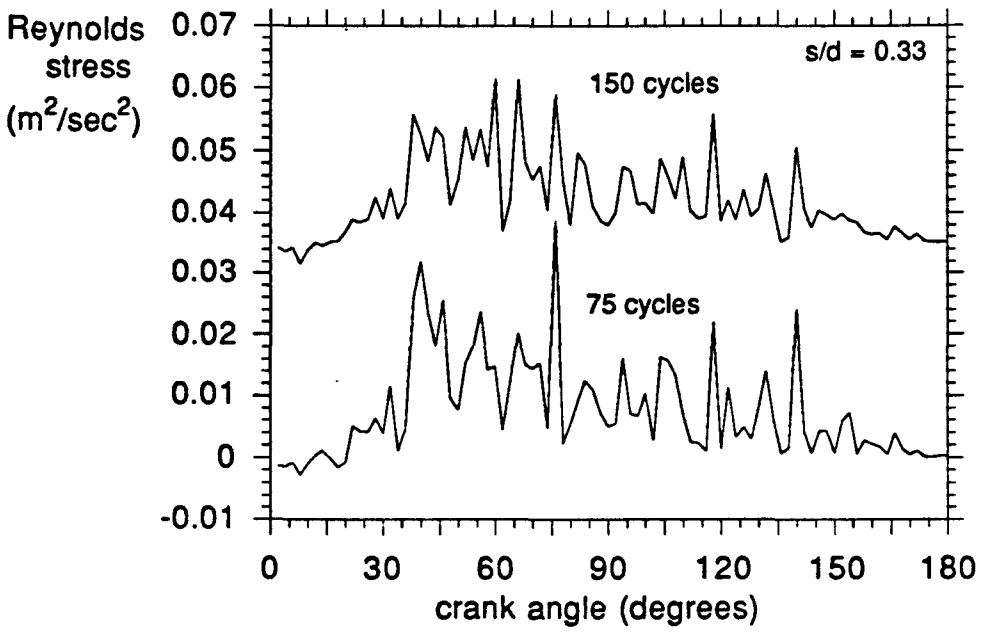

Figure 13: Convergence test of cross-wire measurements: Reynolds stress at r/R = 0.733 for s/d = 0.33

3.1.3. Volume Balance: Piston Displacement vs. Volumetric Flow Computed from Hot-Wire Readings

Verification of the accuracy of the hot-wire measurements is next discussed. One qualification test consists of comparing the volume of air displaced by the piston during a half-cycle to the volume computed from the velocities measured by the hot-wire. The latter is calculated by integrating the bulk-mean velocity over the cycle, between flow reversals. Table 3 compares the volume displacement for the half-cycle calculated from the hot-wire velocity measurements to each corresponding volume determined from displacement of the piston for a stroke.

s/d	Hot-wire Measurement vs. Piston Displacement (% difference in volume)
0.33	- 3.0
16	- 1.3
30	- 6.3
44	- 5.0

Table 3: Piston displacement versus hot-wire measurements

All four data sets underestimate the volume displaced by the piston. This may be due to a combination of factors, including (but not limited to) compression in the dead space between the piston and the tube, errors in the hot-wire calibration (See Appendix B for an uncertainty analysis), leakage of air past the piston leather cup seals, cyclic density variations, inaccuracies in zeroing the probe against the wall, and probe blockage effects. As mentioned in Section 2.3. above, special care was taken in calibration to ensure that accurate low velocity measurements, both in the near-wall region and in the vicinity of flow reversal, were taken. For the SPRE operating point, the pressure swing and, hence, the density change, was not significant. Due to the large size of the probe relative to the test section, blockage at the axial position of the probe stem increases up to a maximum of nearly 10% when the probe is measuring in the near-wall region. One advantage in the measurements is that the boundary-layer probes measure upstream of the significant blockage location, thereby reducing the blockage effect to well below the 10% figure, perhaps to 1 - 2%.

3.1.4. Repeatability of Transition Crank Position

A test of cycle-to-cycle variation of the crank position at transition was conducted at the SPRE operating point. In the test, the data were separated according to the crank position at which transition was observed. Transition position was designated as that point in the cycle for which the instantaneous rms velocity fluctuation (such as in Fig. 10) exceeded a predetermined value. The results were independent of the value of velocity fluctuation used in that determination, over a wide range of reasonable values. Figure 14, based on a test of 500 cycles, demonstrates that the position of transition varies from cycle

to cycle. The standard deviation in crank position at transition is 2.2° about an average transition position of 87.3° for this axial station, s/d = 30.

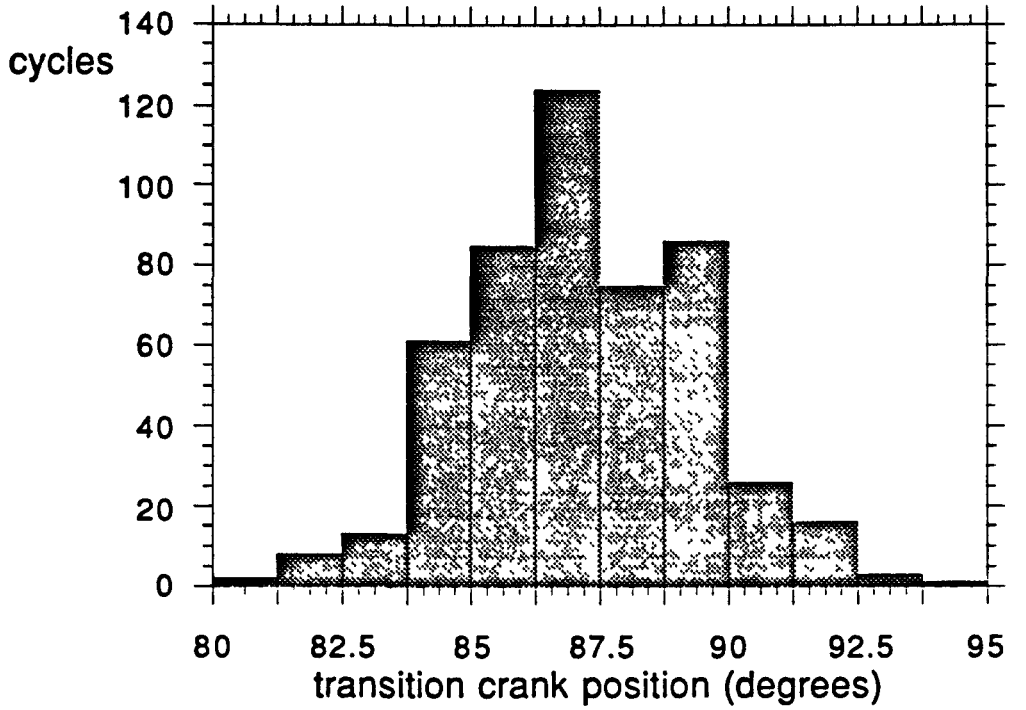

Figure 14: Probability distribution for transition crank position based on 500 cycles

The standard deviation would be similar in magnitude at the other axial stations. With this information, one can assume that in Figure 11, for instance, the increase in rms velocity fluctuation level to 0.65 m/sec (beyond a value of 0.4 m/sec to which the signal settles soon after) recorded at transition (app. 107°) is an overshoot due to cycle-to-cycle variations and hence, is not turbulence. The actual rms velocity fluctuations associated with turbulence at transition are likely to be closer to post-transition levels, in this case approximately 0.4 m/sec.

3.1.5. Steady-flow Results

Measurements in steady unidirectional pipe flow were performed to partially qualify the measurement techniques. To generate unidirectional flow, the flow nozzle at the drive end of the test section (see Fig. 3) was removed and a centrifugal fan was attached at the opposing end to draw air down the length of the test section. The fan was attached to the test section via a 3 m long, 100 mm diameter flexible tube.

The profiles taken with the straight probe were skewed, somewhat, by interference of the stem of the probe with the flow. Though it is felt that the straight probe accurately located the position within the cycle of flow transition, it was decided, based upon these tests, that profile measurements would be taken with a boundary layer probe. Comparisons of transition locations taken with the two probes support the assumption that the blockage by the straight probe does not affect the measurement of transition location within the cycle.

A steady-flow velocity profile, taken with a boundary-layer probe, is shown in Figure 15. The ensemble-averaged profile, obtained from 4096 samples, is slightly asymmetric (dashed line). The reason for this asymmetry is that the effective distance of the probe from the wall could not be determined precisely before reviewing the measurement results. When the wall distance is corrected, the velocity profile has the expected shape (solid line). In Figure 16, the velocity profile is plotted in wall-coordinates. It agrees well with the log-law line for fully-developed pipe flow in the log-linear region (Schlichting 1979, p. 603).

Measurements were also taken with a cross-wire probe in steady, fully-developed pipe flow in order to qualify the Reynolds stress values by comparing to those of a previous study (Laufer, 1953). A 100 mm long honeycomb section was inserted into the flexible tube to avoid induced swirl. To achieve fully-developed steady-flow conditions, several modifications were made. A 3 mm (0.12 inch) thick circular boundary-layer trip (31% area reduction) was inserted in the pipe entrance, the tube length was extended to l/d=80.3, and measurements were taken at the furthest downstream station, x/d = 78.3. Static pressure taps were used to verify a fully-developed flow pressure gradient. Wall shear stress, was determined from the pressure gradient. Profile measurements of Reynolds shear stress were taken, normalized, and compared with those of Laufer (Fig. 17). Laufer's data were taken at x/d = 50.3 in a pipe with a 246.9 mm (9.72 inch) inner diameter and l/d of 50.6. In both cases, Re_d was approximately 50,000.

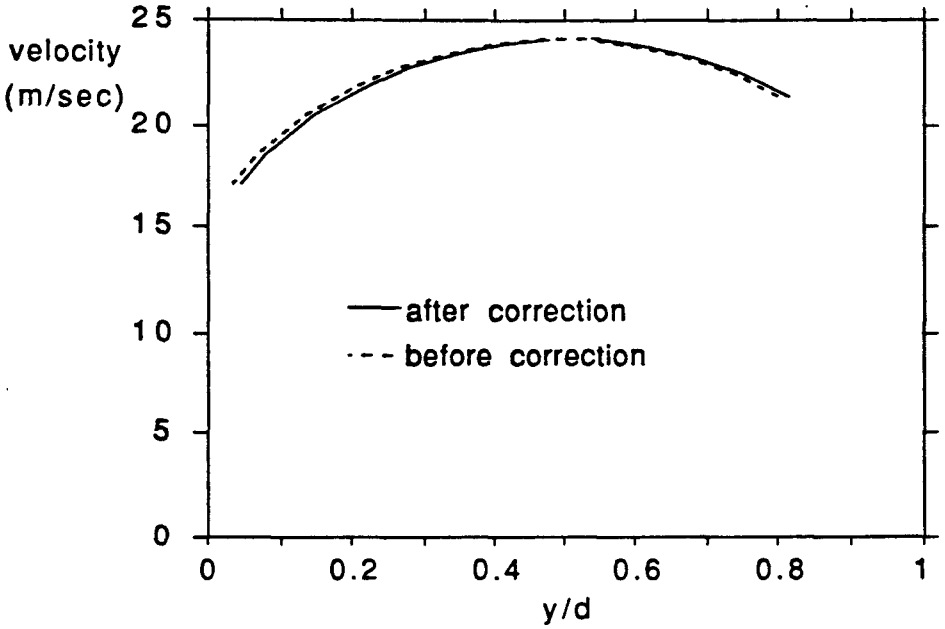

Figure 15: Qualification test; steady-flow velocity profile taken with $Re_{m,max}$ = 44,800 at x/d = 76.

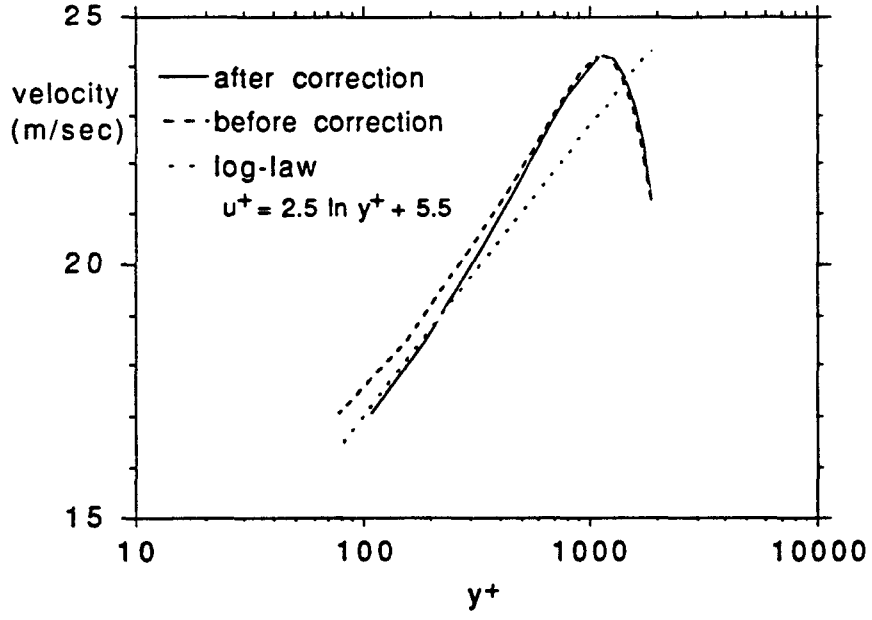

Figure 16: Steady-flow velocity profile in wall coordinates.

The difference between the measurements and the reference case for $y/R < 0.2$ is probably due to spatial averaging of gradients over the active length of the sensors. The sensor length to-pipe-diameter ratio is approximately 13 times that of Laufer's study. Consistent with this, Laufer's data shows a rolloff at about one-thirteenth the y/R for which the present data roll off. Analogous differences were observed in profiles of normalized axial and radial velocity fluctuations, as shown in Figures 18 and 19. This characteristic of the cross-wire-size to pipe-size ratio limited the use of the probe to measurements for which $y/R \geq 0.2$ $(r/R \leq 0.8)$.

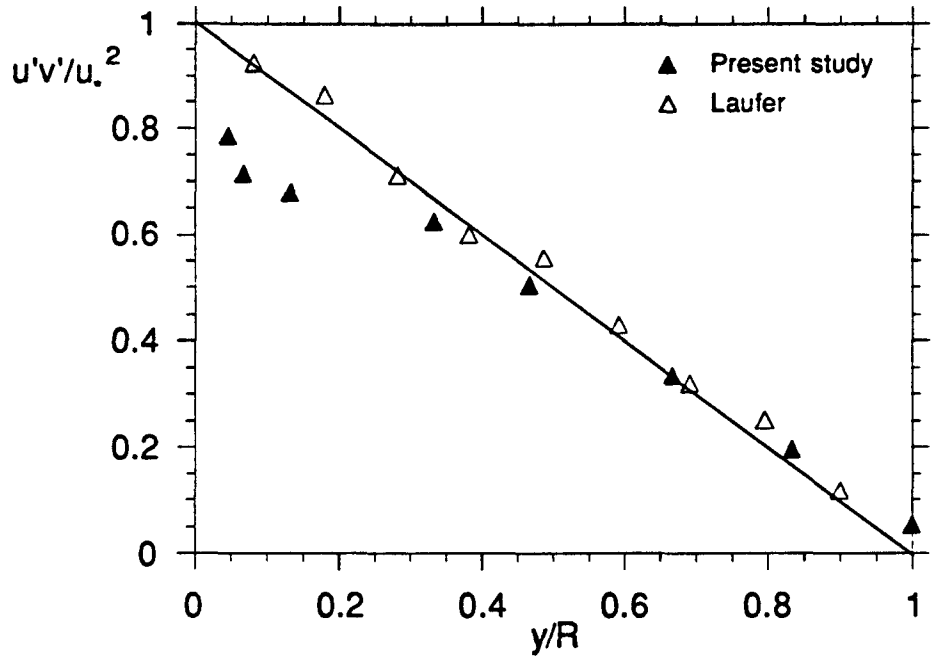

Figure 17: Reynolds stress qualification test in fully-developed steady flow.

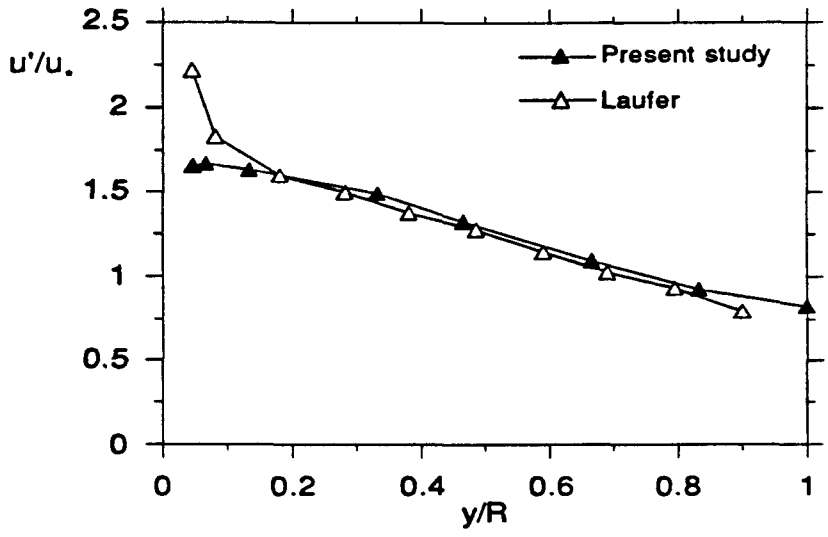

Figure 18: Normalized streamwise velocity fluctuation in fully-developed steady flow.

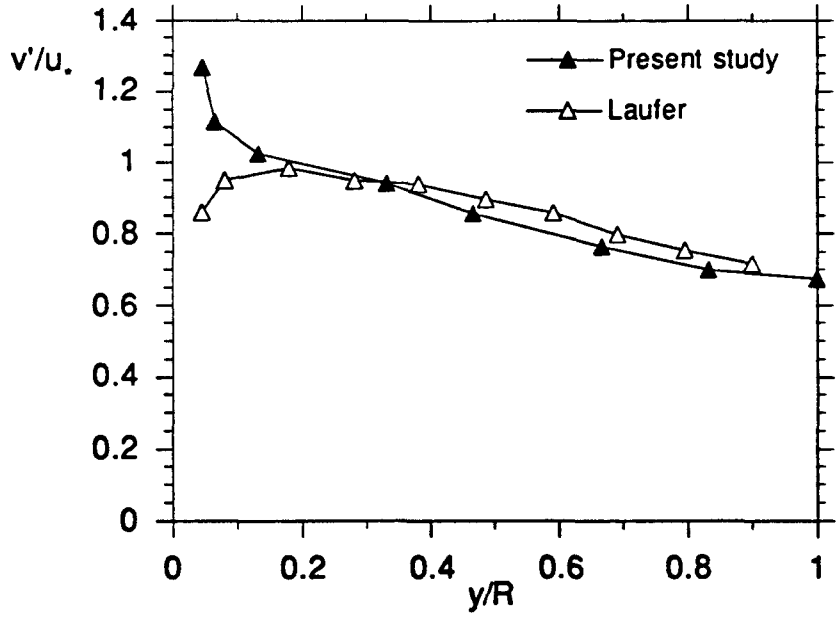

Figure 19: Normalized radial velocity fluctuation in fully-developed steady flow.

3.2. Exploration of transition mechanisms

Transition from laminar to turbulent flow was studied for 11 cases that differ in values of the similarity parameters. Figure 20 shows the location of the transition cases a through q on a map of the operating regime. Tables 4 and 5 provide summaries of dimensional and similarity parameters.

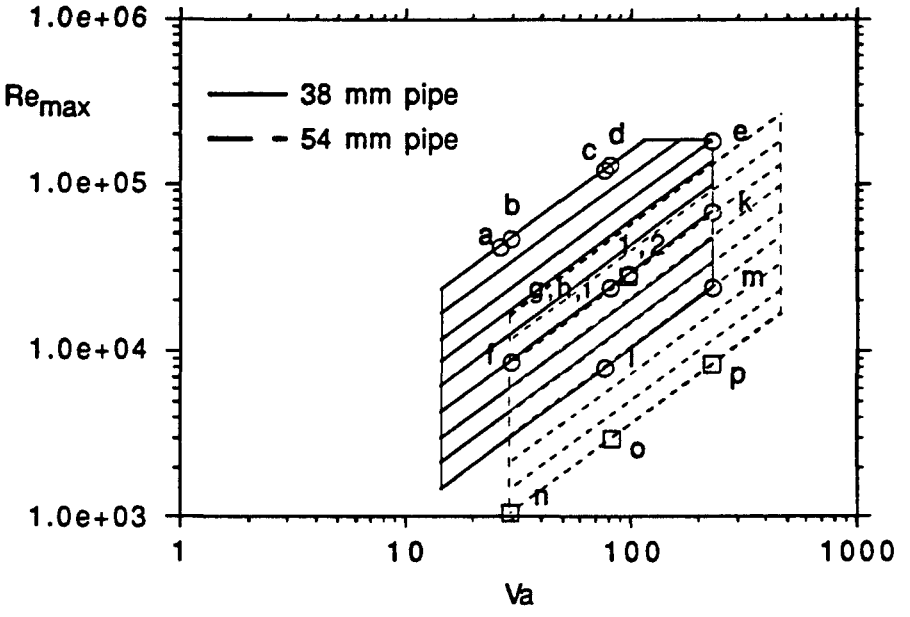

Figure 20: Map of nominal operating points for the transition study.

case	line no.	pipe diam.	bore	stroke	drive freq.	pipe length	u_{max}
		mm	mm	mm	Hz	mm	m/sec
a	1	38	356	356	0.188	2609	18.3
b	1	38	356	356	0.208	2286	20.3
c	1	38	356	356	0.558	2609	54.3
d	1	38	356	356	0.588	2286	57.2
e	3	38	356	178	1.667	2286	81.1
f	6	38	216	178	0.208	2286	3.7
g	6	38	216	178	0.588	2286	10.5
h	6	38	216	178	0.588	3048	10.5
i	6	38	216	178	0.588	1524	10.5
k	6	38	216	178	1.667	2286	29.9
1	6	38	216	178	0.700	2286	12.6
2	6	54	356	178	0.350	3239	8.5
l	9	38	127	178	0.558	2609	3.5
m	9	38	127	178	1.667	2609	10.4
n	12	54	127	178	0.104	3239	0.3
o	12	54	127	178	0.296	3239	0.9
p	12	54	127	178	0.833	3239	2.6
q	7	38	127	251.5	0.563	2286	4.94

Table 4: Dimensional description of cases in the transition study

case	line no.	Str	Va *	Re_{max} *	l/d	A_R	M_{max} *
a	1	0.0025	25.9	4.21E+04	68.5	11.9	0.05
b	1	0.0025	28.8	4.68E+04	60.0	13.6	0.06
c	1	0.0025	77.2	1.25E+05	68.5	11.9	0.16
d	1	0.0025	81.2	1.32E+05	60.0	13.6	0.17
e	3	0.0049	230.	1.87E+05	60.0	6.8	0.23
f	6	0.0133	28.8	8.63E+03	60.0	2.5	0.01
g	6	0.0133	81.2	2.43E+04	60.0	2.5	0.03
h	6	0.0133	81.2	2.43E+04	80.0	1.9	0.03
i	6	0.0133	81.2	2.43E+04	40.0	3.8	0.03
k	6	0.0133	230.	6.90E+04	60.0	2.5	0.09
1	6	0.0133	96.7	2.90E+04	60.0	2.5	0.04
2	6	0.0140	97.1	2.78E+04	60.0	2.4	0.02
l	9	0.0386	77.2	8.00E+03	68.5	0.8	0.01
m	9	0.0386	230.	2.39E+04	68.5	0.8	0.03
n	12	0.1097	28.9	1.05E+03	60.0	0.3	0.00
o	12	0.1097	82.0	2.99E+03	60.0	0.3	0.00
p	12	0.1097	231.	8.43E+03	60.0	0.3	0.01
q	7	0.0272	80.2	1.18E+04	60.0	1.22	0.014

*Assume: kinematic viscosity =16.5E-06 m^2/sec
speed of sound = 347 m/sec

Table 5: Description of cases in the transition study in terms of similarity parameters.

3.2.1. High-amplitude cases

Some researchers (e.g. Ohmi, et al. 1982, cf. section 1.3.3) claim that the flow for high values of Re_{max} (Ohmi: $Re_{max} > 2800\sqrt{Va}$) is fully turbulent and quasi-steady. This area of the operating regime appeared to provide a limiting case of transition and, thus, a good starting point.

Figure 21 shows instantaneous velocity traces of case a. The traces were taken near the wall (r/R = 0.973) and at the centerline of the pipe (r/R = 0). The probe was located at mid-length (x/d = 34.24, l/d = 68.48). Clearly, the level of velocity fluctuation, particularly near the wall (r/R = 0.973), varies greatly throughout the cycle, with a marked increase at a crank angle of approximately 25°. The flow is not turbulent throughout the cycle. The instantaneous pipe Reynolds number at the point of transition (Re ≈ 5500) is

higher than expected in steady flow. The flow remains turbulent, but decaying, until flow reversal ($\omega t \approx 180°$). It is laminar-like at the beginning of the ensuing half-cycle, however. This case is not fully-turbulent throughout the cycle and is thus not quasi-steady turbulent.

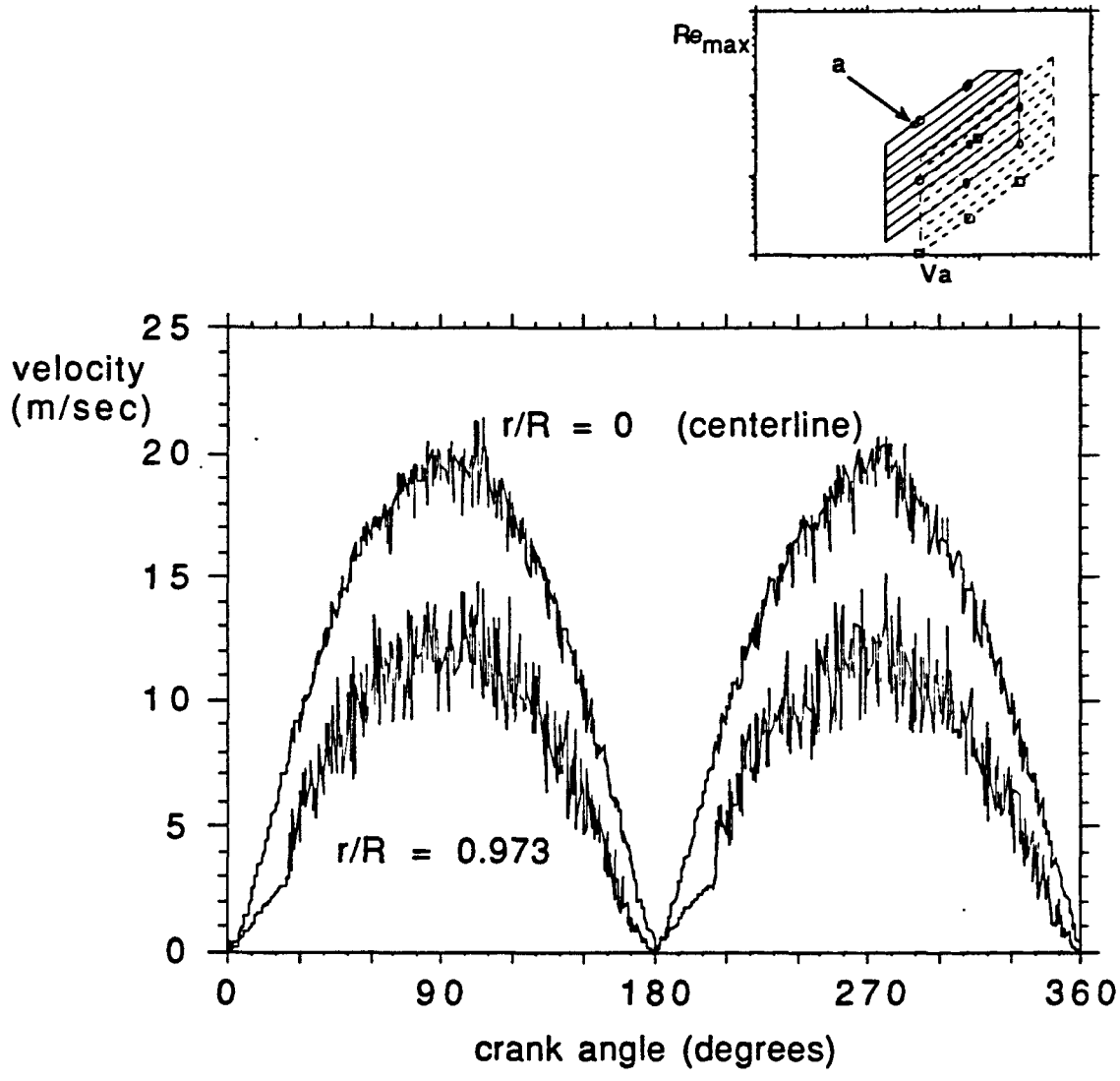

Figure 21: Instantaneous velocity transients at mid-length for case a, at x/d = 34.24 of l/d = 68.48.

Near the open end of the test section (case b–near case a on the operating map, x/d = 58), the trace of near-wall velocity fluctuation (Figure 22) shows two increases in fluctuation during the first half-cycle, the half-cycle during which the flow enters from the room. There is a rise in fluctuations at 9°, a decrease at 24.5°, and a rise again at 45.5°.

Subsequently, the level of fluctuation remains high until it decreases at 156°. This behavior near the entrance is qualitatively different from the transient at mid-length (case a) in that the flow becomes turbulent-like twice during one half-cycle.

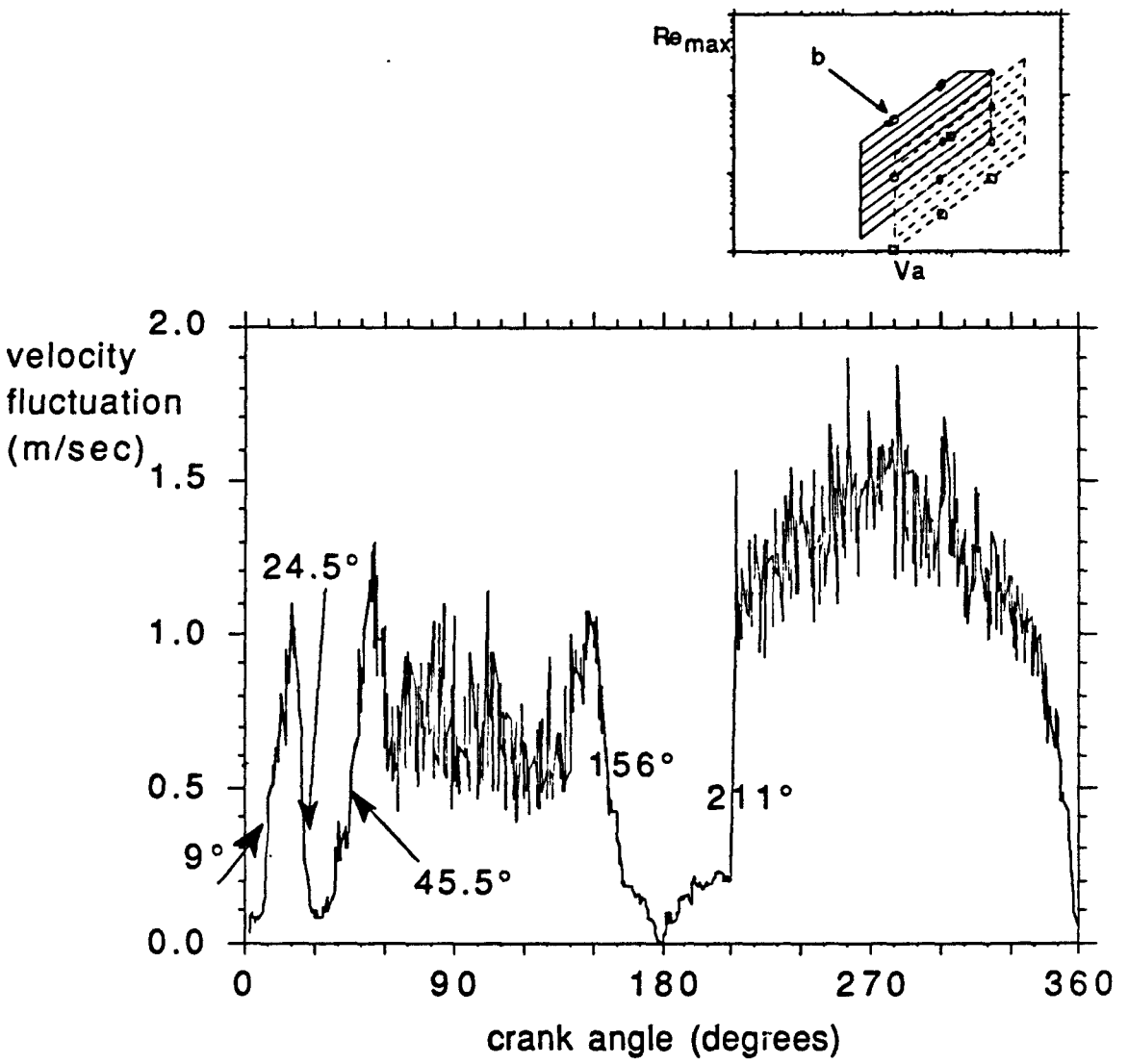

Figure 22: Velocity fluctuation near the open end for case b, at r/R = 0.96 and x/d = 58 of l/d = 60.

The time of first rise in fluctuation of case b and time of the only rise in fluctuation of case a can be computed by simply accounting for the transit time of the ingested turbulence. The integral of the velocity (bulk-mean averaged over the pipe area) and over time from the start of the cycle to the point of transition is approximately equal to the volume of the fluid in the pipe between the entrance and the probe location. This suggests

that transition is due to the arrival of incoming turbulent fluid. The crank angle of transition onset, therefore, is a function of probe location and the amplitude of fluid motion; in terms of similarity parameters: A_R and x/l. Dijkstra also observed that transition in oscillating flow is due to incoming turbulent fluid (1984, cf. section 1.3.2). This view will be discussed in detail in section 3.2.5. The apparent return from the turbulent to the laminar state for case b (24.5°) will be discussed in section 3.2.5.

Figure 23 shows velocity fluctuation levels in case d at mid-length (x/d = 30, l/d = 60). Again, there are two rises in near-wall velocity fluctuation (at 14°/194° and at 24°/204°) but the flow does not return to the laminar state.

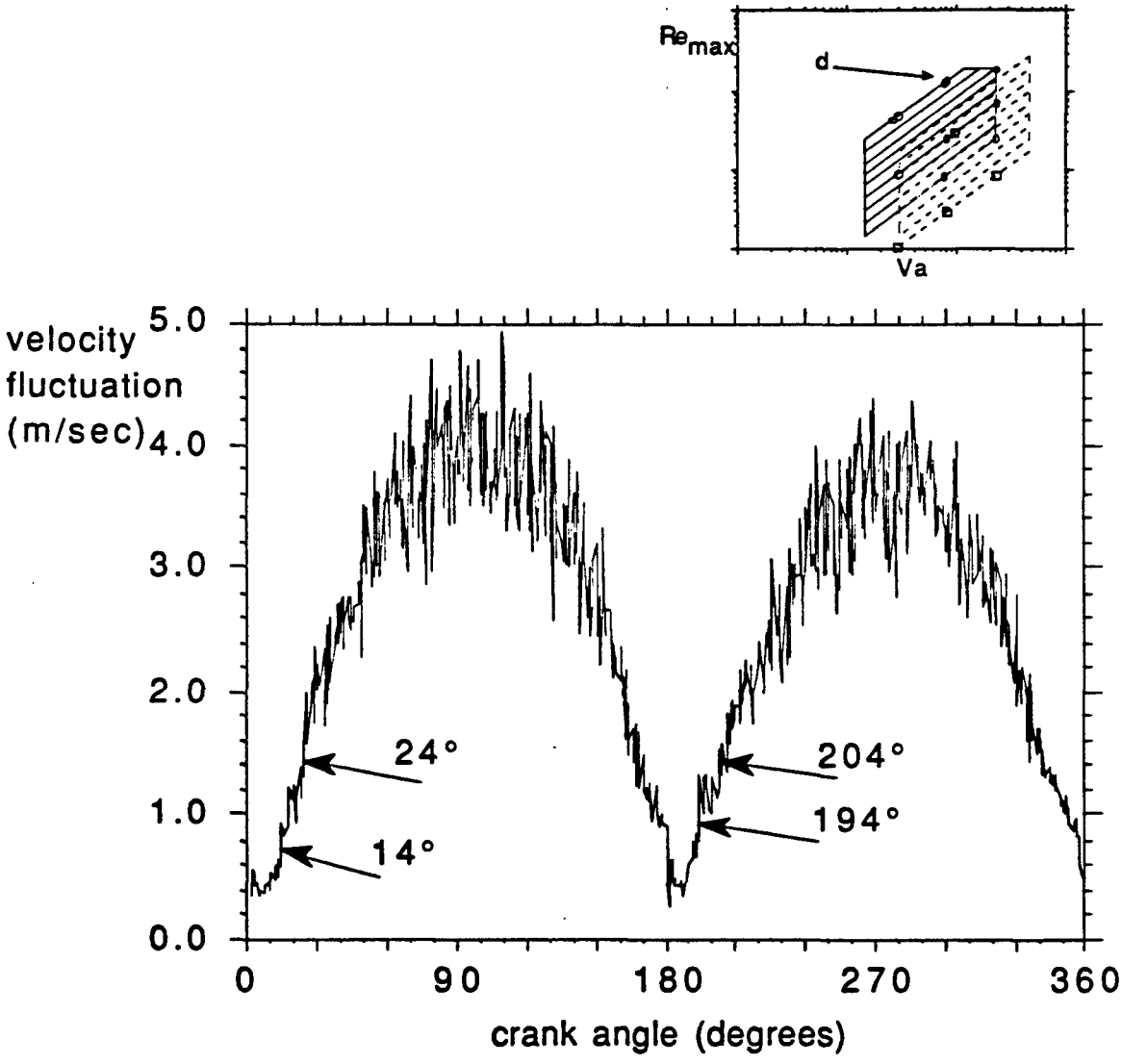

Figure 23: Velocity fluctuation at mid-length for case d at r/R = 0.96 and x/d = 30 of l/d = 60.

Near-wall fluctuation levels at mid-length (x/d = 30, l/d = 60) in case e, the upper-right corner of the map, are shown in Figure 24. Fluctuations remain large throughout the cycle. Case e seems to come closest to a fully-turbulent state. In this case, turbulence persists through the flow reversal and the strong acceleration phases of the cycle.

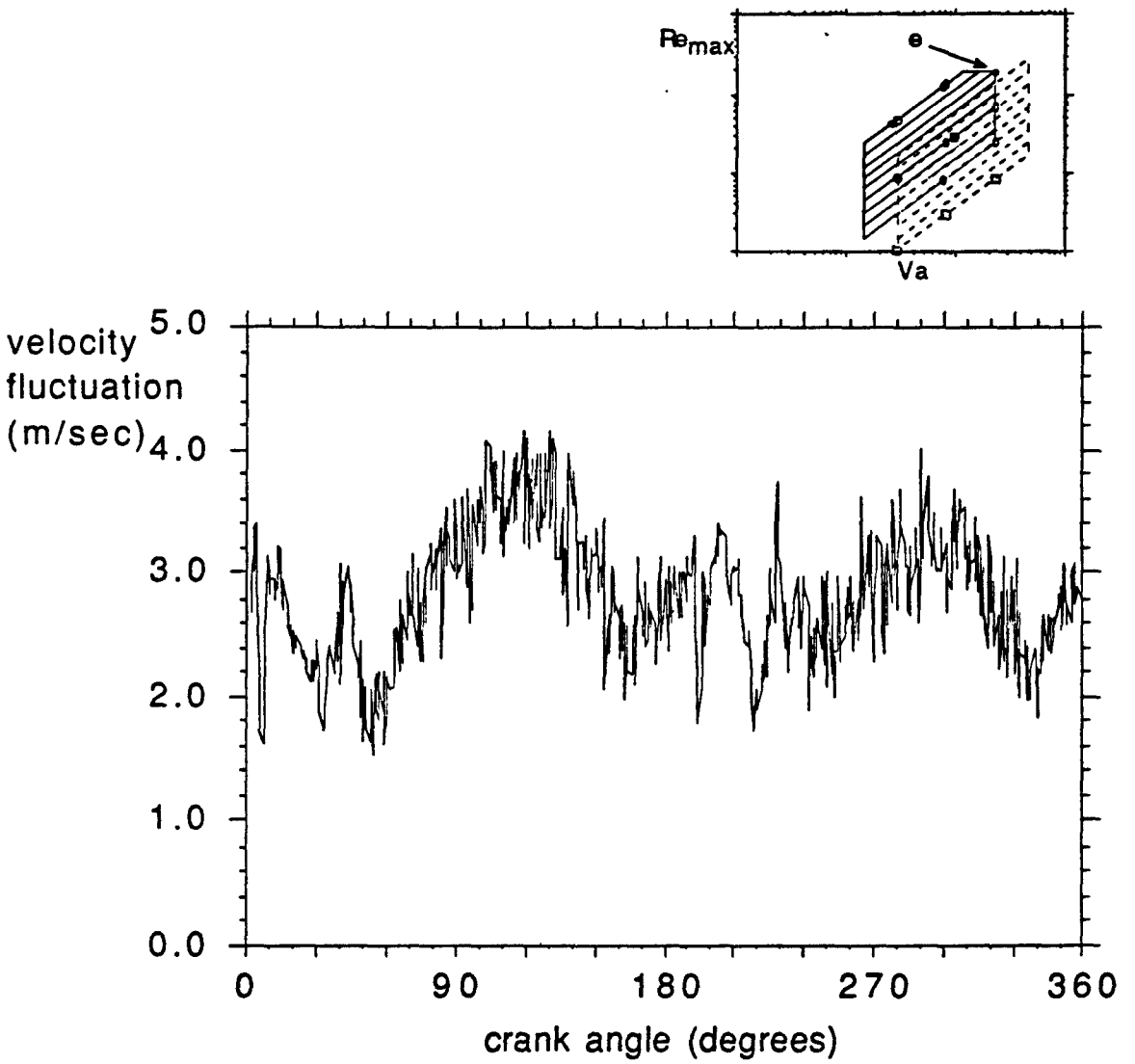

Figure 24: Velocity fluctuation at mid-length for case e, at r/R = 0.96 and x/d = 30 of l/d = 60.

Cases a through e are above the line $Re_{max} = 2800 \sqrt{Va}$, i.e. in a part of the operating regime which Ohmi et al. (1982) described as fully-turbulent and quasi-steady

(cf. section 1.3.3). Cases a, b, c and d show that a portion of each half-cycle is laminar. A mass balance shows that the first onset of transition for cases a, b and c appears to be triggered by that fluid which, at the time of flow reversal, was outside the pipe. Case d (Figure 23) does not fit this pattern, however, because the first sharp rise in fluctuation level takes place before fluid from the pipe entrance could have arrived. Thus, transition was by another mechanism which transpired before the convected turbulent flow arrived to trigger it. Case b (Figure 22) shows that, at least near the pipe entrance, the flow may not remain turbulent throughout the cycle once it has become turbulent-like. That is, a laminar flow, disturbed by the incoming turbulence, need not be triggered to turbulence. The tentative conclusions from the cases discussed so far are:

- Transition is, in most cases, triggered by incoming turbulent fluid.
- Transition, characterized by higher turbulence levels, may start by another mechanism before incoming turbulent fluid arrives.
- Transition onset is a function of the axial location and A_R if it is triggered by incoming turbulent fluid.
- Though the flow assumes a turbulent-like nature due to the effect of the convected disturbance in the core, it may revert back to a laminar appearance when the disturbance passes.

3.2.2. Medium-amplitude cases

Case f exhibits qualitatively different behavior than displayed by the previous cases. Figure 25 shows a trace of near-wall velocity fluctuation near the open end (x/d = 58, l/d = 60) of the test-section. The fluid coming in from the room (first half-cycle) causes a rise in fluctuation level. The flow reverts to the laminar state after the passage of the fluid which, at the time of flow reversal, was in the nozzle between the heat exchanger and the pipe inlet. Note that downstream of this turbulent fluid is calm fluid which was outboard of the heat exchangers upon flow reversal and, after flow reversal, was drawn through the heat exchanger and the nozzle before entering the test section. The heat exchanger reduced the turbulence to a fine-grained nature and the nozzle strained the flow, thus dissipating the turbulence. Apparently, in case f, higher fluctuation levels can be sustained only when turbulent incoming fluid is present. The boundary layer was not ready to pass through transition to sustained turbulence while the fluid was present. The turbulent-like flow, then, was actually a highly disturbed laminar flow.

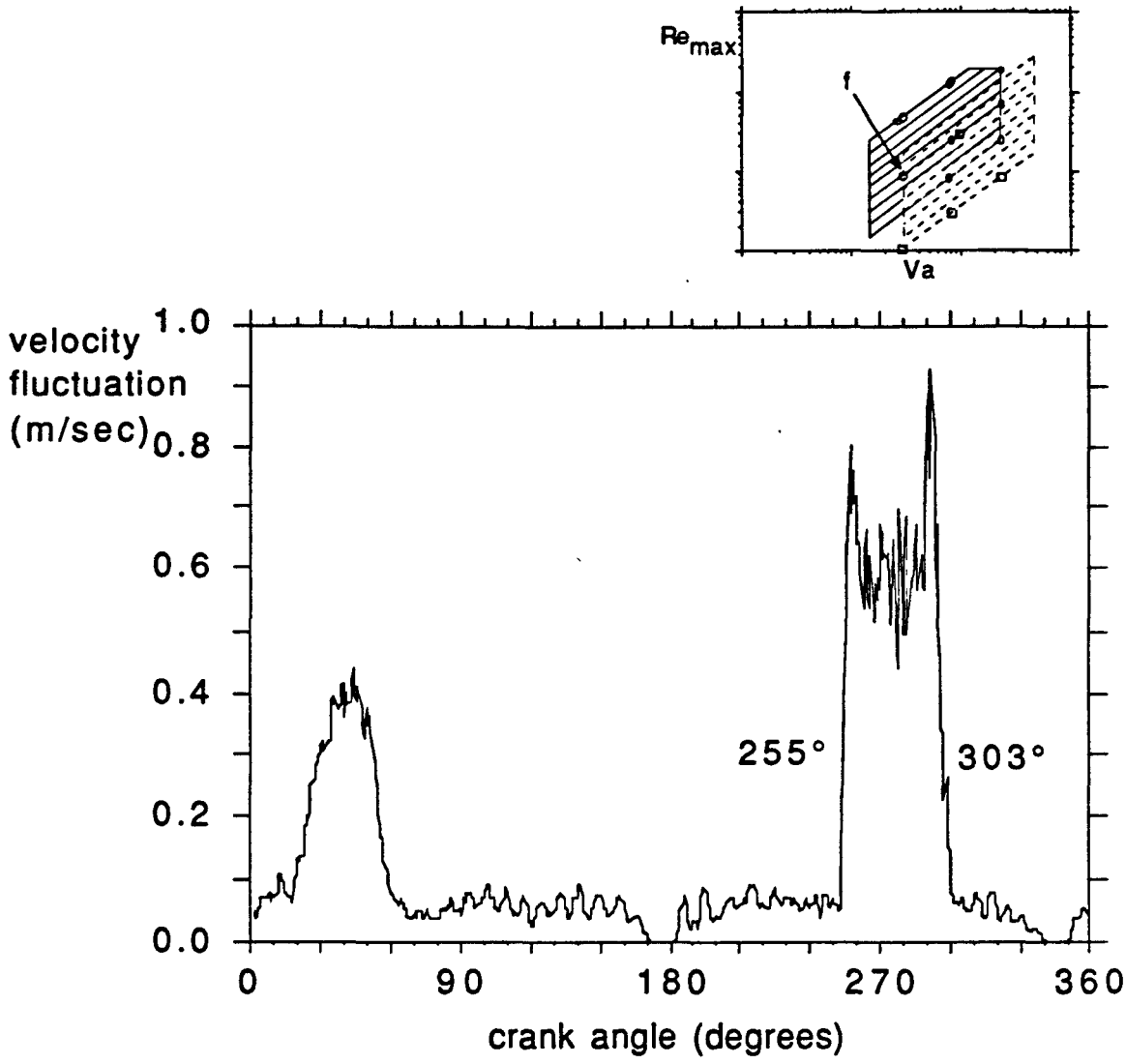

Figure 25: Velocity fluctuation near the open end, case f, at r/R = 0.96 and x/d = 58, of l/d = 60.

It is instructive to compare the present case, f, to case b (Figure 22). In case b, near the pipe entrance, the flow also reverts to the laminar state but undergoes transition later. In case f, the flow remains laminar throughout the rest of the half-cycle and throughout the entire pipe. The flow is apparently too stable to maintain a turbulent state at any point in the cycle, anywhere in the tube, except when in the presence of high turbulent kinetic energy fluid which has been convected into the tube.

In case g, as in case f, the fluid returns to the laminar state near the open pipe end (x/d = 58, l/d = 60). This may be seen in the first half-cycle of Figure 26. Further

downstream from the pipe entrance, however, the flow undergoes transition and remains turbulent for the rest of the half-cycle. When the turbulent slug reaches the probe, during the second half cycle, the fluid has traveled 58 diameters downstream of the inlet. Upon arrival, there is a sharp rise in turbulent fluctuation, as observed in the high-amplitude cases. Under these conditions, the flow does not return to the laminar-like state until flow reversal and the subsequent high-acceleration portion of the next half-cycle.

The influence of the pipe length was studied by comparing case g (l/d = 60) to cases h (l/d = 80) and i (l/d = 40). The change in (l/d) also changes A_R, since the Strouhal number is identical for cases g, h and i:

$$A_R = \frac{2}{Str}\frac{d}{l}$$

In all cases, the probe is located 2 diameters from the open end. During the first half-cycle, the flow enters through the open end. Figures 26 (x/d = 58, l/d = 60), 27 (x/d = 38, l/d = 40) and 28 (x/d = 78, l/d = 80) show that transition to turbulence and relaminarization occur at the same positions in the first half-cycle. The length of the pipe downstream of the probe location apparently does not matter. This implies that the flow does not "remember" the previous half-cycle in this case. This is expected since "transition" is effected by the disturbance which is convected from the open end.

In the second half-cycle, the three cases differ in the time to transition. This is the case because the incoming turbulent fluid must travel different distances to reach the probe location in each case:

length l/d	case	axial location x/d	angle of transition onset	Figure
40	i	38	242°	27
60	g	58	253°	26
80	h	78	260°	28

Table 6: Variation of transition onset with pipe length

Qualitatively, the same transition process occurs in the two shorter pipes (case i, l/d = 40, and case g, l/d = 60). In the longest pipe, however, (case h, l/d = 80), the increase in velocity fluctuation proceeds in two steps (Figure 28). At 245°, there is an increase. This is prior to the arrival of the turbulent slug. At 260°, the "time" of arrival of the first fluid that entered the pipe after flow reversal, there is a strong increase in turbulent

fluctuation. The question of which event marks laminar-to-turbulent transition will be addressed later with the use of the measured velocity profiles. The first transition, prior to the arrival of the turbulent fluid from the upstream plenum, again indicates that transition from a low-turbulence-intensity to a high-turbulence-intensity flow may occur without the influence of the advected high-turbulent-kinetic-energy slug.

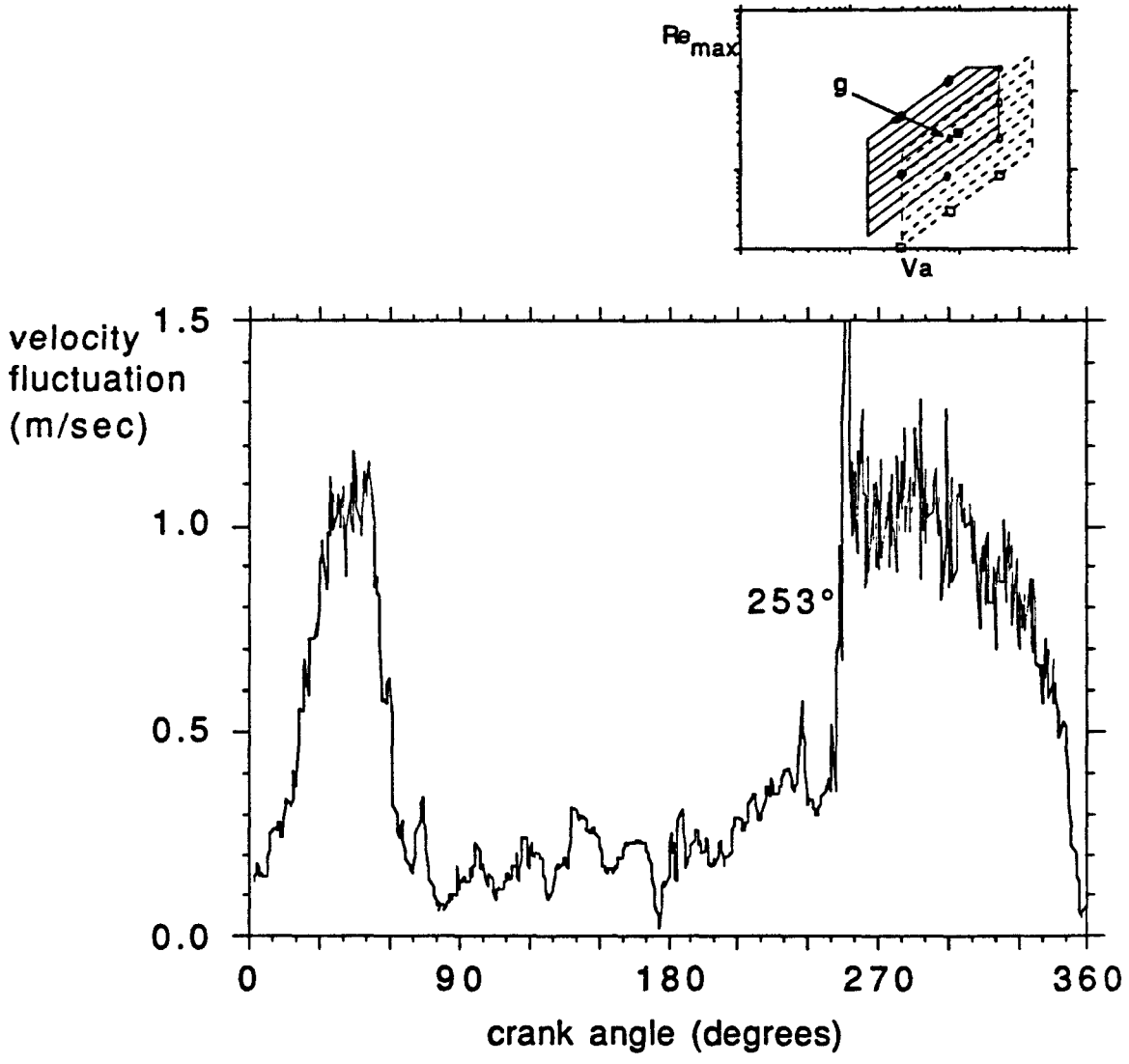

Figure 26: Velocity fluctuation near the open end, case g, at r/R = 0.96 and x/d = 58 of l/d = 60.

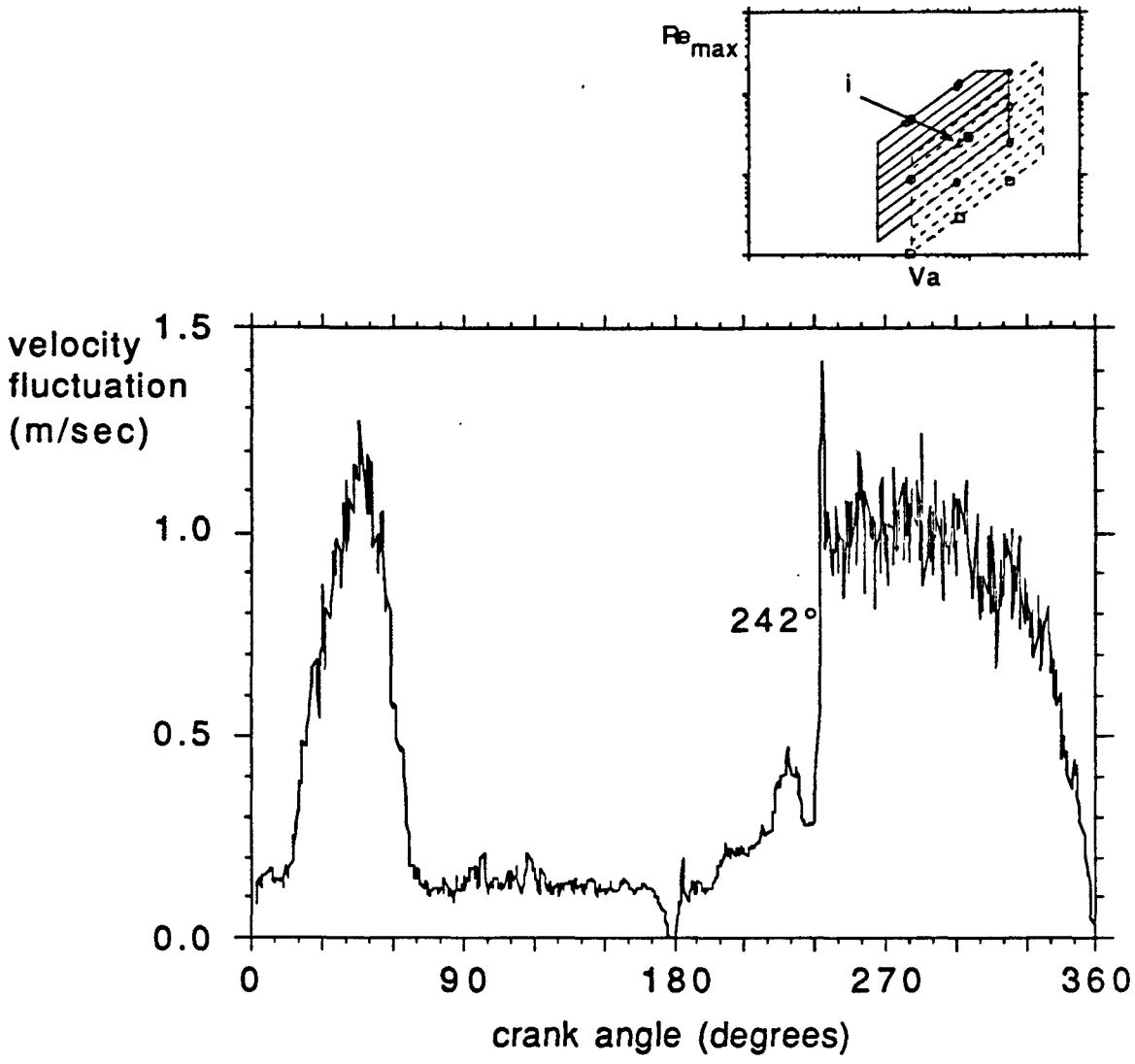

Figure 27: Velocity fluctuation near the open end, case i for which x/d = 38, l/d = 40, and r/R = 0.96

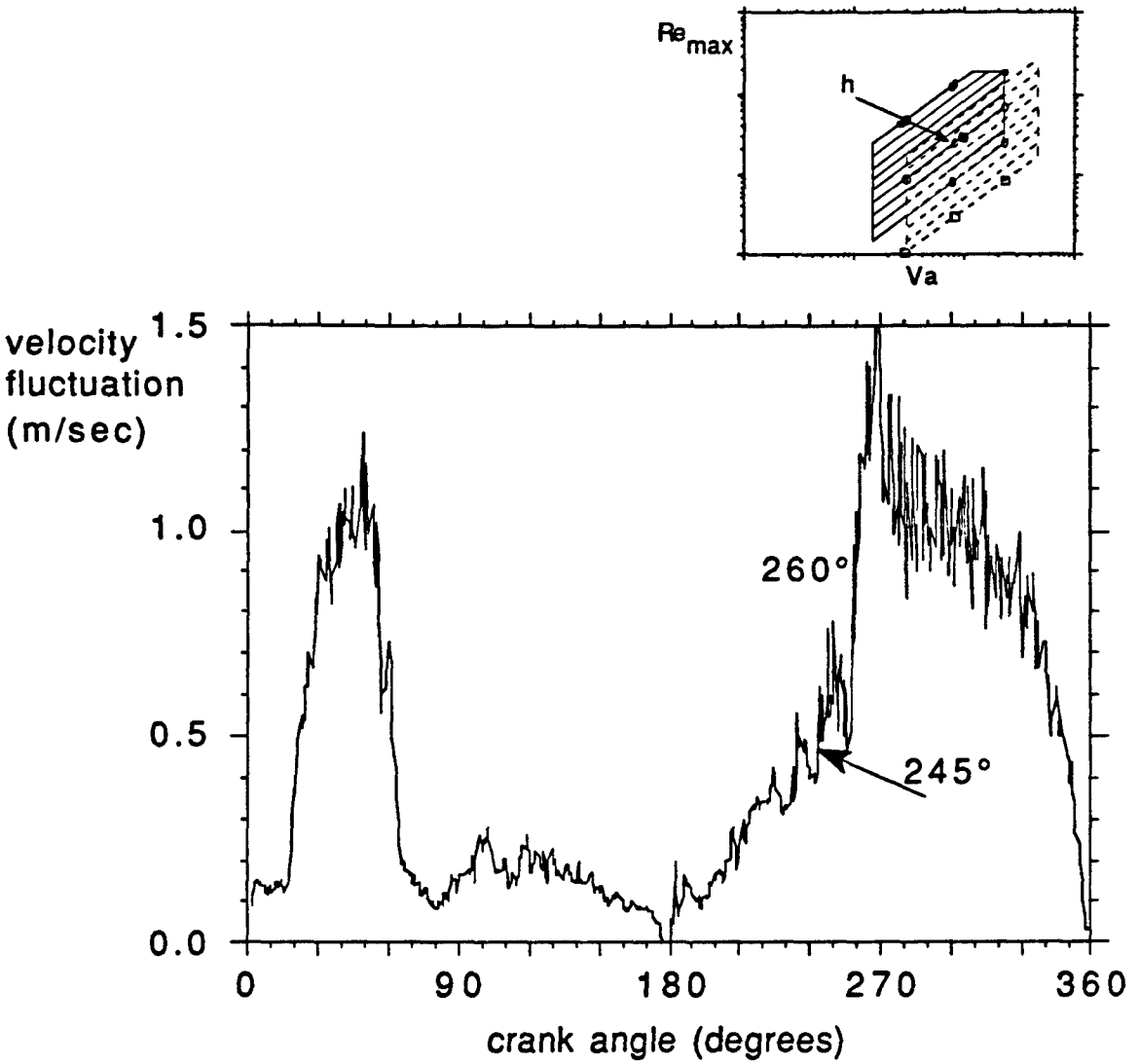

Figure 28: Velocity fluctuation near the open end, case h for which x/d = 78, l/d = 80, and r/R = 0.96

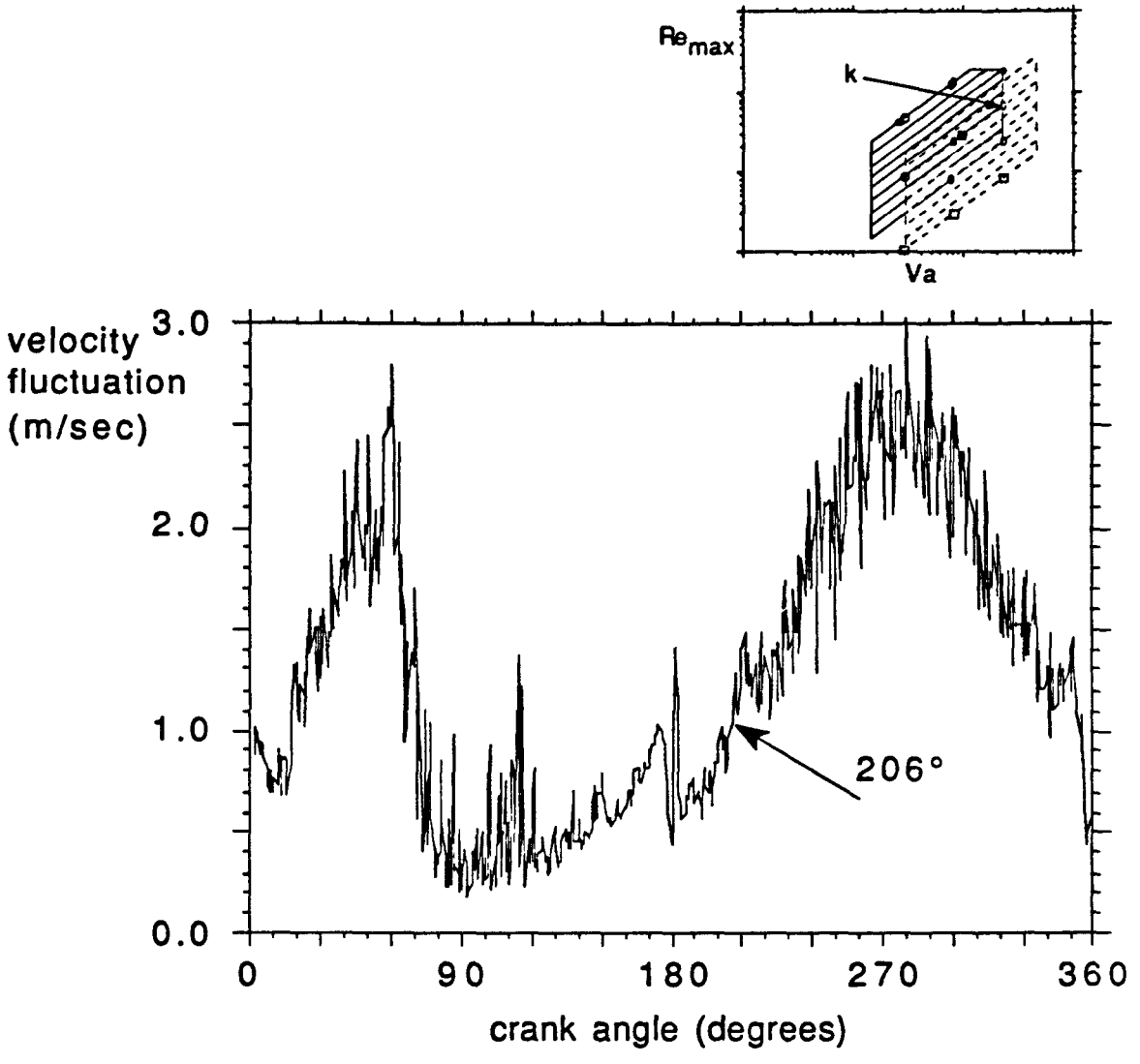

Figure 29: Velocity fluctuation near the open end, case k, at r/R = 0.96 and x/d = 58 of l/d = 60.

This concludes the discussion of the length effect. The remainder of this section is based on data with a fixed pipe length of l/d = 60.

In case k (Fig. 29), near the open end (x/d = 58), the drop in turbulent activity during the first half-cycle is less clearly defined. The fluctuation levels in the first half-cycle do, however, drop after the incoming turbulent fluid has passed. This is somewhat analogous to the return to laminar flow in case g, although, similar to case e, the turbulence is never completely dissipated. One could say that this is fully-turbulent in that it displays some turbulence throughout the cycle but one wonders whether it would have the characteristics of a mature turbulent flow throughout the cycle.

In the second half-cycle, there is a jump in the level of velocity fluctuation at 206°, i.e. before the turbulent incoming fluid reaches the probe location. This is similar to the laminar-turbulent transition observed near the exit (x/d = 78, l/d = 80) in case h (Fig. 28). Thereafter, the variation of turbulent fluctuation shows no additional sharp rises throughout the remainder of the cycle. One wonders whether the turbulent slug had much impact in this case. It seems as though the flow was fully turbulent when the slug arrived.

The medium-amplitude results contribute the following additional observations:

- At low values of Re_{max} and/or Va, the flow may appear turbulent only as long as turbulent fluid that entered the pipe is present. This may be true throughout the cycle (both directions) and throughout the pipe.
- If there is transition, it is usually triggered by incoming turbulent fluid.
- Only far downstream from the pipe inlet may transition occur prior to being triggered by incoming fluid.

3.2.3. Low-amplitude cases

Traces for the low amplitude cases l through p are not shown. Cases l and m agree with the general trends observed above. In both cases the probe was located at mid-length. Transition occurred approximately at the time when the incoming turbulent fluid arrived.

Cases n, o, and p confirm the transition observations made by Iguchi, et al. (1982), Ohmi, et al. (1982), and Grassmann and Tuma (1979) which predict laminar flow throughout the entire cycle in this area. The measurements show laminar unsteadiness but no sign of the higher-frequency fluctuations characteristic of turbulent flows.

3.2.4. Similarity

The use of the results of this experiment for the prediction of transition in oscillating flows hinges on the proper choice of similarity parameters. Similarity parameters were derived in section 2 from the momentum equation, but similarity in the boundary conditions and in the geometry must also be maintained. An experiment was performed to test how robust the chosen set of similarity parameters is and which aspects of similarity may have been neglected in designing the apparatus and test section.

Cases 1 and 2 are designed to have nominally identical similarity parameters but to differ in dimensional parameters such as pipe diameter, frequency, etc. (cf. Table 2). Since the present work addresses the transition process, similarity was checked with respect to transition. The cases used to assess similarity are also those documented in detail, i.e. profiles of velocities and velocity fluctuations are taken. The profiles will be discussed in section 3.2.7. Because they were taken with a boundary-layer probe, the measurements reported for the similarity cases are only valid for one half-cycle.

A comparison of the traces of near-wall velocity fluctuation at $x/d \approx 8$ may be made by referring to Fig. 30 (similarity case 1, $x/d = 7.67$) and 31 (similarity case 2, $x/d = 7.77$). In both cases, transition starts at approximately 211°. The relaminarization, however, begins at 248° in case 1 and at 228.5° in case 2. This difference may be explained by the different nozzle volumes in the two cases. In case 1, the nozzle provides the contraction from the 127 mm I.D. flexible joint to a 38 mm I.D. pipe, in case 2 the contraction is from 127 mm to 54 mm, in both cases over a 152 mm length. The length of pipe corresponding to the nozzle volume is 22.3 diameters long in case 1, 7.95 diameters long in case 2. Therefore, the period during which fluctuation levels are high is longer in case 1 than in case 2. Consequently, similarity is only maintained with respect to the initial rise in fluctuation. The return to the laminar-like state and the second rise in fluctuation level, which depend on the ratio of nozzle volume to the volume of the pipe between the inlet and the probe, are specific to the inlet geometry and cannot be generalized.

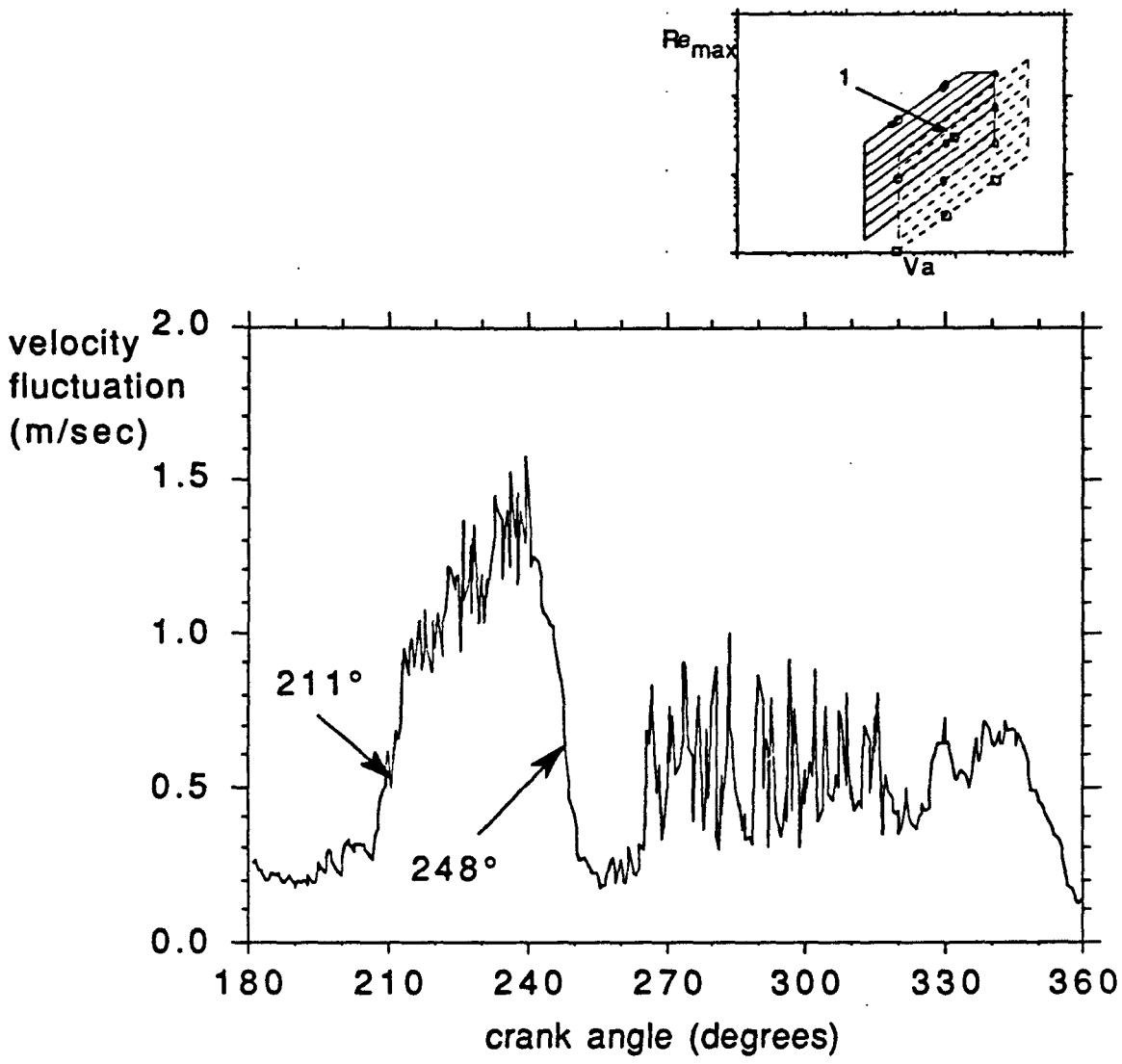

Figure 30: Velocity fluctuation near the drive end, Similarity case 1, at r/R = 0.96 and x/d = 7.67 of l/d = 60.

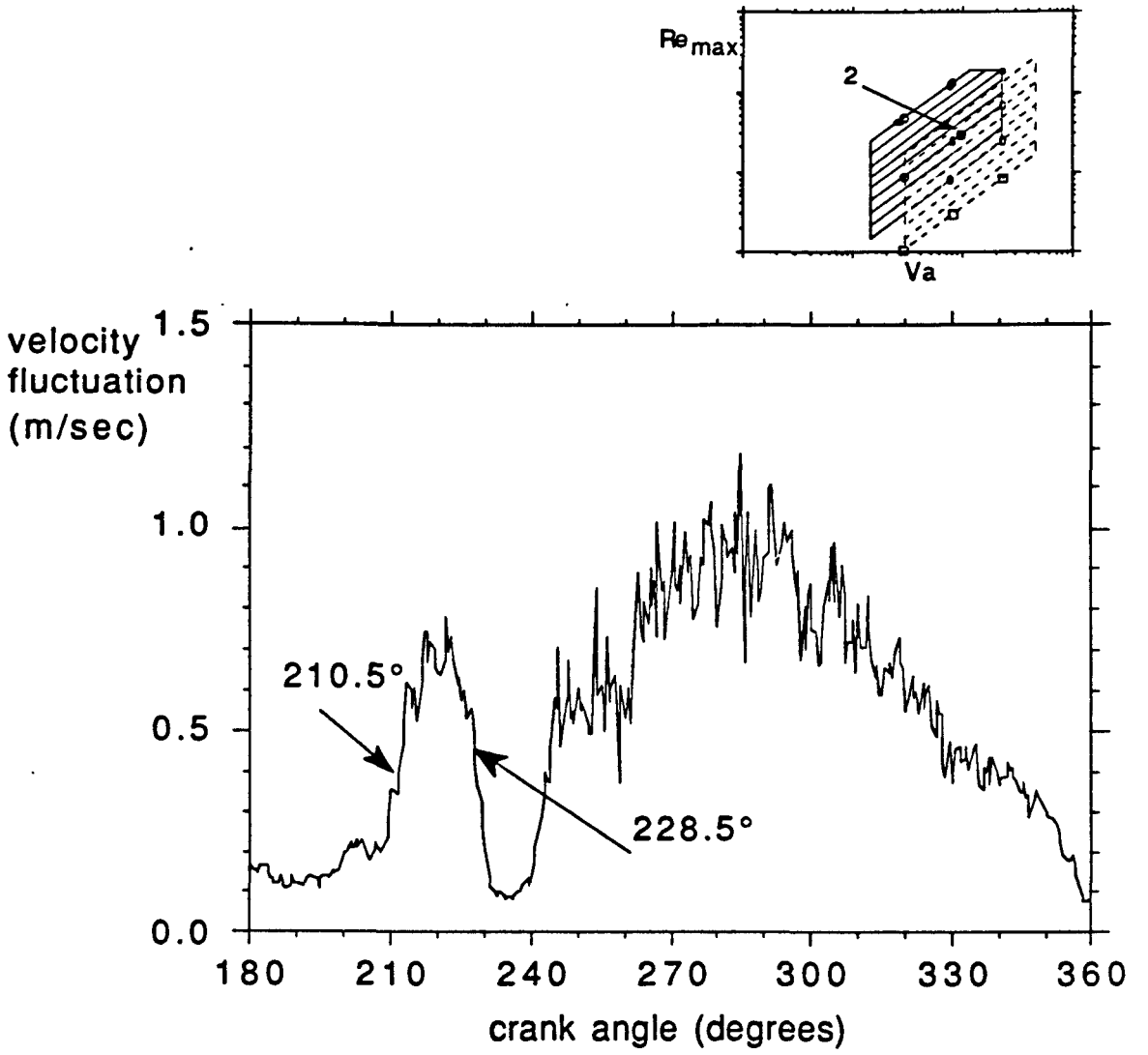

Figure 31: Velocity fluctuation near the drive end, Similarity case 2, at r/R = 0.96 and x/d = 7.77 of l/d = 60.

3.2.5. Convective triggering of transition

The observation that the first rise in velocity fluctuation is triggered by the incoming fluid suggests a simple model for the prediction of transition. It is based on the assumption that turbulent fluid triggers transition as it moves through the pipe at some appropriate velocity, here assumed to be the bulk-mean velocity.

Assume that ...

- the incoming turbulent fluid travels in the axial direction with the bulk-mean velocity,
- the piston velocity is a sine-function in crank-angle and time, and
- the fluid density in the cylinder and the test section is uniform and constant throughout the cycle.

Then the distance which the fluid has traveled in the axial direction may be calculated by integrating the sinusoidal bulk-mean velocity from the crank angle of flow reversal to the crank angle of transition onset. The flow reverses at or near the top dead center of the drive (crank angle = 0°) and the bottom dead center (crank angle = 180°). If the simple convective model of transition is correct, the axial position of the turbulent slug leading edge should correspond with the probe position. Figure 32 shows a good comparison.

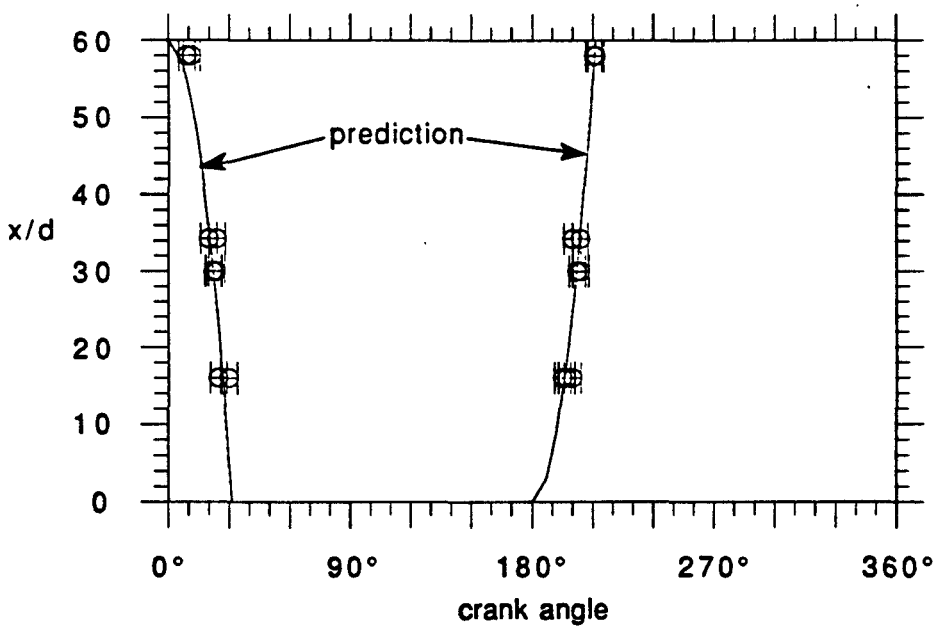

Figure 32: Predicted and measured transition in high-amplitude cases

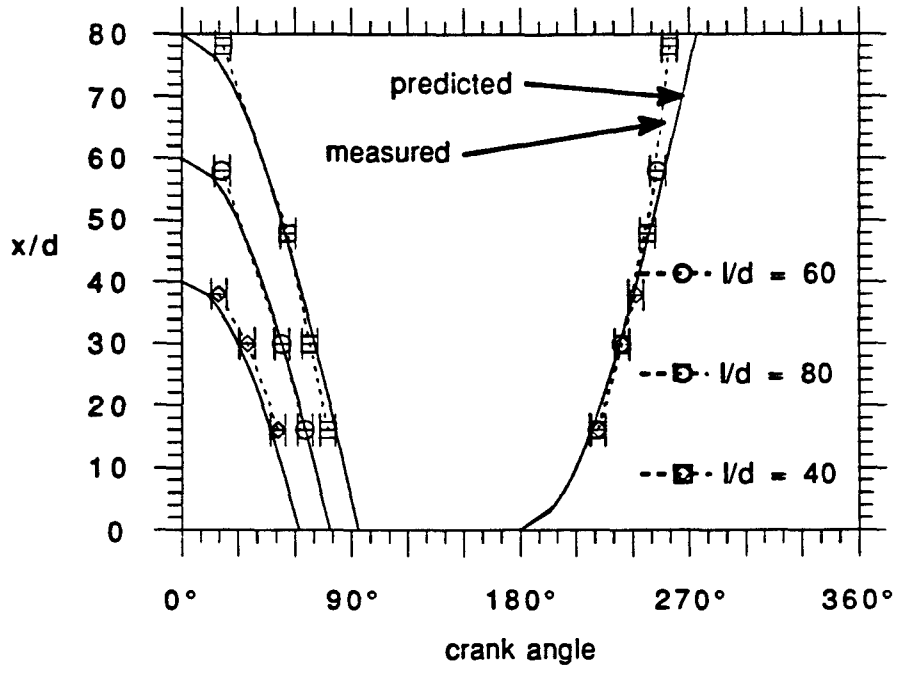

Figure 33: Predicted and measured transition in medium-amplitude cases for three pipe lengths.

The increase in ensemble-averaged velocity fluctuation values from a low, laminar value to a higher, turbulent value is typically not instantaneous, but occurs over approximately 4° of crank angle. This major contribution to the uncertainty in transition position is represented by the uncertainty bars shown in Fig. 32.

Figure 33 provides the same comparison at a higher Strouhal number and for three different pipe lengths, cases g,h, and i. The prediction is generally consistent with the observed results, but there is a large deviation near the pipe inlet, at (l-x)/d = 2. There are two reasons for this discrepancy:

(1) During the inflow (first half-cycle), the turbulent fluctuations increase gradually with time from the laminar to the turbulent level. In Figure 22, for example, the rise in velocity fluctuation during inflow extends over 15° and during the outflow, when the boundary layer is tripped to a turbulent state, the rise in velocity fluctuation extends over 4°. Therefore, the imprecision in determining the point of transition is greater during inflow than during the outflow. The transition from the nozzle, where large-scale eddies survive through flow reversal, to the pipe, is gradual. There, thus, is some ambiguity concerning precisely what fluid, upon flow reversal, constitutes the turbulent slug. The fluid which was very near the tube entrance during flow reversal probably is not instrumental in

triggering transition. Therefore, the triggering of transition occurs somewhat later than predicted by this simple method. The error is visible only for measurements very near the tube entrance.

(2) During the outflow (second half-cycle), the turbulent fluid arrives at the exit earlier than predicted because the boundary layer growing on the pipe wall displaces fluid into the core and thereby accelerates the core fluid. Therefore, the simple convective model should predict transition onset later than it actually occurs. This is observed for the case of the longer pipe (l/d = 80, case h) where transition occurred earlier than expected near the open end (x/d = 78).

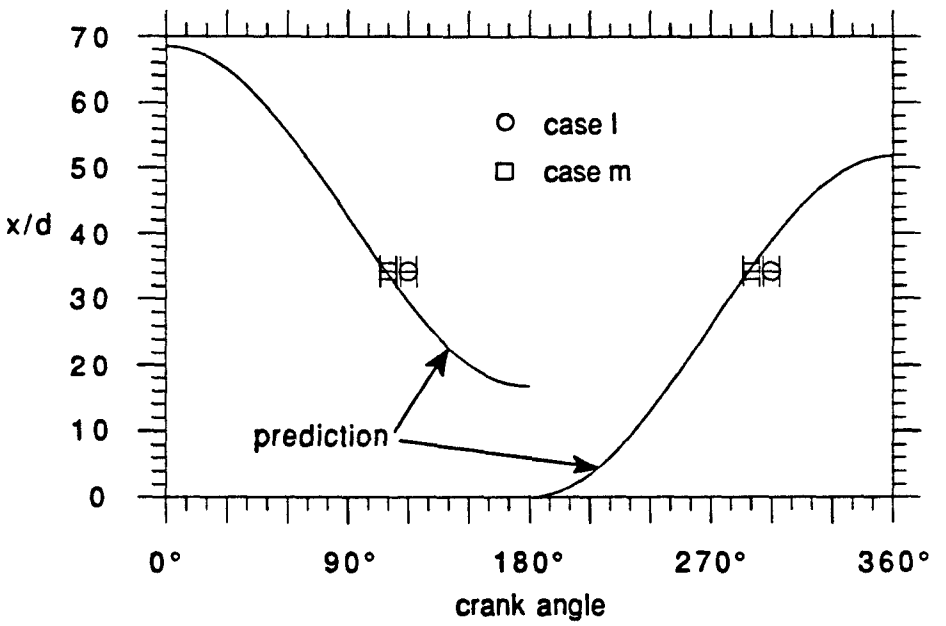

Figure 34: Predicted and measured transition in low-amplitude cases.

Figure 34 shows that the model holds for case m but there is a 10° phase delay of the observed values in case l. This discrepancy may again be due to acceleration of the flow in the core. In this case, the development length is quite long. During the development, the flow would remain laminar-like, thus, a laminar profile, which has a very high core-to-bulk velocity ratio, develops.

3.2.6. Non-convective triggering of transition

Figures 32 through 34 include only those transitions which are due to convective triggering, i.e. the arrival of incoming turbulent fluid. The discussion of cases d and h in section 3.2.1 shows that transition may occur before the arrival of incoming turbulent fluid and in case f, the flow is turbulent only while convected turbulent fluid is passing the measurement station, remaining laminar throughout the remainder of the cycle.

Figure 26 (case g, x/d = 58) illustrates perhaps most clearly that transition can be triggered and turbulence sustained only if the boundary layer is sufficiently unstable to be triggered. Otherwise it reverts to the laminar behavior after the turbulent fluid passes.

The observations of transition from laminar to turbulent flow are best summarized by taking a Lagrangian point of view, traveling with the bulk-mean fluid motion.

- Turbulent fluid entering the pipe remains turbulent.
- Laminar fluid entering the pipe and that fluid which was in the pipe at flow reversal tend to remain laminar, but the growth of the boundary layer may, under certain conditions, lead to boundary layer transition under that laminar core before the convected turbulent fluid arrives.

In section 3.2.3., cases were presented in which transition was not observed:

- In the lower part of the parameter map (cases n,o,p on Figure 20) there is a region in which the fluid remains laminar under all circumstances encountered in this study.
- There appears to be a condition near the top of the parameter range covered (case e in Figure 20), where the flow is fully turbulent throughout the cycle.

3.2.7. The effects of convectively and non-convectively triggered transition

To this point, a sharp rise in velocity fluctuation was taken as evidence of transition to turbulent flow. Turbulent flow, however, is characterized by eddy-transport and not merely by unsteadiness. To check whether a rise in fluctuation is associated with enhanced transport of momentum, velocity profiles from similarity case 1 are now discussed.

The trace of velocity fluctuation in Figure 35 was taken with a boundary layer probe facing toward the open end of the test section (x/d = 58.3, near the open end), therefore only the first half of the cycle is shown. The trace shows a sharp increase in velocity fluctuation at approximately 4.5°. The level of fluctuation remains high until the turbulent fluid from the nozzle has passed, after which it decreases gradually, reaching a low level at 60°.

Figure 36 shows a profile at 4° with higher near-wall than center-line velocity. This higher near-wall velocity is because the fluid at the pipe center had a higher momentum in the previous half-cycle and was therefore slower to respond to the reversal of the pressure gradient than was the near-wall fluid. Since there is no turbulent eddy transport at this point in the cycle, there is little communication between near-wall and core fluid. This is similar to the behavior of oscillating flow that remains laminar throughout the cycle (cf. section 1.3.1.). At 30°, the profile shows a more uniform velocity and a much thicker boundary layer which is a sign of higher cross-stream momentum transport. This transport is presumably that of turbulent eddy transport. This agrees well with the higher near-wall velocity fluctuation seen at 30° in the trace of velocity-fluctuation (Fig. 35). At 60°, the boundary layer appears thinner again, which correlates well with weaker cross-stream transport expected from the low fluctuation levels shown in the trace (Fig. 35) at this crank-angle. The core fluid continues to accelerate but the decreased turbulent transport has isolated more of the near-wall flow from the wall shear – allowing it to be accelerated, like the core flow, by the pressure gradient.

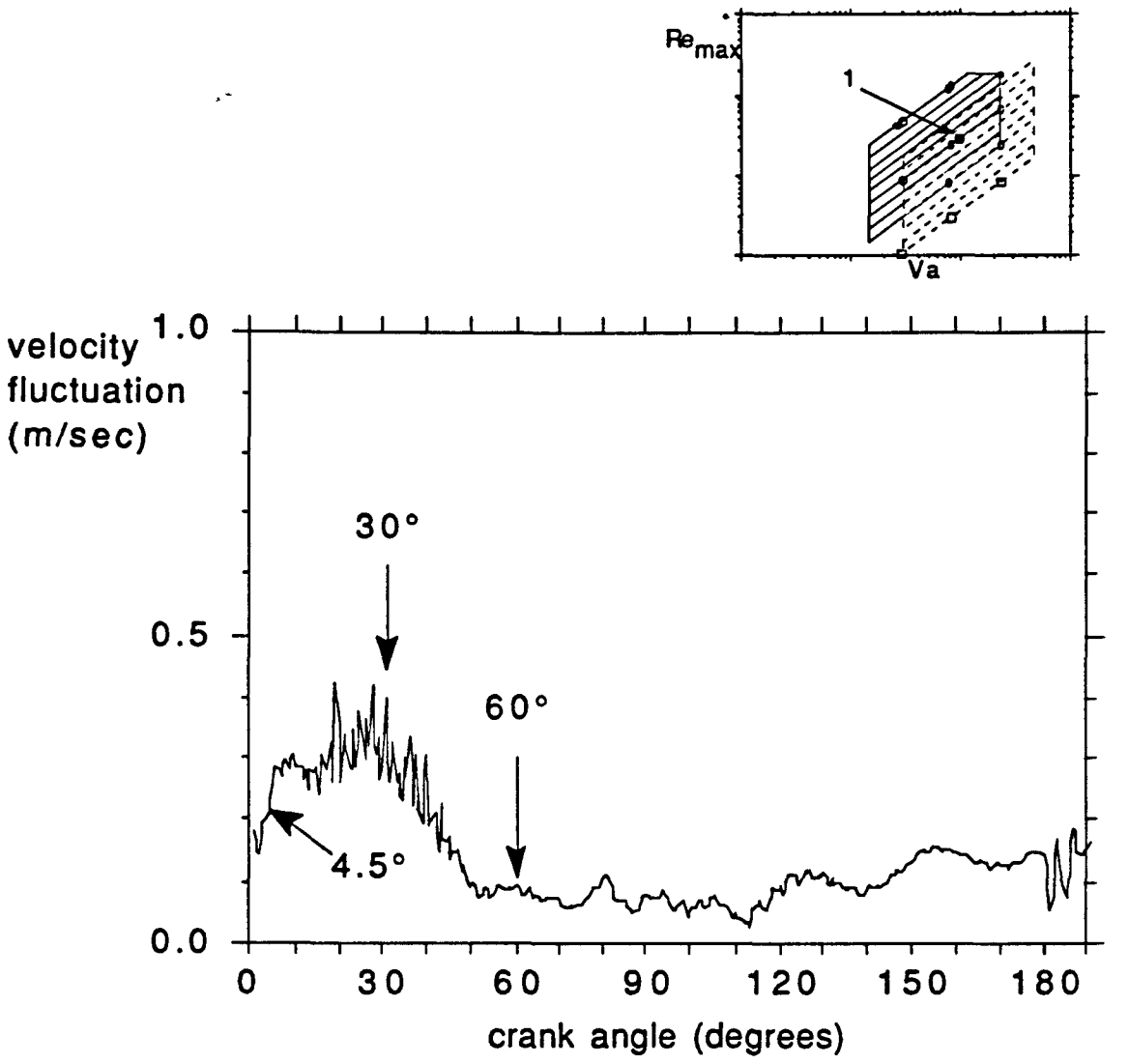

Figure 35: Velocity fluctuation near the open end, case 1, at r/R = 0.96, (y/d = 0.02) and x/d = 58.3 of l/d = 60 (near the entry end).

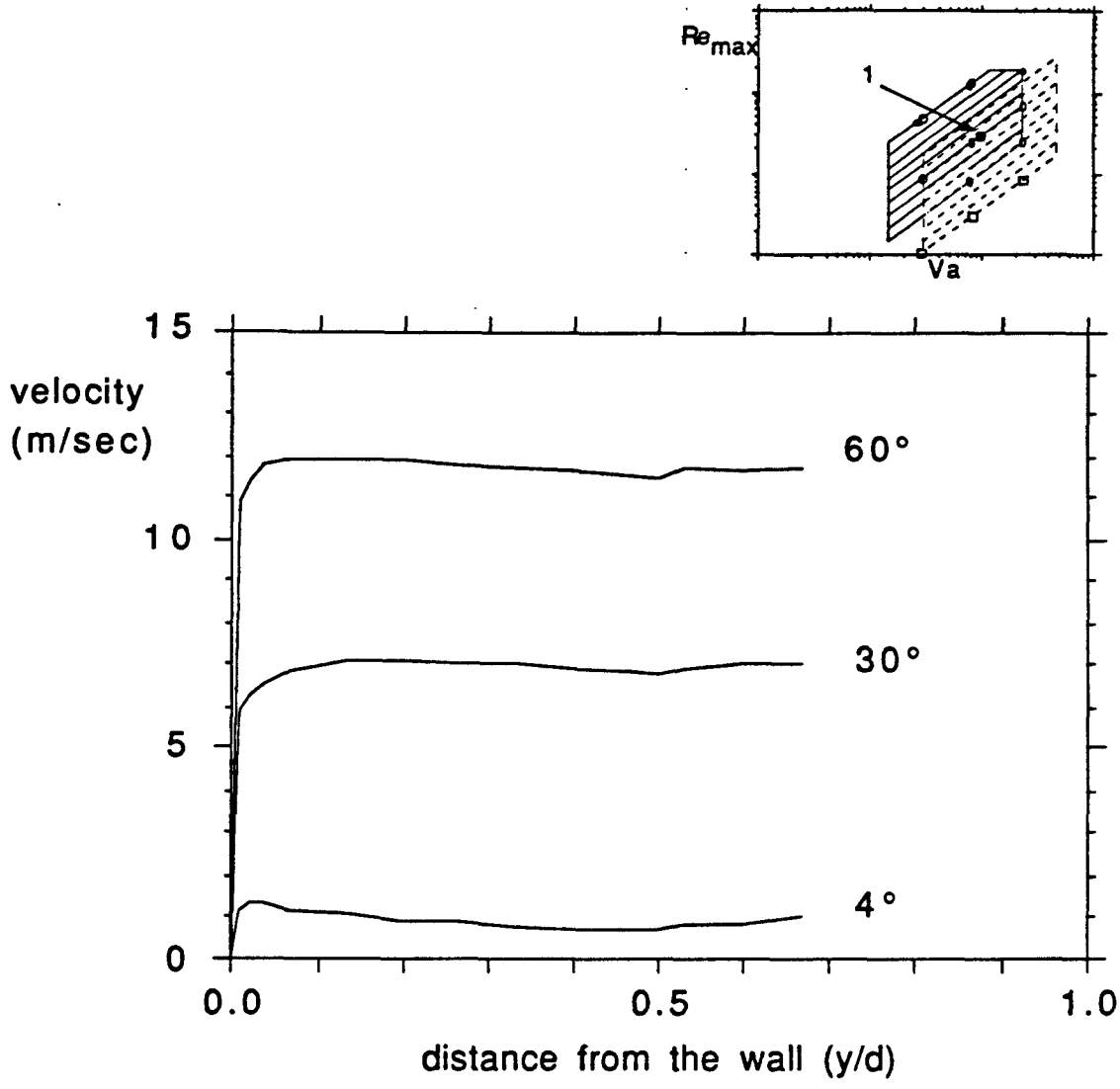

Figure 36: Velocity profiles near the open end, case 1, at x/d = 58.3 of l/d = 60.

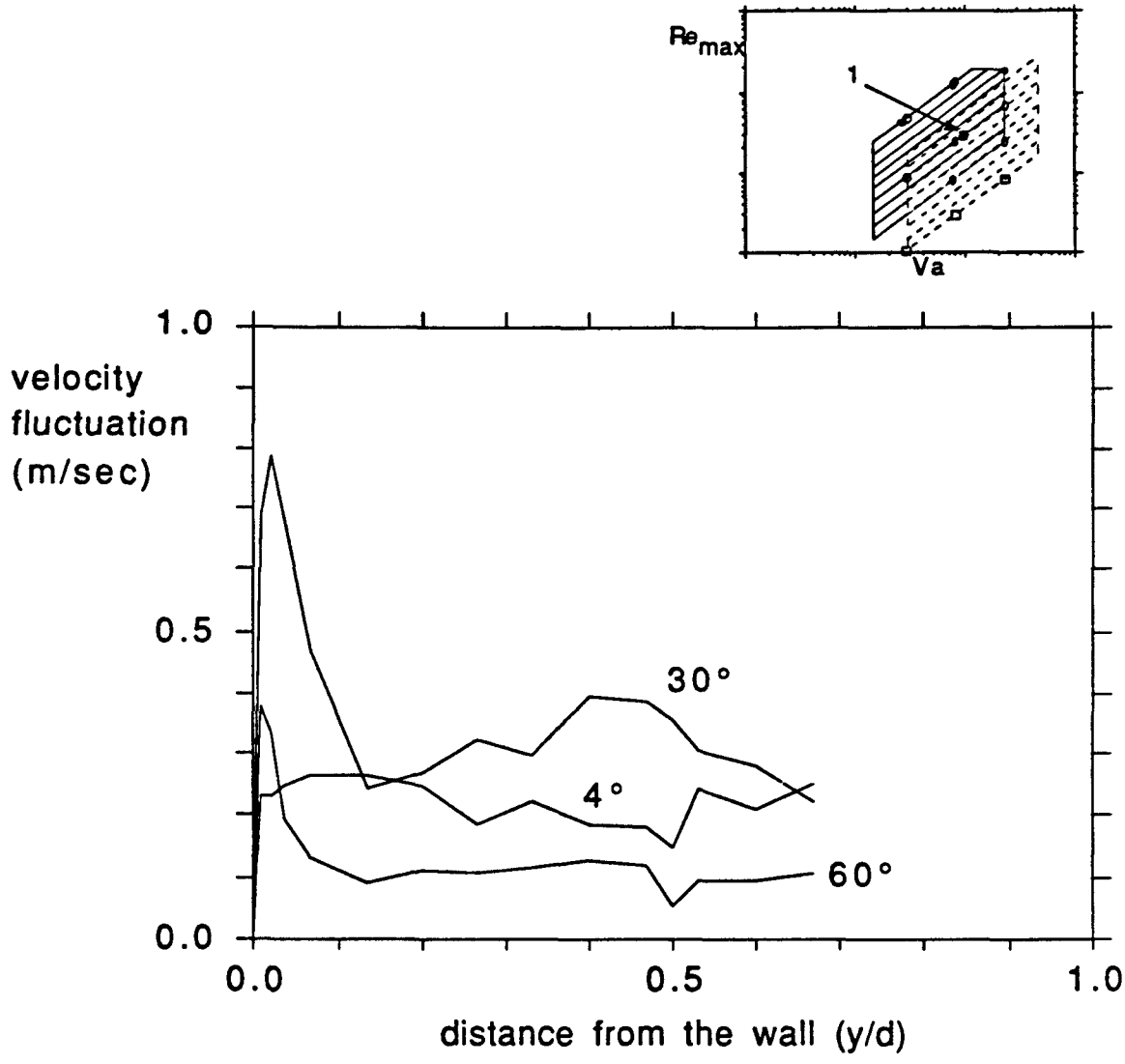

Figure 37: Profiles of velocity fluctuation near the open end, case 1, x/d = 58.3 of l/d = 60.

Figure 37 presents profiles of velocity fluctuation. At 4°, prior to transition, fluctuation levels are uniformly low. In the turbulent profile at 30°, fluctuations are higher, particularly near the wall. After the turbulent slug passes, fluctuation levels drop at all radial positions. Scaled on the ensemble-averaged velocity, fluctuations at 60° are very small. These measurements, and the argument presented, support the idea that increases in velocity fluctuations are accompanied by increased turbulent transport and that the observed decrease in fluctuation magnitude represents a decay of turbulent transport.

Figure 38 shows a trace of velocity fluctuation level measured further downstream (x/d = 8.33, near the drive). Again, the probe faces toward the open end of the test section. Therefore, only the first half-cycle is shown here. Fluctuation levels rise twice, the first around 31.5° and the second at 70°. The trace of ensemble-averaged velocity in Figure 39 shows that only the second, larger rise in fluctuation is accompanied by a rapid change in velocity. As expected, this rise in ensemble-averaged velocity is due to the change of profile shape between 68° and 70° (Figure 40). The increase in boundary layer thickness between 68° and 70° appears to be larger than the increase in boundary-layer thickness between 15° and 40°. Apparently the increase in fluctuation at 31.5° is not associated with as much of an increase in turbulent cross-stream transport of momentum as is the transition at 69°. Figure 41 shows that the profile of turbulent fluctuation level mirrors this two-step transition. Note that only the second step in fluctuation level is associated with increased free-stream turbulence intensity. This second rise in fluctuation level is consistent with calculations of convection of the turbulent slug which entered at flow reversal, i.e. the first transition was apparently not triggered by the incoming fluid.

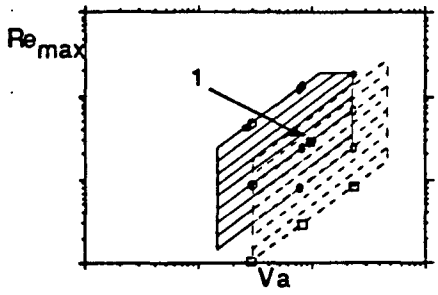

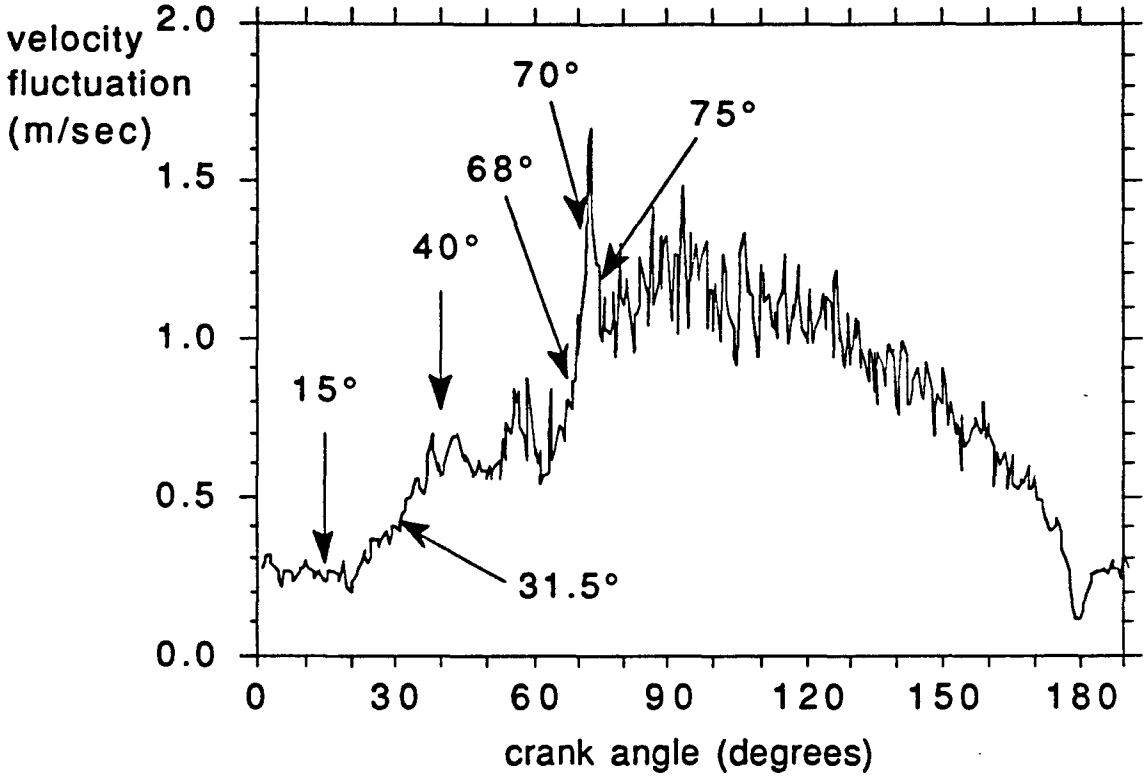

Figure 38: Trace of velocity fluctuation near the drive end, case 1, at r/R = 0.96, (y/d = 0.02) and x/d = 8.33 of l/d = 60 (far from the entry end).

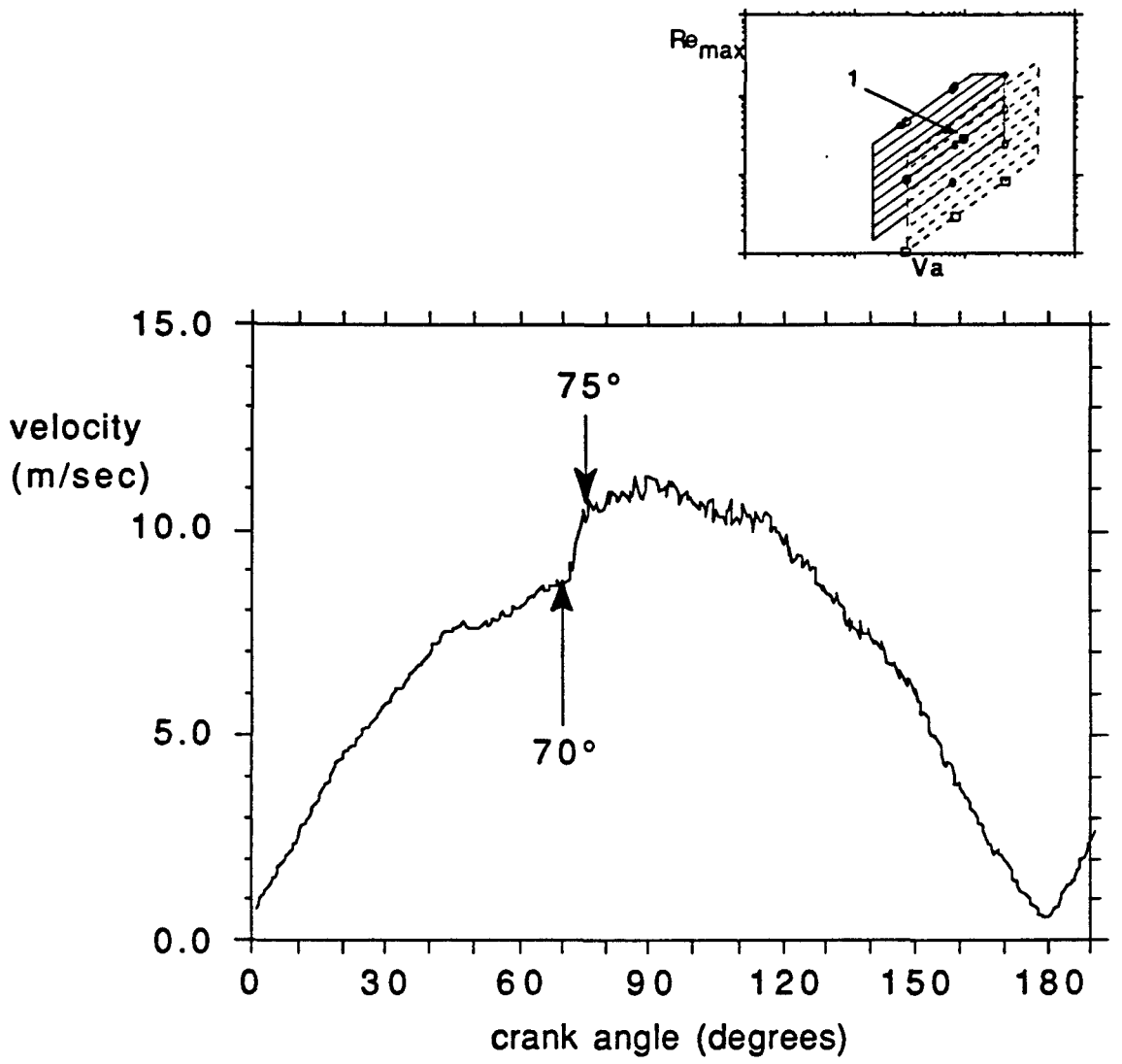

Figure 39: Ensemble-averaged velocity trace near the drive end case 1 x/d = 8.33, l/d = 60 r/R = 0.96, and y/d = 0.02.

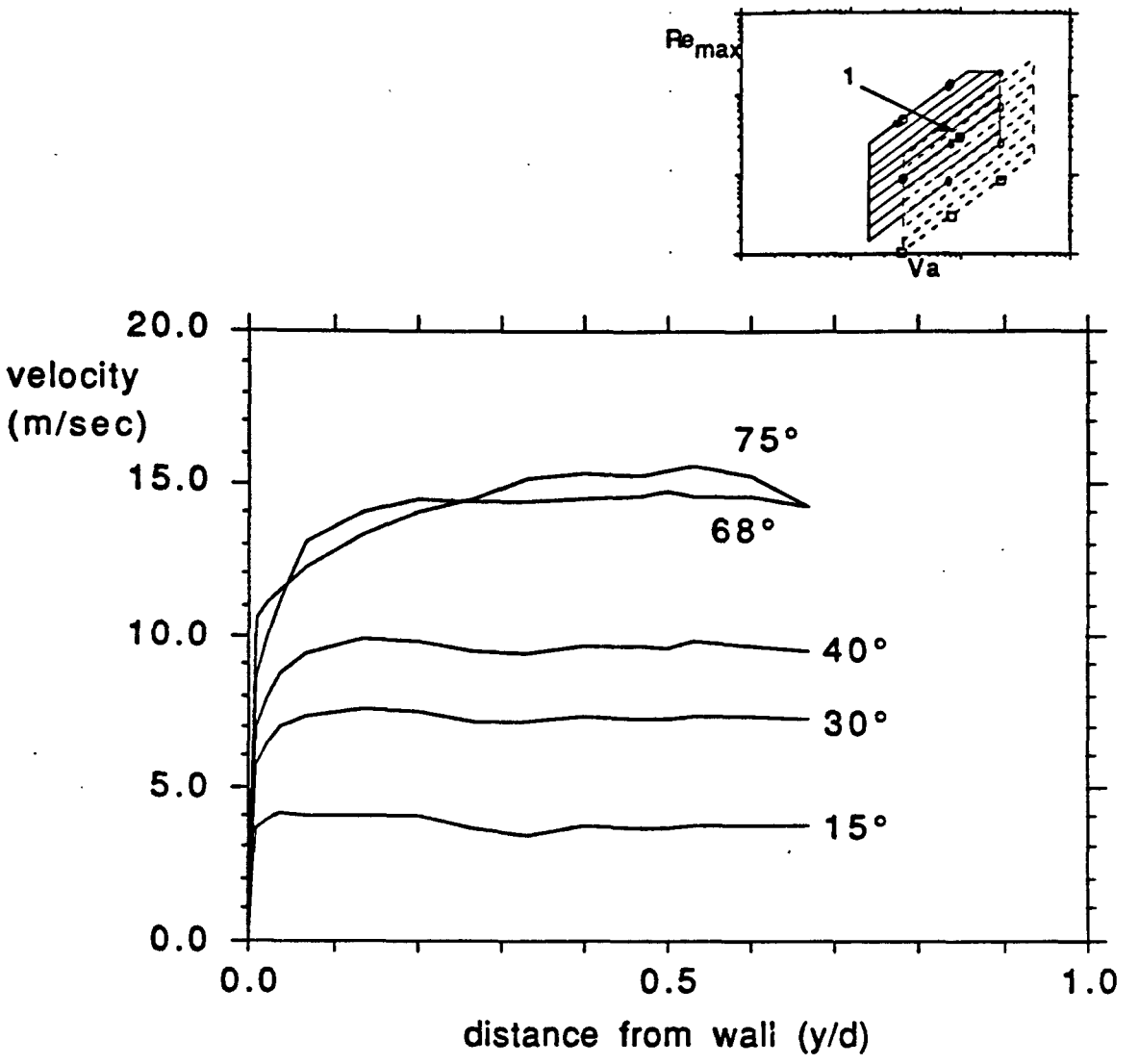

Figure 40: Velocity profiles near the drive end case 1 x/d = 8.33, l/d = 60.

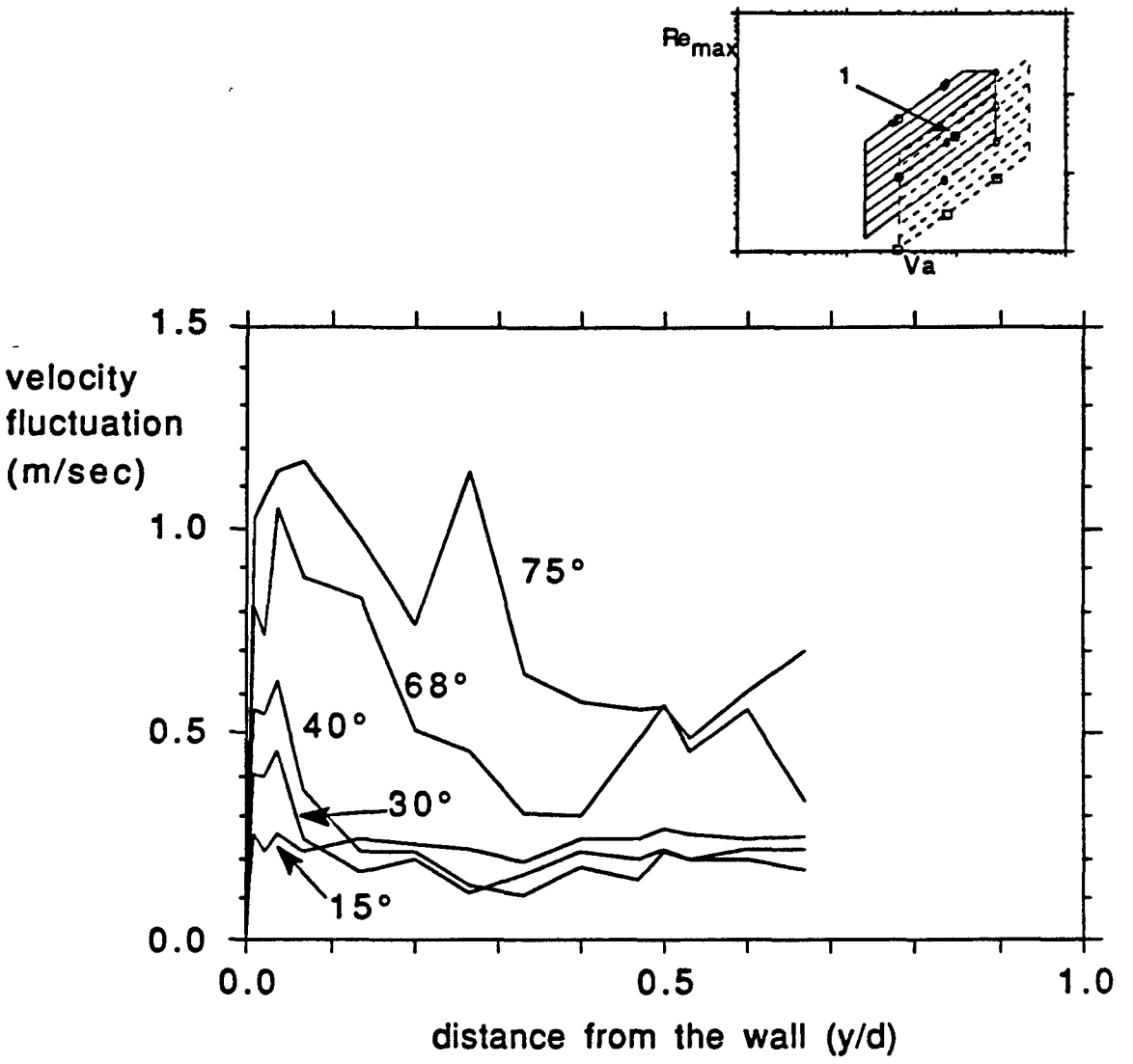

Figure 41: Profiles of velocity fluctuation near the drive end case 1 x/d = 8.33, l/d = 60.

3.2.8. Return to laminar flow

In this study, two cases were explored in which turbulent flow returned to laminar flow:

(1) after flow reversal

(2) after turbulent fluid had passed

The first kind is observed in virtually every trace of velocity fluctuation shown here. Laminar-like flow is observed during the early, high-acceleration portion of the

cycle. In contrast, in case e (Fig.24), there appears to be no decay to laminar flow, i.e. the entire cycle appears to be turbulent even though there is some variation in the magnitude of the fluctuation.

The second kind of relaminarization was discussed in case f above. Figure 25 shows that the flow becomes turbulent only as long as fluid with high turbulent kinetic energy is present at the probe position. Afterwards, the flow reverts to its laminar state. Apparently the flow is stable unless perturbed by advected turbulence. In Figure 31 transition to turbulence is first triggered by the turbulence convected in the fluid. After this fluid passes, the flow briefly reverts to the laminar state. Eventually the flow becomes turbulent again and remains turbulent throughout the remainder of the half-cycle.

In section 3.2.6, transition from laminar to turbulent flow was summarized by taking a Lagrangian viewpoint. Transition from turbulent to laminar flow in this oscillating flow may be summarized similarly:

- In the lower part of the operating map (cases n,o,p), the flow is always laminar.
- That fluid which was in the pipe at flow reversal, and all incoming low-turbulence fluid, remains laminar-like unless the wall boundary layers undergo transition due to boundary-layer growth and instability.

3.3. SPRE TEST RESULTS WITH A SMOOTH (NOZZLE) ENTRY

In this section, the results are presented for measurements taken in the test section with smooth (flow nozzle) inlet geometries (Fig. 3) at a specific operating point (see table 2) which most closely simulates the Space Power Research Engine (SPRE) heater tube operating point (Simon and Seume, 1988c). Detailed measurements taken at s/d = 0.33, 16, 30 and 44 are presented.

3.3.1. Transition Mechanisms

As detailed above, transition is initiated in one of two ways. The first mechanism involves the natural transition of an unstable boundary layer which has developed along the length of the test section. Transition arises in the second case from the tripping of an otherwise stable boundary layer by turbulence which has been convected downstream from the test section entrance. The latter mechanism is influenced by both the geometry of the inlet, which guides the flow into the test section, and the effect of flow oscillation on the

production and decay of the convected turbulence. It should be noted that there are cases of "transition" in which a stable laminar boundary layer is disturbed by the convected free-stream turbulence and becomes turbulent-like but returns to a laminar-like state after the high-turbulence slug passes. The flow neither trips to sustained turbulent flow nor relaminarizes but rather is a stable, laminar boundary layer flow that is temporarily disturbed by the convected turbulence. In order to fully understand the transition process and the nature of convected turbulence in oscillating flow, it is best to focus first on the data acquired near the test section entrance. This data set is labelled the "boundary condition" because it serves to provide the entry (boundary) profiles of velocity and turbulence quantities to those who wish to numerically simulate the flow.

3.3.2. Results at s/d = 0.33 (Boundary Condition)

The analysis of results begins at s/d = 0.33, immediately downstream of the flow nozzle (see Fig. 3). This is a natural place to begin the discussion because the flow at this station is very early in its development (spatially) and because downstream flow conditions are strongly influenced by the inlet geometry. In this section, some of the basic characteristics of oscillating flow are briefly introduced, including (1) the response of the flow to a temporally-varying pressure gradient, (2) the formation of eddies in the nozzle inlets to the test section, and (3) the anisotropy of the flow. In addition, a discussion of how the "wall coordinates" analysis is applied to the data to compute wall skin friction coefficients is given here since it is the first station presented in this section.

Response of Flow to Pressure Gradient

A dominant characteristic of oscillating flow is the temporally-varying pressure gradient. Figure 42 is a plot of profiles of ensemble-averaged velocity versus y position for every 30° of crank position for the first half of the cycle of the SPRE case. The core flow is very flat throughout this half of the cycle. Only in the region below y/R = 0.133 is the effect of the wall seen, indicating the edge of the developing boundary layer. Figure 43 is a plot of ensemble-averaged velocity versus crank position for the first half of the cycle, during which air is drawn into the test section from the room. The centerline velocity (r/R = 0) closely approximates a sinusoid, as expected from the smooth sinusoidal piston motion. Near the wall (r/R = 0.968), the fluid is of lower momentum than that of the core flow and thus responds more readily to the pressure gradient. The near-wall fluid leads the

core by approximately 5° in accelerating from rest, and it passes through zero velocity at 170°, nearly 10° prior to the core flow. Note also that during the accelerating phase of the flow, the near-wall fluid does not exhibit a smooth sinusoidal acceleration. This variation is influenced by the pressure gradient and turbulent fluid ingested from the nozzle immediately upstream, as will be described below.

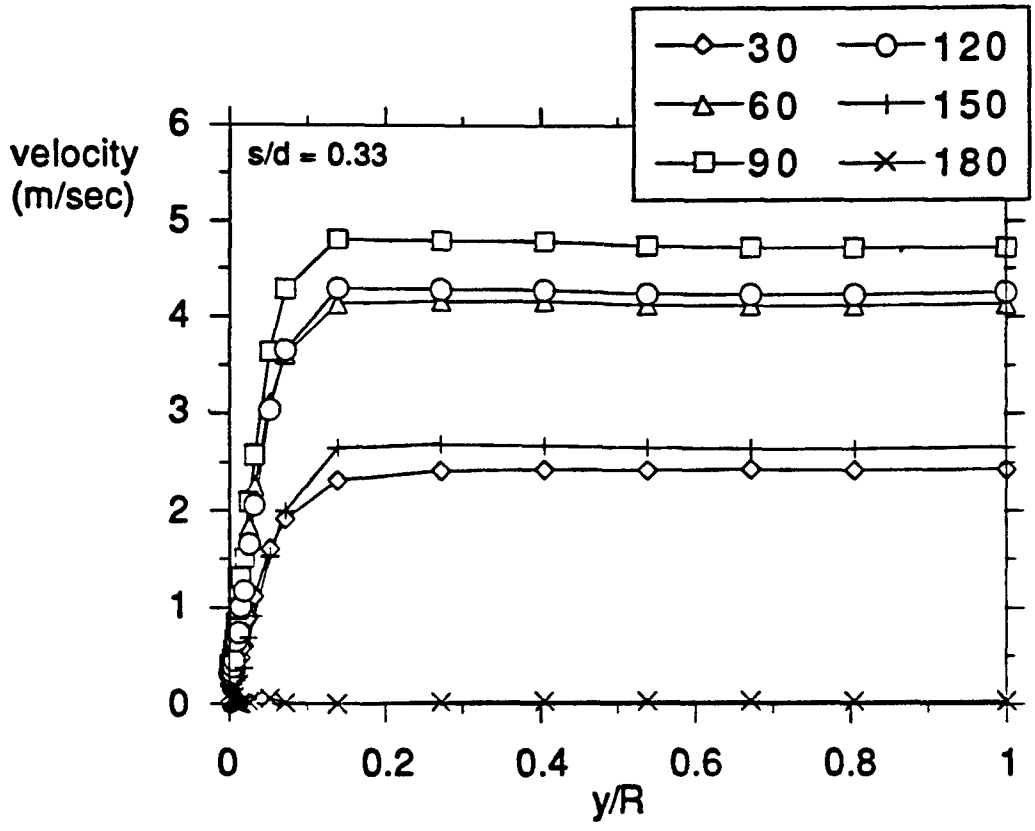

Figure 42: Profiles of ensemble-averaged velocity at s/d = 0.33.

Eddy Formation in Flow Nozzle

Essential to a complete picture of the fluid mechanics in the test section is the documentation of the influence of inlet geometry. In this experimental program, smooth nozzles were used to avoid flow separation upon inflow to the test section. The nozzles do not, however, avoid separation upon outflow, and thus, large scale eddy-like structures are generated in the nozzle as the test section is exhausted during the second half of the cycle (Fig. 44). At flow reversal, the axial-mean flow is momentarily stationary, but the flow is

not stagnant. Eddies formed during the second half cycle do not dissipate completely. As the flow accelerates at the start of the next cycle, the eddies are strained through the nozzle

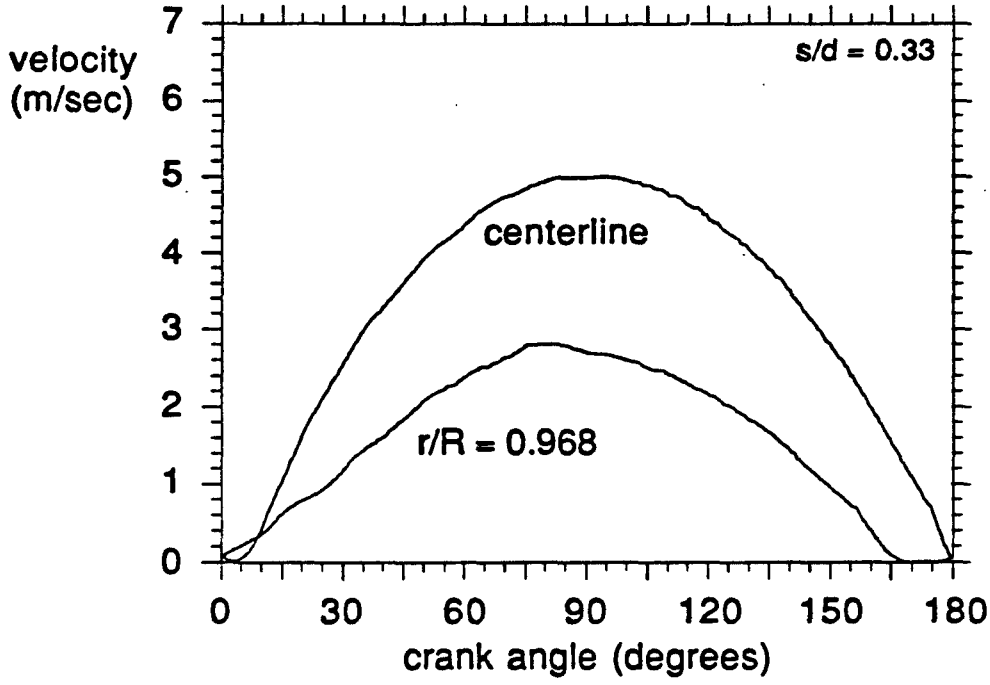

Figure 43: Centerline and near-wall ensemble-averaged velocity at s/d = 0.33.

and are convected down the test section, followed by the fluid which resided in and upstream of the heat exchanger core at flow reversal (see geometry in Figs. 3 and 44). As discussed above, the heat exchanger cores are comprised of narrow passages which break up large-scale fluid motion into smaller scales which can dissipate quickly. Hence, upon flow reversal, a slug with large eddy structures is convected downstream every cycle, followed by fluid of lower turbulent kinetic energy which is contained in the small turbulence scales and is, thus, dissipating rapidly.

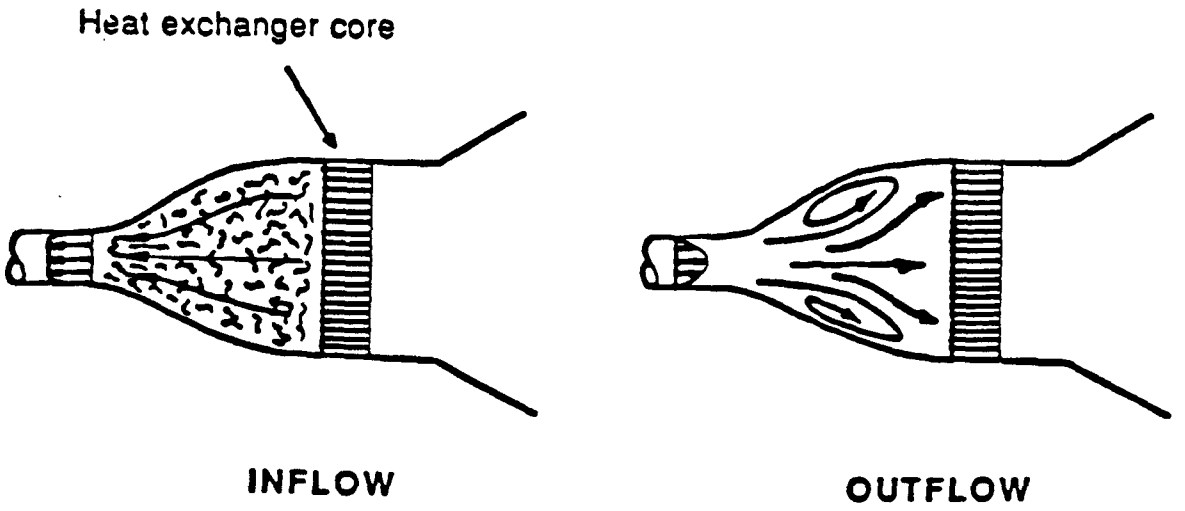

Figure 44: Eddy formation in flow nozzles.

Advection of Eddy Structures

Figure 45, a plot of a near-wall (r/R = 0.968) and centerline trace of the rms fluctuation of the axial component of velocity at s/d = 0.33, illustrates the effect of the slug, which washes past this measurement station between approximately 20° and 100° of crank position. Elevated fluctuation levels appear first at the centerline, almost immediately after flow reversal, suggesting that the leading edge of the slug turbulence is in the core. In the near-wall region, the fluctuations during passage of the slug are quite high, and the trailing edge of the slug is well defined, denoted by the steep decline in rms fluctuation beyond 75° and followed by a region of quiet flow which persists throughout the remaining half-cycle. Figure 46 is a plot of the normalized turbulence intensity, the ratio of rms fluctuation to ensemble-averaged velocity, $u' / \tilde{u}$, generated from the data of Figures 43 and 45. Note that the near-wall data are offset by 0.1 for ease of viewing and the measurements below 15° and above 165° have been omitted (since the turbulence intensity rises to infinity as the ensemble-averaged velocity approaches zero at flow reversal.).

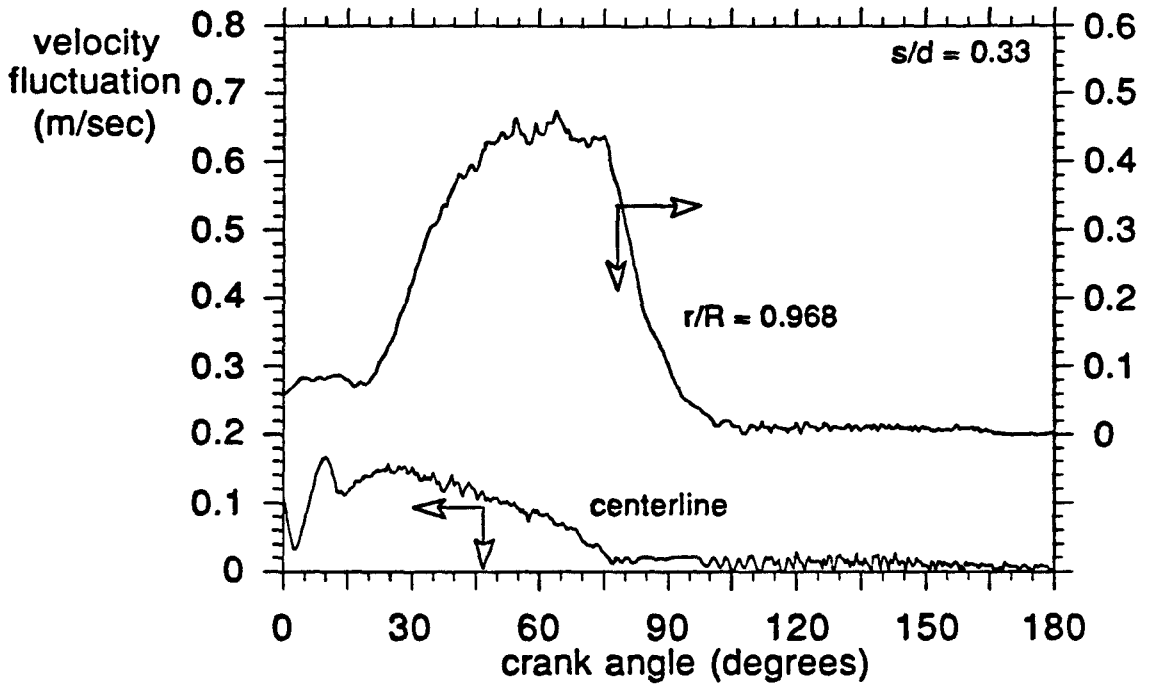

Figure 45: Centerline and near-wall velocity fluctuation at s/d = 0.33.

A comparison of Figures 45 and 46 illuminates the stabilizing effect of acceleration, which reduces the turbulence intensity across the duct. The normalized turbulence intensity during passage of the slug (Fig. 46) ranges from between 25% and 17% in the near-wall region to less than 1% in the core flow. This suggests that the large scale eddies convected from the nozzle are concentrated in the near-wall region. The flow in the center of the tube, after passage of the turbulent slug is fluid that has been reduced to small-scale turbulence in the heat exchanger passages, strained in the nozzle and allowed to decay in the short entry section of the tube upstream of the probe.

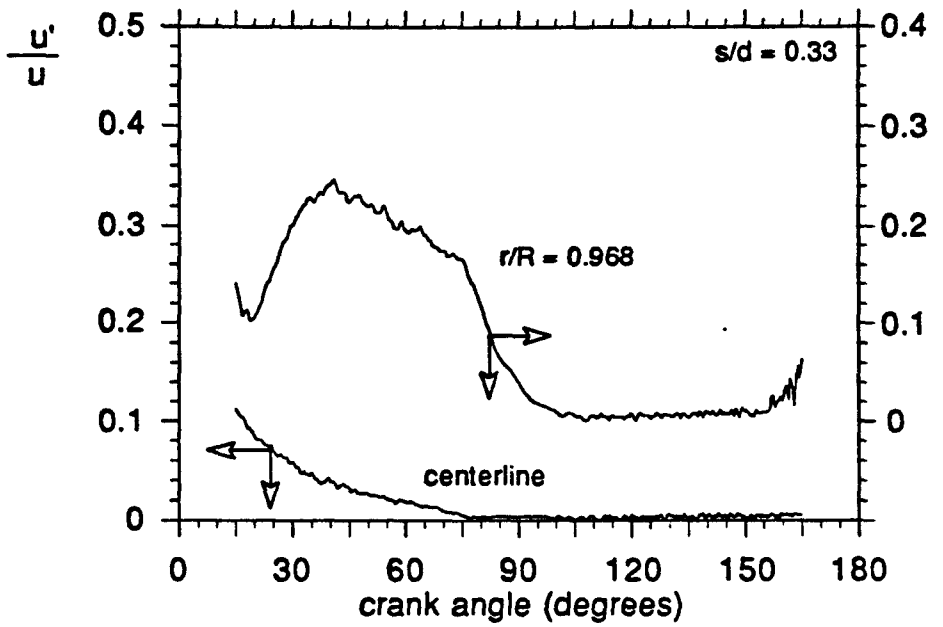

Figure 46: Centerline and near-wall turbulence intensity at s/d = 0.33.

Flow Anisotropy

Measurements with the cross-wire probe of axial and radial components of rms-velocity fluctuation give insight into the degree of anisotropy of the turbulence in the flow, an important boundary condition to computer modelling of the flow. At r/R = 0.733, the radial and axial fluctuations are comparable (Fig. 47), following nearly the same trace with crank angle. Note that the cross-wire data were ensemble averaged over 150 cycles and are not as completely converged as are the single-wire data.

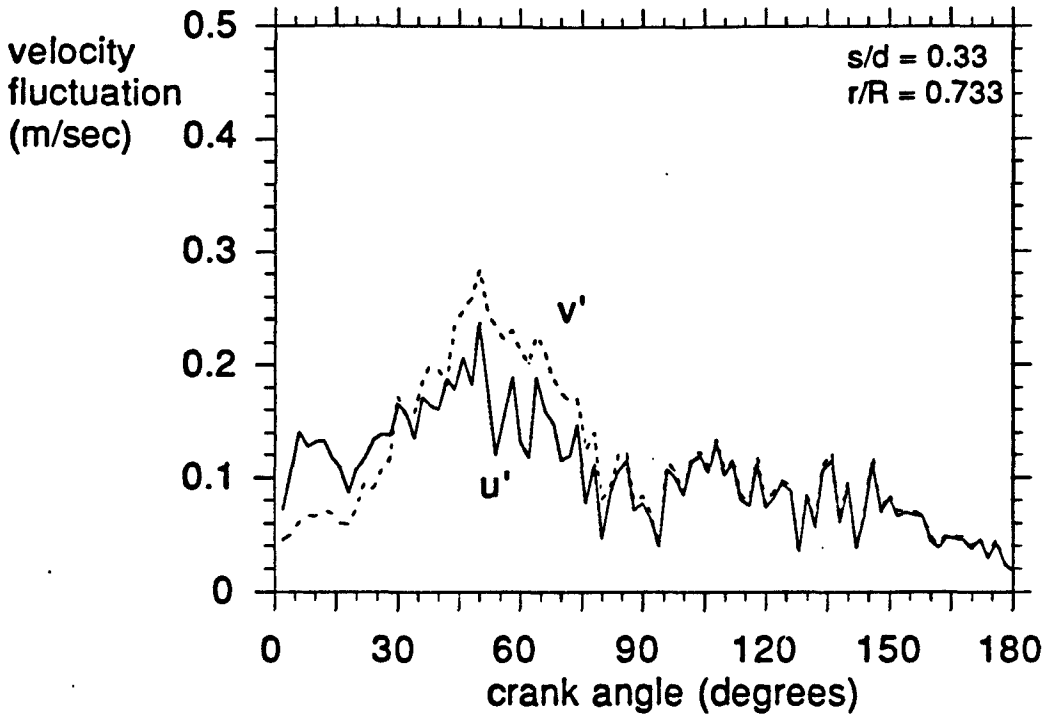

Figure 47: Near-wall streamwise and radial fluctuation at s/d = 0.33.

Wall dampening is considered to be the mechanism that restrains v' values to near-u' values. In the core flow, at the pipe centerline (Fig. 48), the radial component of velocity fluctuation in the convected slug, v', is high relative to the streamwise component, u', reflecting the straining action in the nozzle and the lack of dampening by the presence of a wall (in Fig. 47). This is in agreement with the general understanding that larger scale eddies associated with the core flow are more anisotropic than the smaller-scale eddies near the wall. The high centerline values around the 60° cycle position in Fig. 48 may be a result of fluctuating asymmetry of compression experienced by the large-scale eddies as they are compressed through the nozzle. Note that the peak value of the 3D turbulence intensity, estimated to be $\{(u'^2 + 2v'^2)/3\}^{0.5} / \bar{u}$, is approximately 8% at the centerline and 7% at r/R = 0.733.

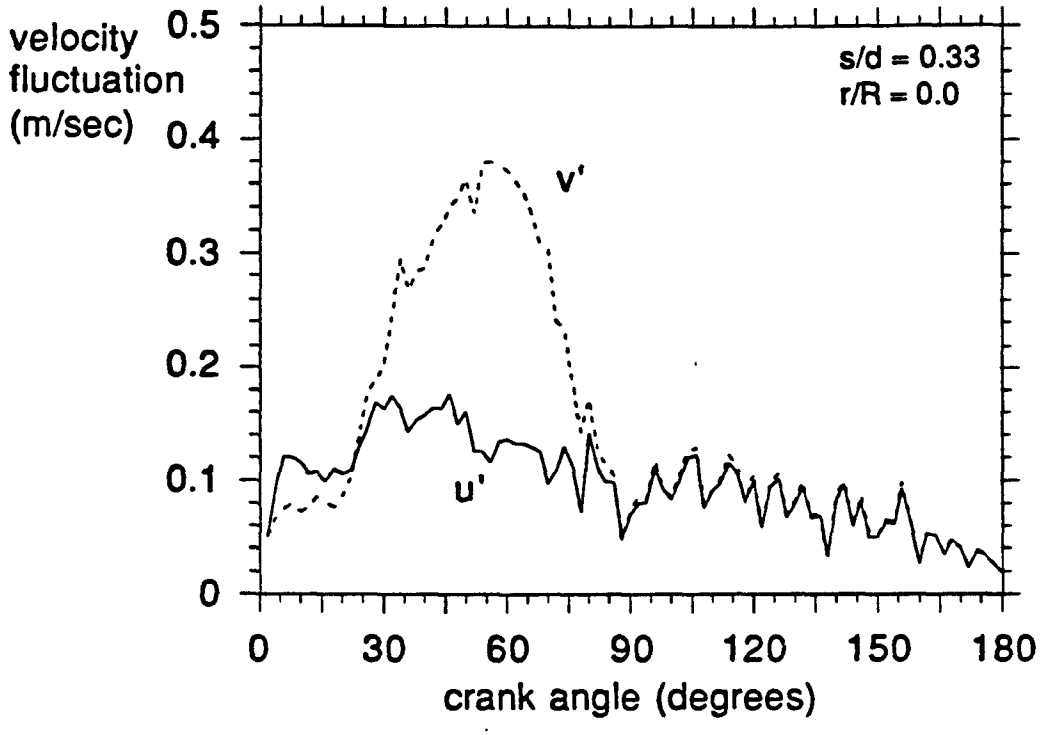

Figure 48: Centerline streamwise and radial fluctuation at s/d = 0.33.

Figure 49 is a three-dimensional plot of the Reynolds shear stress, $-\overline{u'v'}$, versus the crank position and non-dimensionalized radius. This component of Reynolds stress, a measure of the degree to which the radial and axial components of turbulence correlate, helps in assessing both the level of turbulent transport and whether or not transition has occurred. Note that the data of Fig. 49 were smoothed to aid in the qualitative assessment of the turbulence (see Volume 2 for an unsmoothed version of Figure 49). The smoothing consisted of averaging a data point with the two nearest cross-wire measurements, one point 2° earlier and the other 2° later in the cycle. To avoid averaging errors in regions of abrupt change in shear stress, as occurs at transition (see Figure 68 at s/d = 30, for instance), data within ±4° of the abrupt change were not averaged. Also note that in Figure 49, the darkened plane at r/R = 0.0 is the centerline. The 3D surface extends to r/R = 0.8. Since r/R = 0.8 is the near-wall limit of reliable data, the wall, at r/R = 1, does not appear in the figure.

Although the passage of the slug is clearly evident in Figs. 47 and 48, the contour of Fig. 49 appears relatively flat throughout the cycle, suggesting that the turbulent

transport within the slug is weak. The shear stress, averaged over radius r, and crank position, θ, between 30° and 70°, during passage of the slug, is 0.0103 m^2/sec^2. In comparison, between 72° and 150°, the average is 0.0082 m^2/sec^2, or 80% of the former. The slug is a passing disturbance which temporarily elevates the level of rms-velocity fluctuation without significantly increasing the cross-stream momentum transport.

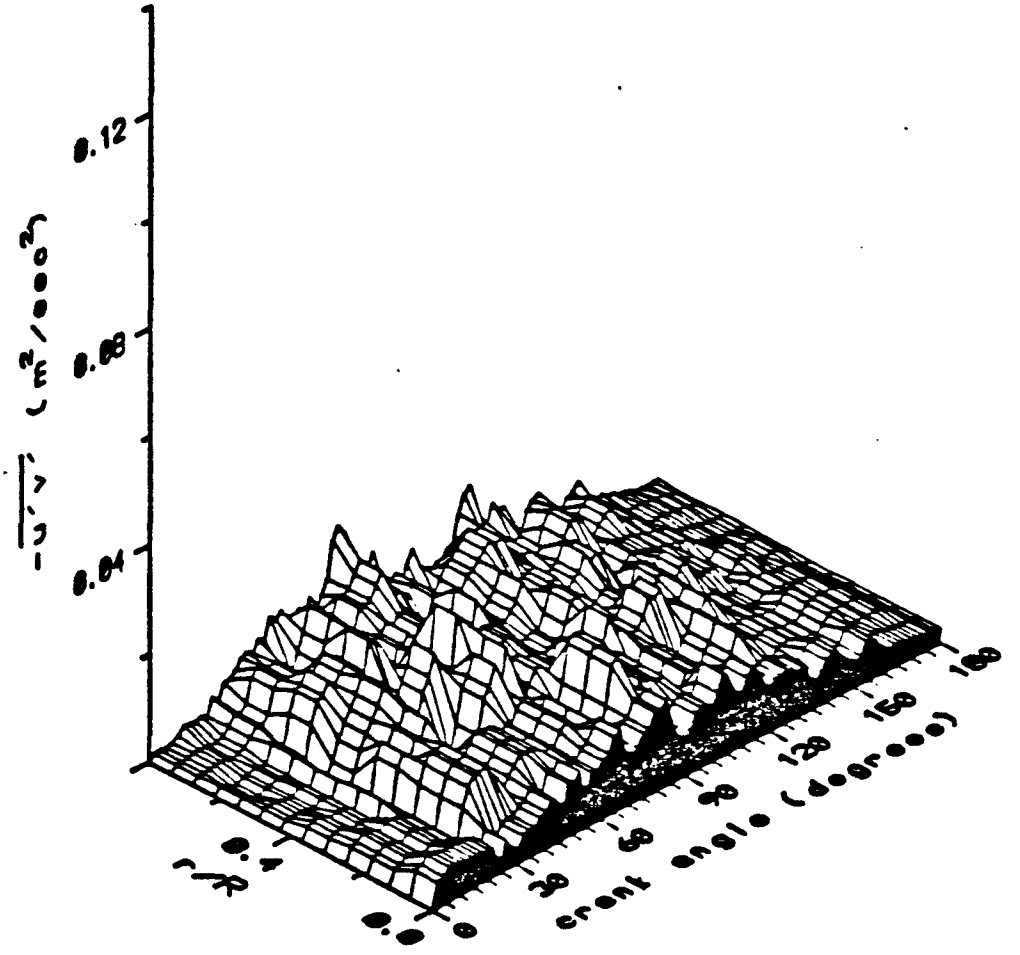

Figure 49: 3D view of Reynolds shear stress at s/d = 0.33 (smoothed)

Processing in "Wall Coordinates"

To further characterize the flow, the data are converted into u^+ - y^+ coordinates by iterating on the friction velocity using the offset in y position, as discussed above in Sec. 2.5. Figure 50 depicts the full profile of sixteen radially distributed boundary condition (s/d = 0.33) experimental data points at 120°. This position is early in the decelerating phase of the first half-cycle. Also shown is a curve representing the Couette flow model

described in Sec. 2.5 for the laminar flow regime. Figures 45 and 46 clearly illustrate that once the turbulent slug has passed this measurement station ($\theta > 100°$), the flow appears laminar-like until flow reversal at 180°. The laminar model fits very well out to $y^+ = 10$, beyond which the Couette flow assumption used to develop the flow model breaks down. It should be noted that at 120°, the effect of the pressure gradient on the model is small, and, as a result, the model differs little from the $u^+ = y^+$ relationship characteristic of the viscous sublayer of a flat-wall boundary layer.

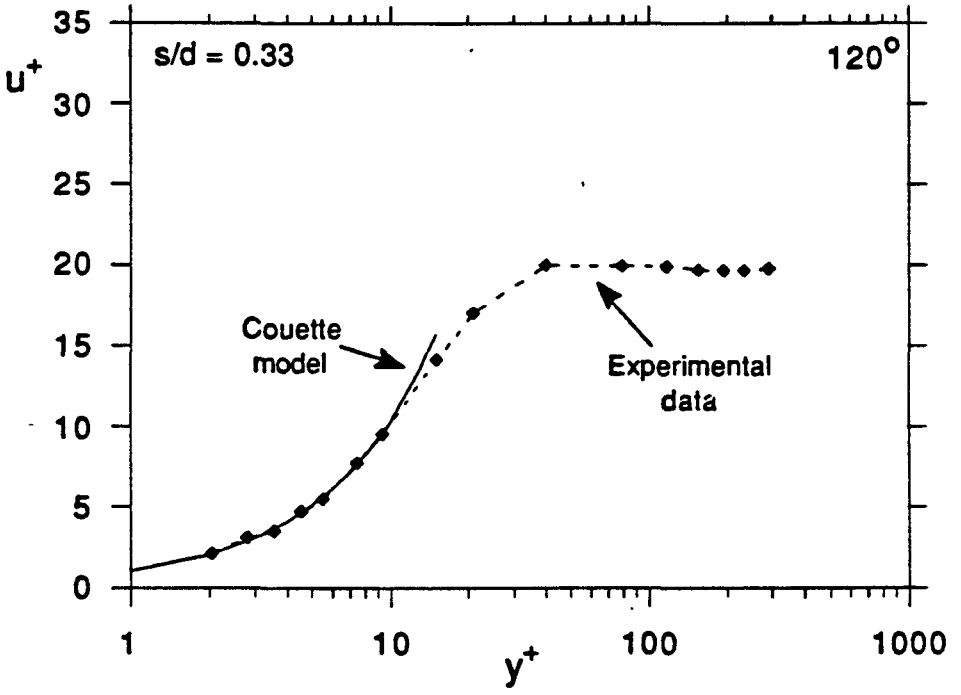

Figure 50: Velocity profile in wall coordinates at 120° for s/d = 0.33.

Once the processing is complete, u_* is known and the relationship between skin-friction coefficient, $c_f = 2u_*^2 / u_m^2$, and crank position can be plotted, as in Figure 51 for the boundary condition data (s/d = 0.33). Note that u^+ - y^+ and skin friction results are tabulated in Volume 2 for both the experimental data and the data generated from the Couette flow model. Although the flow was assumed to be turbulent between 30° and 60°, by virtue of the passage of the turbulent slug, the flow does not undergo transition. With the understanding that the slug's effect on turbulent transport is very small (see Fig. 49), it is not surprising that the skin friction coefficient is relatively unaffected. Note that prior to 30° and after 60° in the cycle, the laminar boundary layer model was invoked. During

acceleration, the bulk-mean velocity increases at a faster rate than the friction velocity, resulting in a decreasing dimensionless skin friction coefficient through 60°. Beyond 90°, the bulk-mean velocity and friction velocity decrease in tandem, and a nearly constant coefficient persists through 150°. As the flow approaches reversal, the coefficient increases rapidly since the bulk-mean velocity drops to zero much more quickly than does u_*.

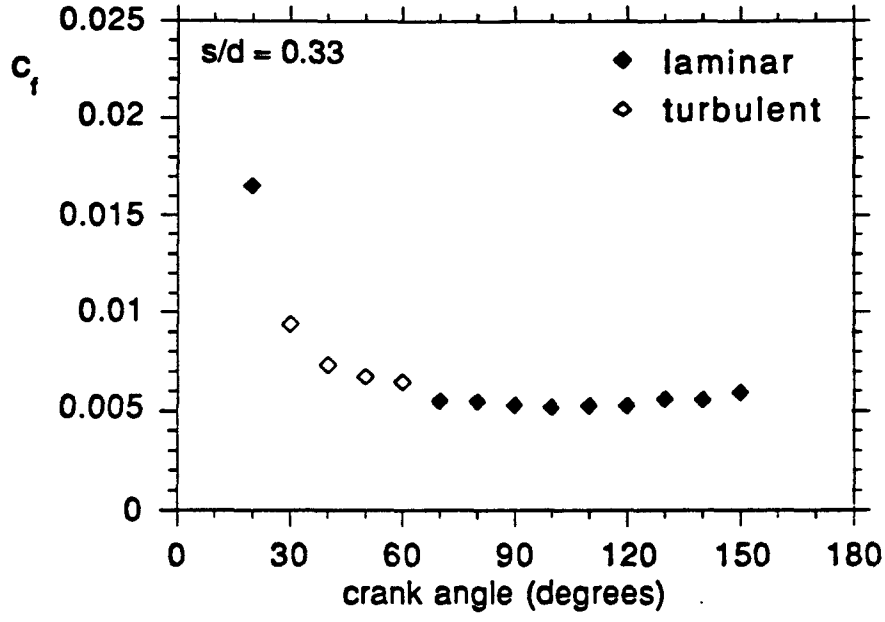

Figure 51: Skin friction coefficient at s/d = 0.33.

3.3.3. Results at s/d = 16

The response of the flow to the pressure gradient is evident at this station, for which the near-wall flow (r/R = 0.959) sees a minimum at 162.5° (Fig. 52). Further into the core, at r/R = 0.872, the flow reverses at 176.5°, while the centerline flow lags reversal of the near-wall flow by nearly 6°.

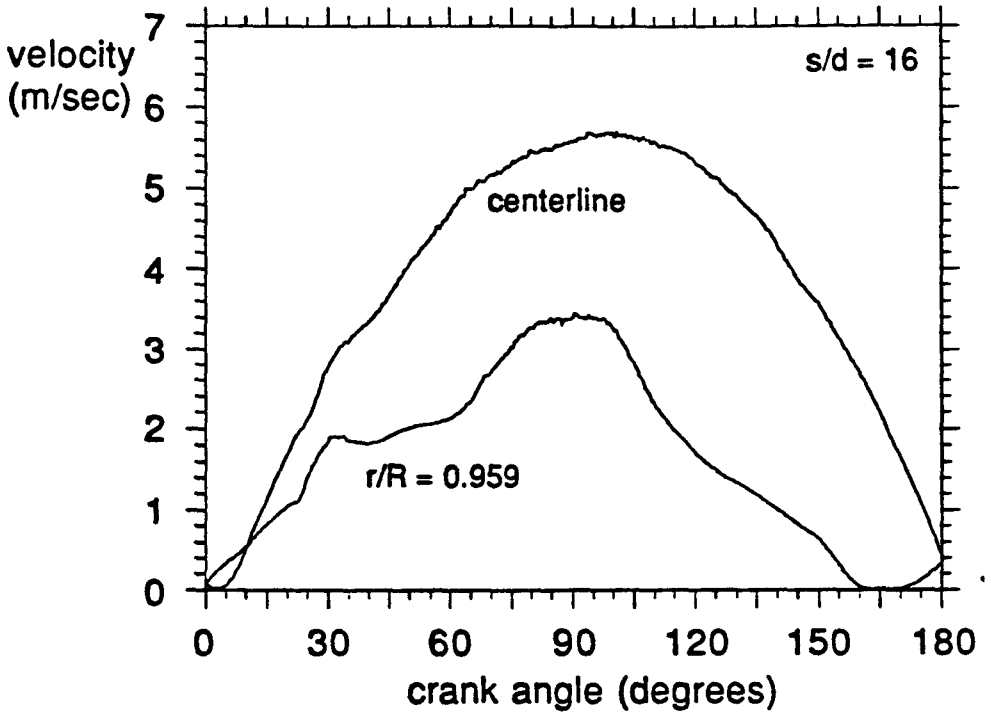

Figure 52: Centerline and near-wall ensemble-averaged velocity at s/d = 16.

Figure 53 is a three-dimensional plot of the streamwise component of rms-velocity fluctuation versus radial position and position within the cycle for s/d = 16. Note that the darkened surface is the centerline, at r/R = 0.0. Advected turbulence, which first is seen near 57°, raises the core fluctuation levels, bringing up the saddle point region between the core and the wall. But, once the slug has passed at approximately 105°, as predicted from an analysis of the convection of the slug, the fluctuations drop off markedly. The flow does not undergo transition, but rather responds to this passing disturbance.

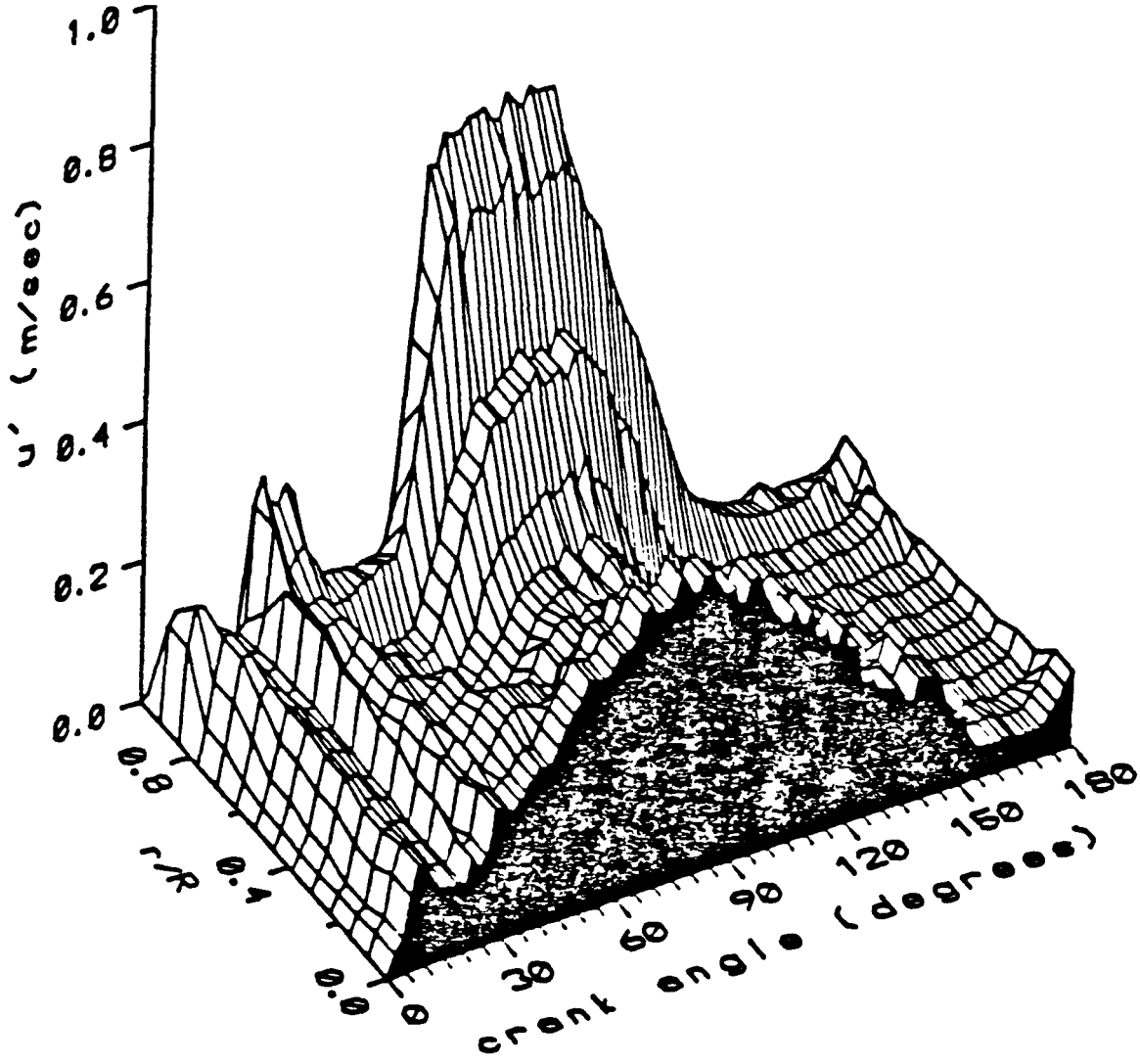

Figure 53: 3D view of streamwise velocity fluctuation at s/d = 16.

Deceleration tends to destabilize the near-wall flow, as illustrated in the profiles of ensemble-averaged velocity in Figure 54, thereby thickening the boundary layer as the cycle progresses toward reversal at 180°. Note that during passage of the slug, the profile at 90° is rounded, indicating a high level of cross-stream transport. This is different than the effect observed at the s/d = 0.33 station. It seems that the boundary layer is more receptive to vorticity amplification at this point of the cycle, but not to the point of passing through sustained transition. Once the disturbance has passed, the weakened cross-stream

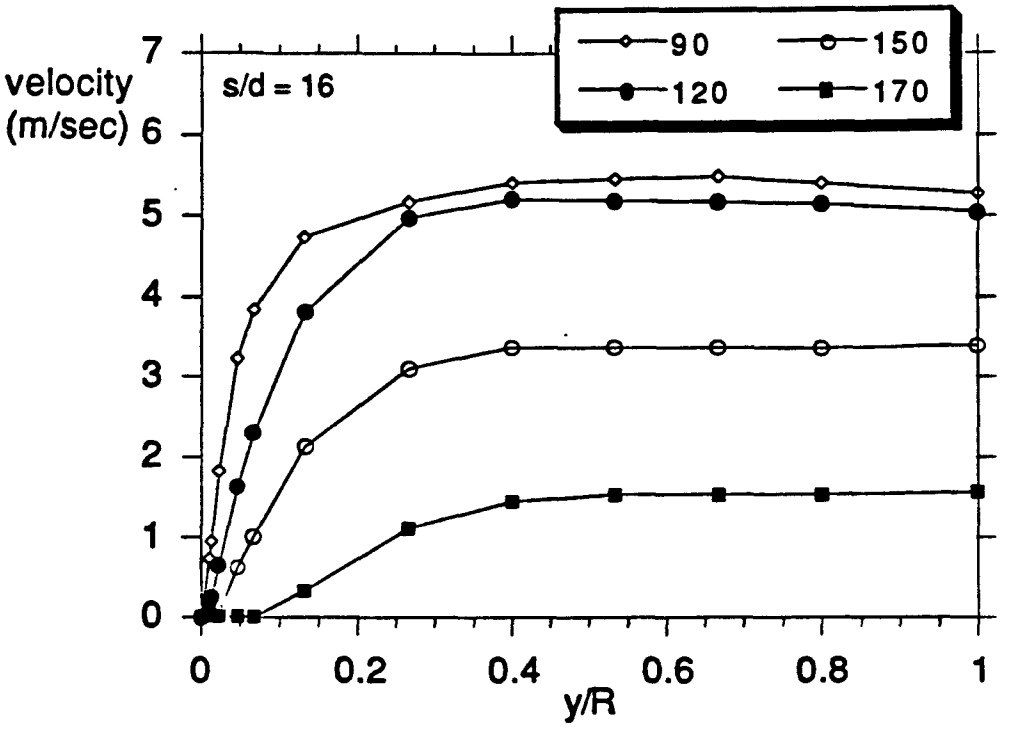

Figure 54: Profiles of ensemble-averaged velocity at s/d = 16.

transport translates into flatter profiles. The presence of cross-stream transport is confirmed by Figure 55, a three-dimensional plot of the Reynolds shear stress, $-\overline{u'v'}$, at s/d = 16. Unlike in Figure 49, for the less well-developed boundary layer at s/d = 0.33, the boundary layer has grown along the pipe length and turbulent activity in the slug has been enhanced markedly. The maximum shear stress at s/d = 16 is 0.1043 m^2/sec^2, which occurs at 92°, for r/R = 0.800, during passage of the slug. This compares to a maximum of 0.0327 m^2/sec^2 at 64°, for r/R = 0.467 at s/d = 0.33. Note that Figure 55 is smoothed, as discussed in section 3.3.2. for s/d = 0.33.

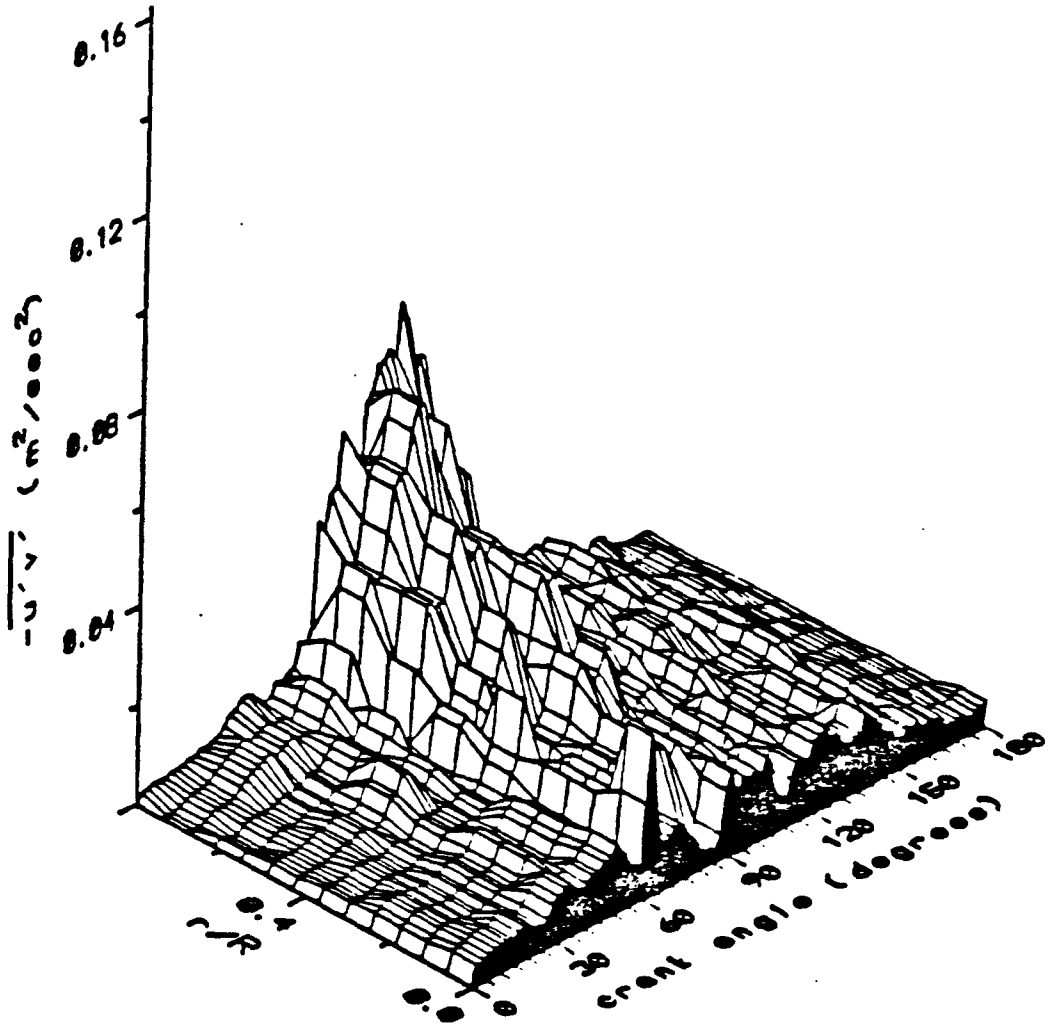

Figure 55: 3D view of Reynolds shear stress at s/d = 16 (smoothed)

In characterizing the anisotropy of the turbulence, it is useful to compare the axial and radial components of rms-velocity fluctuation. Figures 56 and 57 depict u' and v' traces at s/d = 16 for a near-wall station, r/R = 0.733, and for the centerline, respectively.

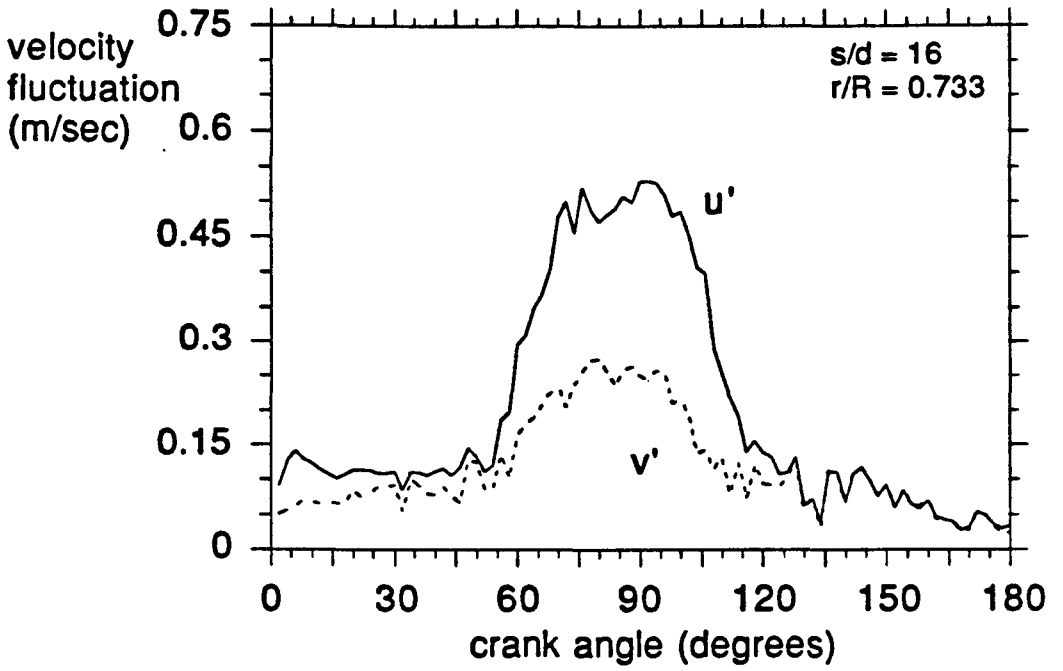

Figure 56: Near-wall streamwise and radial fluctuation at r/R = 0.733 for s/d = 16

As documented in Table 7 of tabulated ratios of the two velocity fluctuation components at selected positions within the cycle at s/d = 16, the core flow is nearly isotropic throughout the cycle. Near the wall, the flow is strongly affected by the slug. The axial velocity component is nearly double the radial velocity component during passage of the slug, suggesting that the former is perhaps amplified in the boundary layer while the latter is strongly damped by the wall. After the turbulence has passed, the flow reassumes a nearly isotropic state.

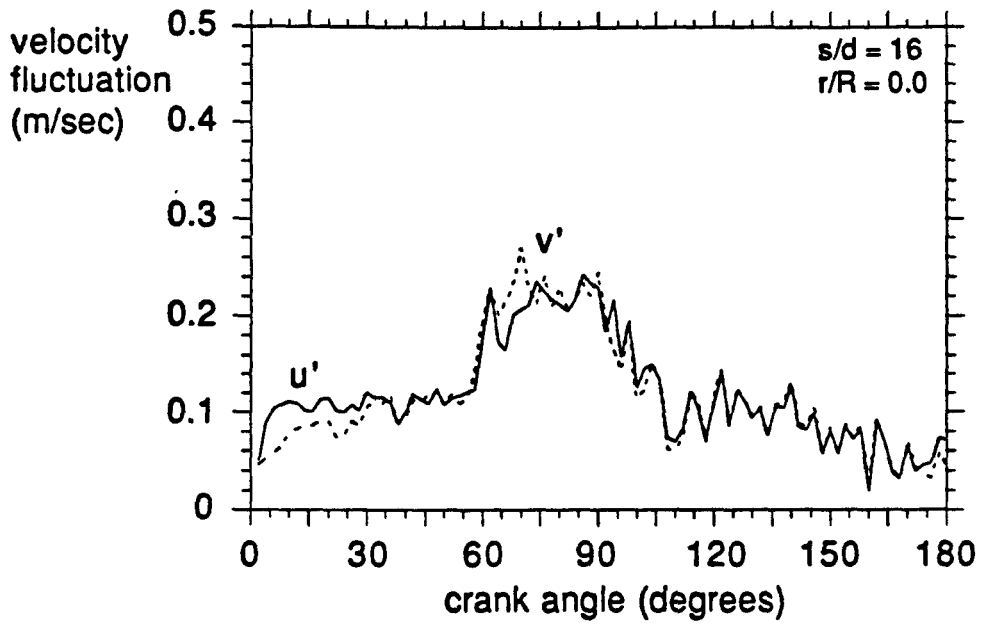

Figure 57 Centerline streamwise and radial fluctuation at s/d = 16.

	r/R = 0.733 (near-wall)	r/R = 0 (centerline)
crank angle (°)	u' / v'	u' / v'
28	1.25	1.03
58	1.91	0.87
88	1.90	1.06
120	1.47	0.93
148	1.02	1.00

Table 7: Ratios of axial to radial components of rms-velocity fluctuation at s/d = 16.

Figure 58 depicts the relationship between the skin friction coefficient and the crank position within the cycle for s/d = 16. Prior to the arrival of the turbulent slug near 60°, the skin friction drops dramatically. The friction velocity grows by 43% between 20° and 60°, but the bulk-mean velocity, on which it is normalized, increases by 168%. During passage of the slug, the turbulent-like flow sees a 60% increase in skin friction to a peak at 90°, in keeping with the enhanced turbulent transport seen in Figure 55, followed by a decline

through the laminar-like portion which follows and persists through flow reversal. After the slug has passed, the skin friction resumes what appears to be a continuation of the path it assumed prior to the slug's arrival. Skin friction values beyond 150° are not plotted since the bulk-mean velocity tends toward zero and the skin friction coefficient increases without bound.

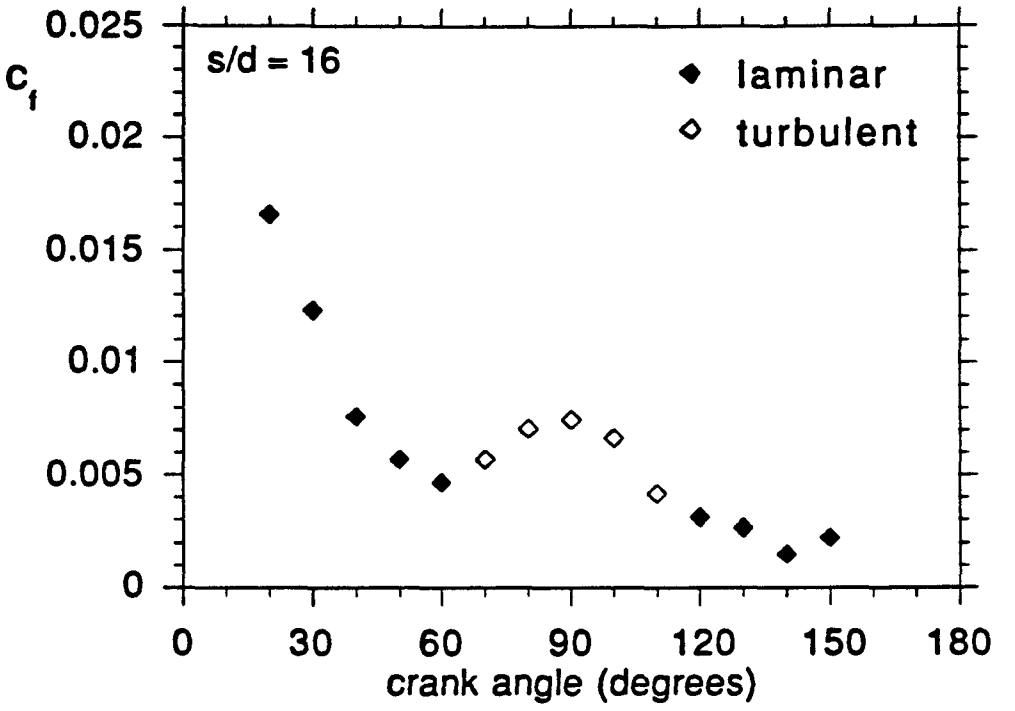

Figure 58: Skin friction coefficient at s/d = 16.

At 90°, the pressure gradient is momentarily zero. Figure 59 plots the experimental data for this position in the cycle at s/d = 16 against the turbulent flow model. The curve reduces to the flat-plate model since p^+ is instantaneously zero ($A^+ = 25$, the base case value from Eqn. 16 in Sec. 2.5.2.). The data follow the model for $y^+ < 20$, beyond which the data exceed the model values. This is either due to a violation of the Couette flow assumption or a residual effect on the profile of the past acceleration history. In Figure 60, at 120°, the flow has experienced 30° of adverse pressure gradient and agrees with the model (corrected with the instantaneous p^+) only out to $y^+ = 10$.

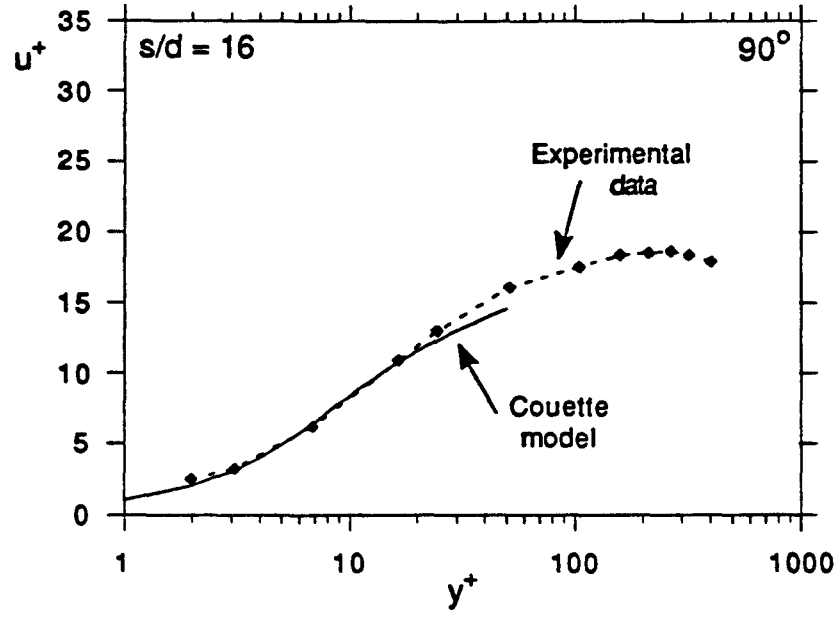

Figure 59: Velocity profile in wall coordinates at 90° for s/d = 16.

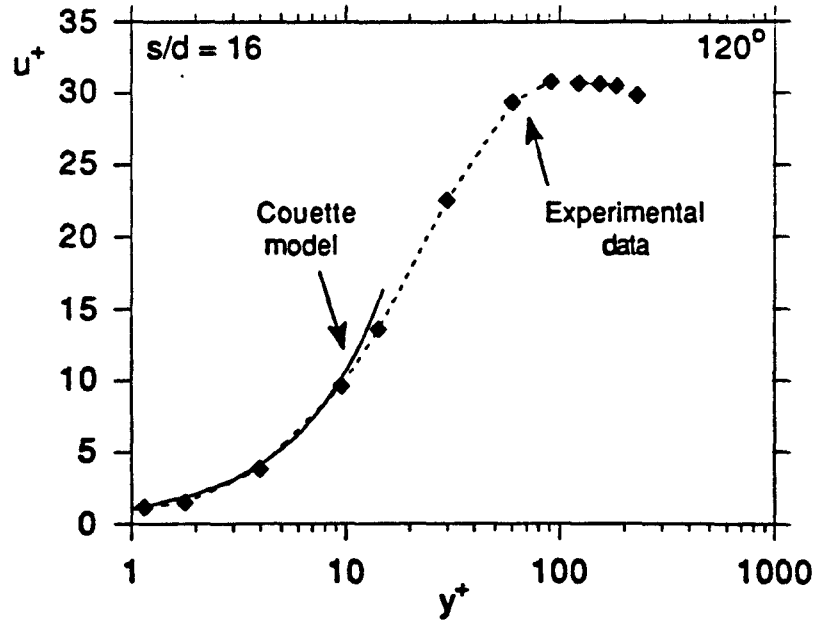

Figure 60: Velocity profile in wall coordinates at 120° for s/d = 16.

3.3.4. Results at s/d = 30

Figure 61 is a three-dimensional plot of ensemble averaged velocity versus radial position and position within the cycle for s/d = 30. The darkened surface represents the measurements at r/R = 0.997, closest to the wall. During acceleration, the profiles remain flat while the boundary layer grows from the wall into the core flow. Transition occurs

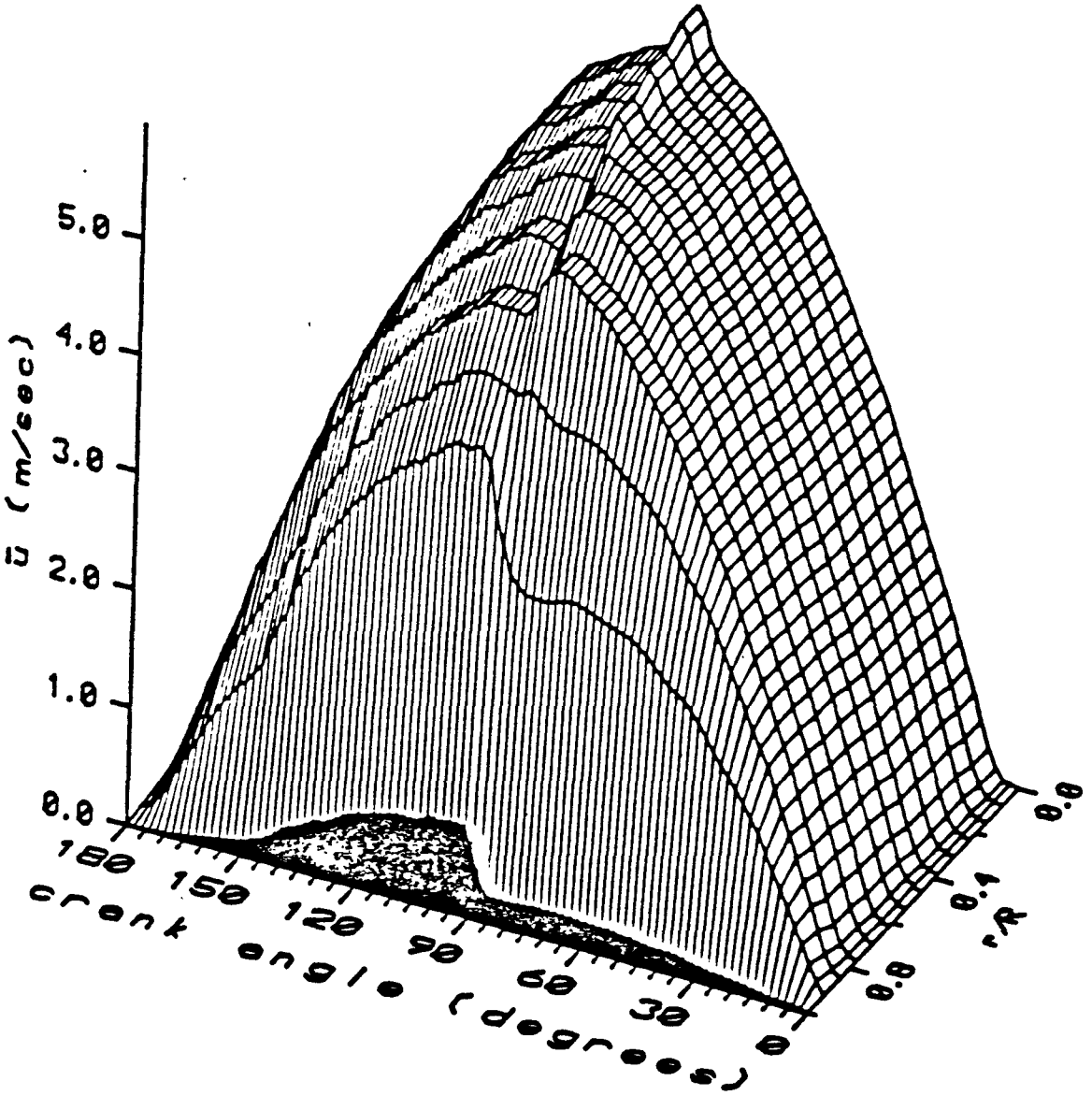

Figure 61: 3D view of ensemble-averaged velocity at s/d = 30.

nearly instantaneously across the tube cross-section at a crank angle of approximately 87°, which coincides with an estimate for the time of arrival of the high-turbulence slug convected from the nozzle region at the bulk velocity. The abruptness of transition is seen in the centerline flow, which experiences a slight rise after transition as the profiles become more rounded due to enhanced cross-stream momentum transport from the wall. The low-momentum, near-wall fluid responds more readily to the adverse pressure gradient than does the core flow, passing through zero earlier in the cycle.

The violent tripping to transition is illustrated for a near-wall (r/R = 0.970) trace in Figure 62. Transition is more abrupt than at upstream stations due to a higher instability of the boundary layer, which has grown longer into the cycle, (since thirty diameters of advection occurs before the slug arrives at the axial station).

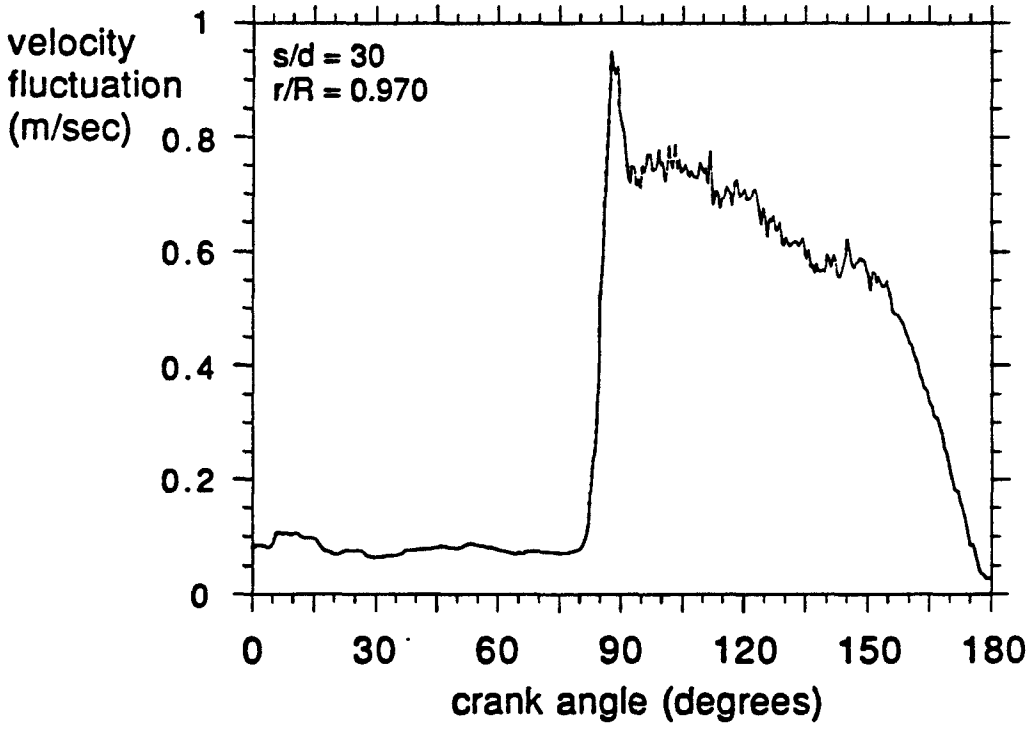

Figure 62: Near-wall streamwise velocity fluctuation at r/R = 0.970 for s/d = 30.

The acceleration phase has a strong stabilizing effect on the core-flow turbulence, as evidenced by the decay in the level of rms-velocity fluctuation in Figure 63 for which the black surface is the centerline. The near-wall flow shows the growth, in time within the

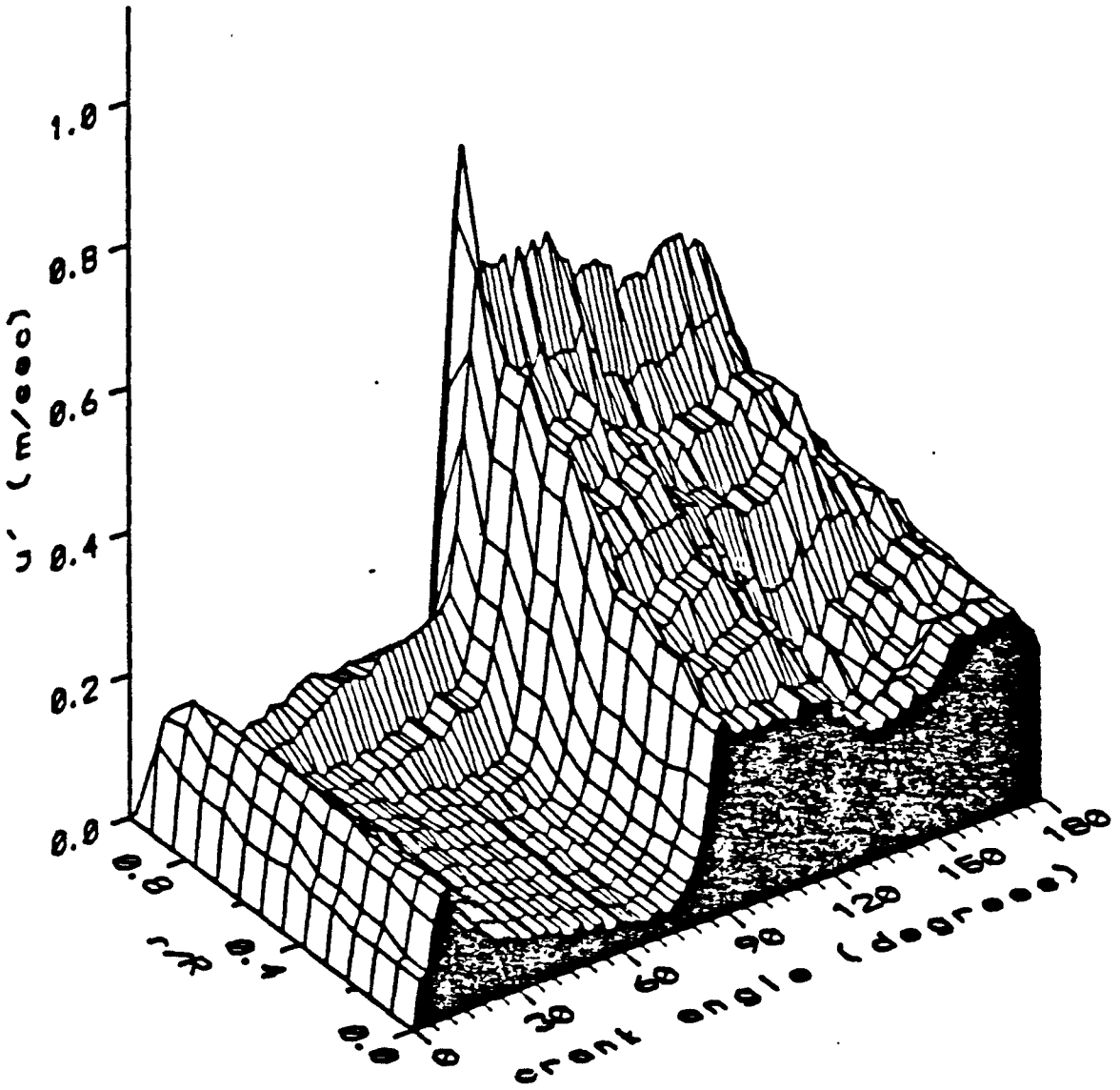

Figure 63: 3D view of streamwise velocity fluctuation at s/d = 30 (centerline view).

cycle, of a laminar boundary layer. As the boundary layer grows, it becomes less stable and allows the near-wall convected turbulence to be amplified, hence the rising fluctuation levels. This is also visible in Figure 64, the same surface as that of Fig. 63, but viewed from the near-wall side. Production of turbulence at the wall proceeds in spite of the

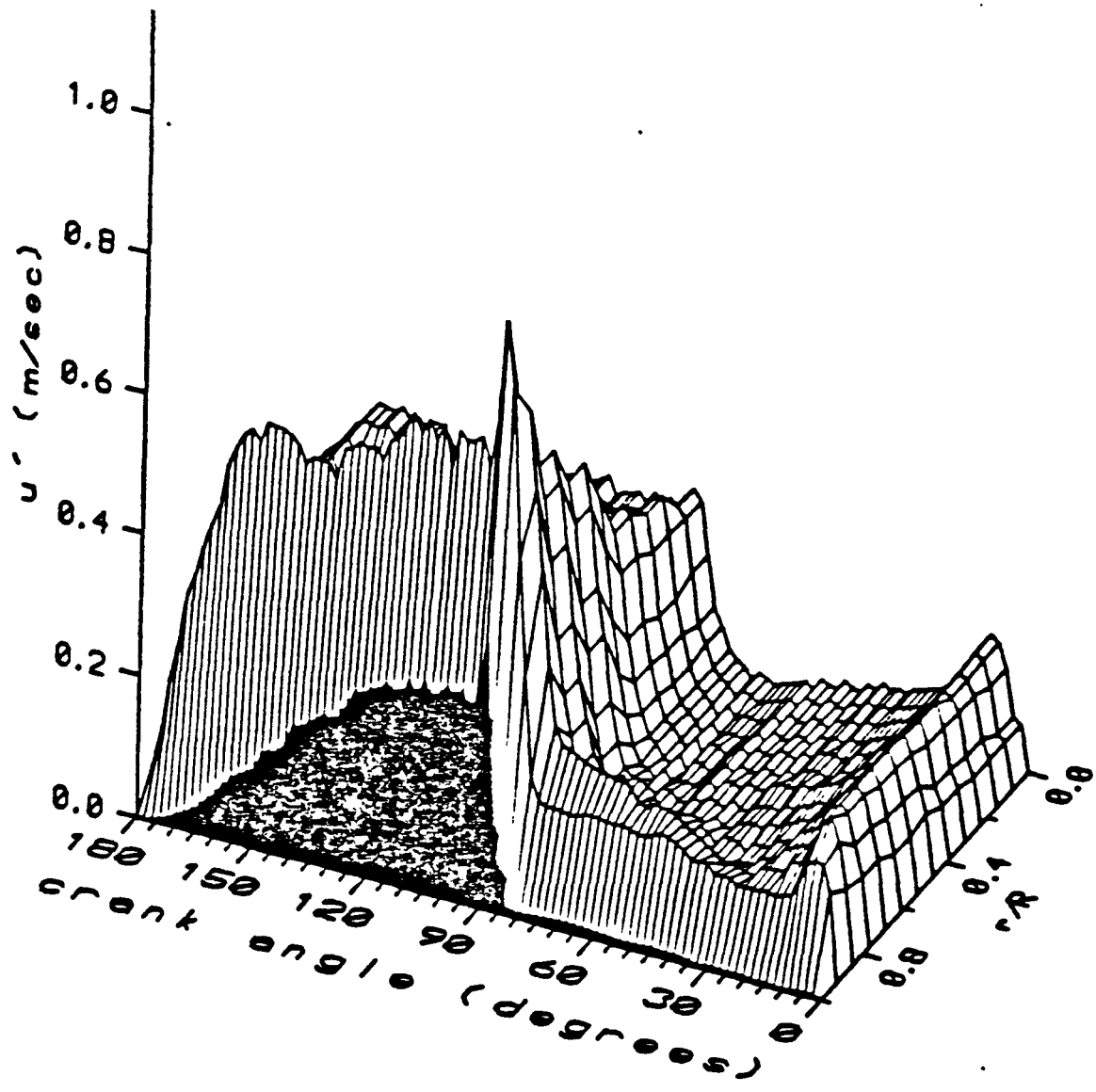

Figure 64: 3D view of streamwise velocity fluctuation at s/d = 30 (near-wall view).

stabilizing effect of the imposed favorable pressure gradient. Figures 63 and 64 show a growth in fluctuation level in the outer portion of the boundary layer. Figure 64 illustrates that the peak in rms-velocity fluctuation shifts toward the wall after approximately 80°. The maximum fluctuation is 0.874 m/sec, which occurs at 88° for r/R = 0.970. Figure 65 is a plot of rms-velocity fluctuation (Figs. 63 and 64) normalized on the ensemble-averaged local streamwise velocity. The high turbulence intensity in the near-wall region increases the turbulence level in the outer portions of the boundary layer by virtue of the enhanced cross-stream momentum transport.

For evaluation of skin friction, the data were processed through 90° using the laminar flow model. At 60°, the data fit the model very well within the viscous sublayer

(Fig. 66). The abrupt boundary-layer transition at this axial position has a strong effect on the skin friction coefficient, which increases by 174% between 80° and 90°, as is evident in Figure 67. Figure 68, a three-dimensional plot of Reynolds shear stress viewed from the centerline, clearly demonstrates that there is an abrupt increase in turbulent transport, focused in the near-wall region, at the assumed crank position of transition. The maximum shear stress, 0.1464 m^2/sec^2, occurs at 88° for r/R = 0.8. The average shear stress for the flow at s/d = 30 prior to transition is 0.0062 m^2/sec^2, compared with 0.0383 m^2/sec^2 for the remainder of the cycle.

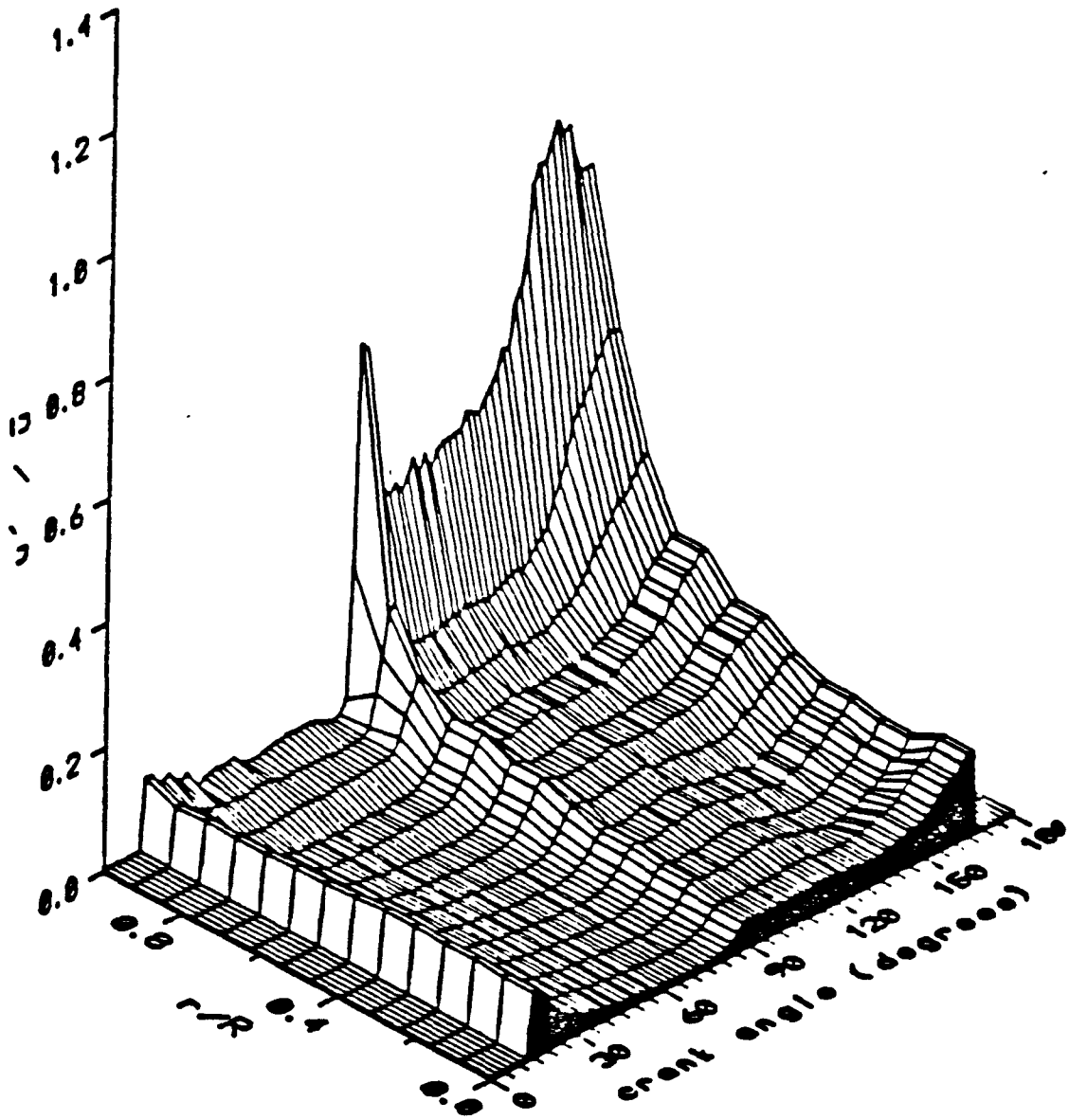

Figure 65: 3D view of streamwise turbulence intensity at s/d = 30.

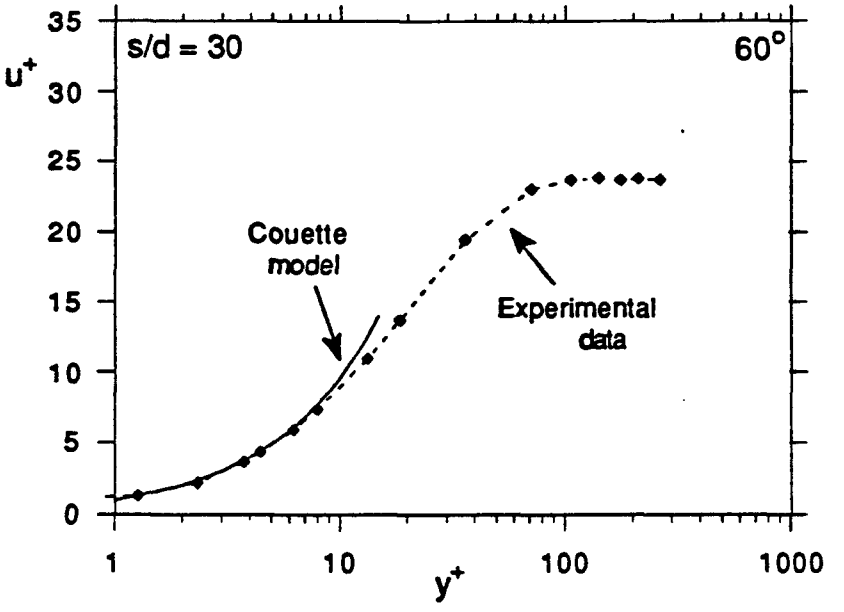

Figure 66: Velocity profile in wall coordinates at 60° for s/d = 30.

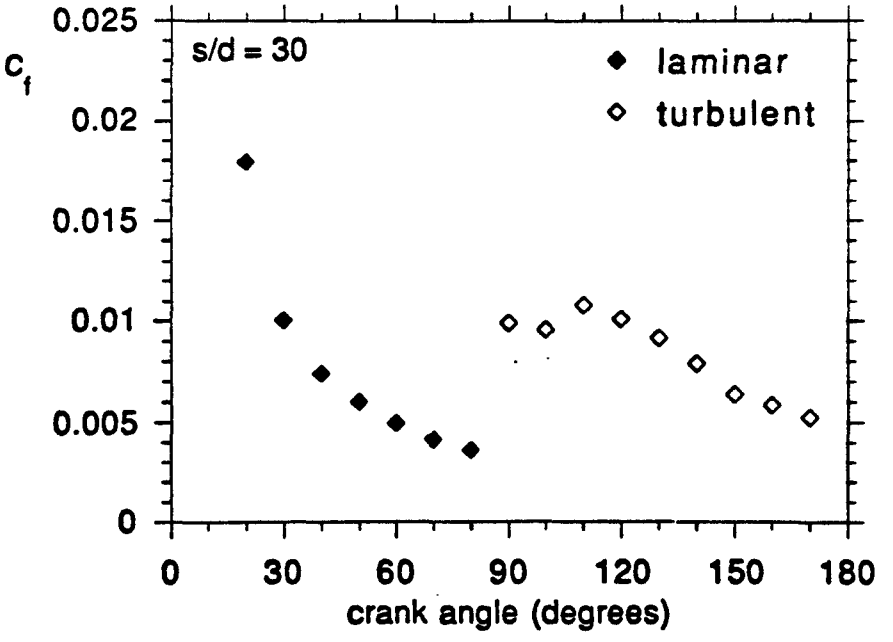

Figure 67: Skin friction coefficient at s/d = 30.

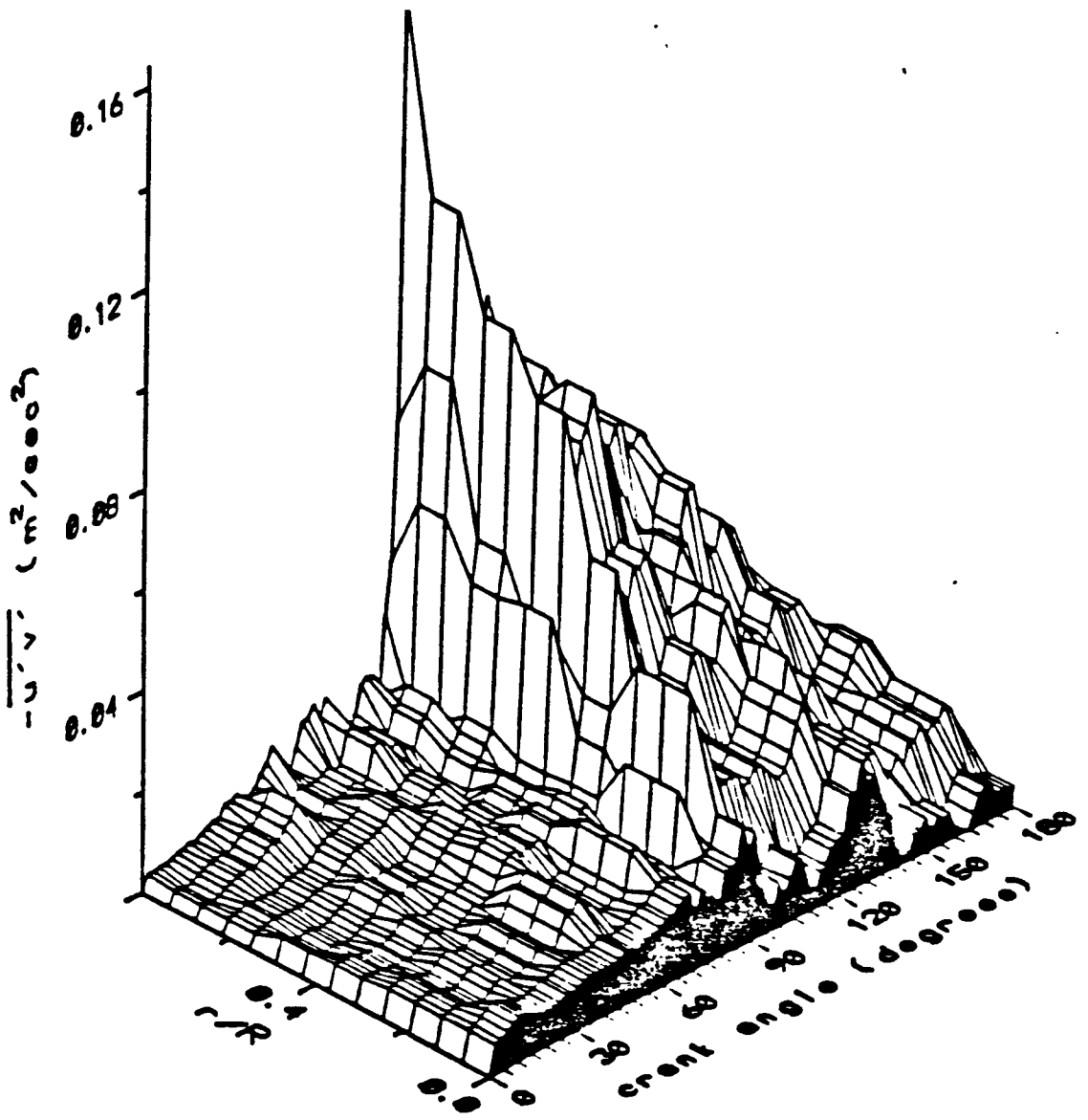

Figure 68: 3D view of Reynolds shear stress at s/d = 30 (smoothed).

3.3.5. Results at s/d = 44

At the furthest downstream axial station, the boundary layer has seen the longest development length. The boundary layer is thicker, prior to transition, than at the other stations, extending out as far as y/R = 0.4 (Fig. 69). Transition occurs abruptly at approximately 106°, one effect of which is to shift the peak rms-velocity fluctuation toward the wall for post-transition crank positions. The peak prior to transition at 90° is at y/R = 0.133, while it is a maximum at y/R = 0.027 for 106°.

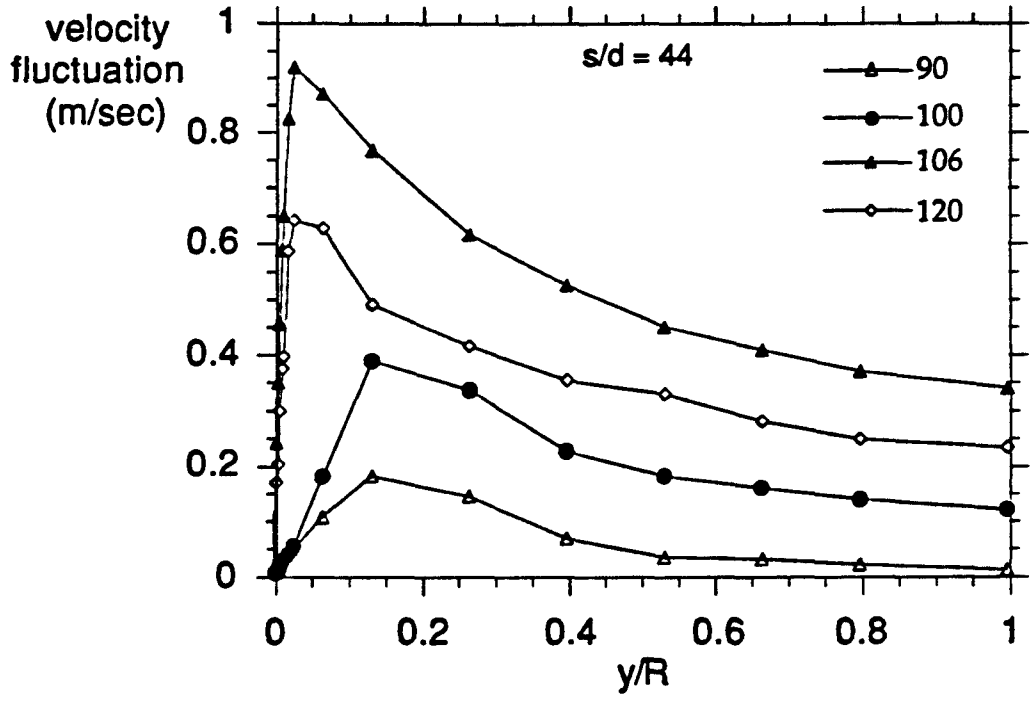

Figure 69: Profiles of streamwise velocity fluctuation at s/d = 44.

The developing boundary layer is nearly isotropic, as evidenced in Figure 70. Even under conditions of a strong adverse pressure gradient at 140°, the flow follows the turbulent model, as in Figure 71. Note that the two data points nearest to the wall, at y^+ = 0.24 and y^+ = 0.65, are below the minimum y^+ of the figure. The corresponding u^+ values for those points are 1.29 and 1.33, respectively. During the first 90° of flow, the

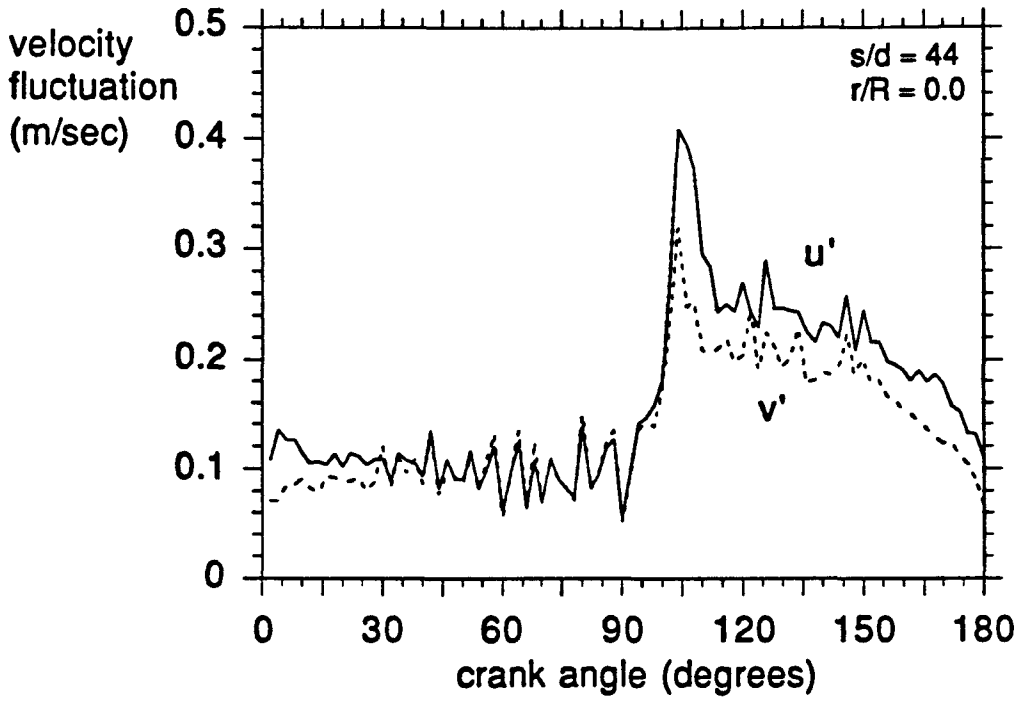

Figure 70: Centerline streamwise and radial velocity fluctuation at s/d = 44.

acceleration has a stabilizing effect, reducing the fluctuations in the core (Fig. 72).

Like that of s/d = 30, the flow at s/d = 44 sees an abrupt rise in Reynolds shear stress as the flow undergoes transition (Fig. 73). Note that the data of Figure 73 were smoothed to aid in the qualitative assessment of the transition process. In the 70° of the cycle immediately following transition, the average shear stress is 0.0340 m^2/sec^2. This is in comparison to an average shear stress of 0.0083 m^2/sec^2 for that portion of the cycle between 30° and 90°. Table 8 is a compilation of the maximum, minimum, and average shear stresses (in m^2/sec^2) measured at each axial station.

The averages are calculated from the data for all radii for the given range of crank position during the first half-cycle. It is evident that the level of turbulent activity after transition increases as the boundary layer grows spatially along the pipe wall.

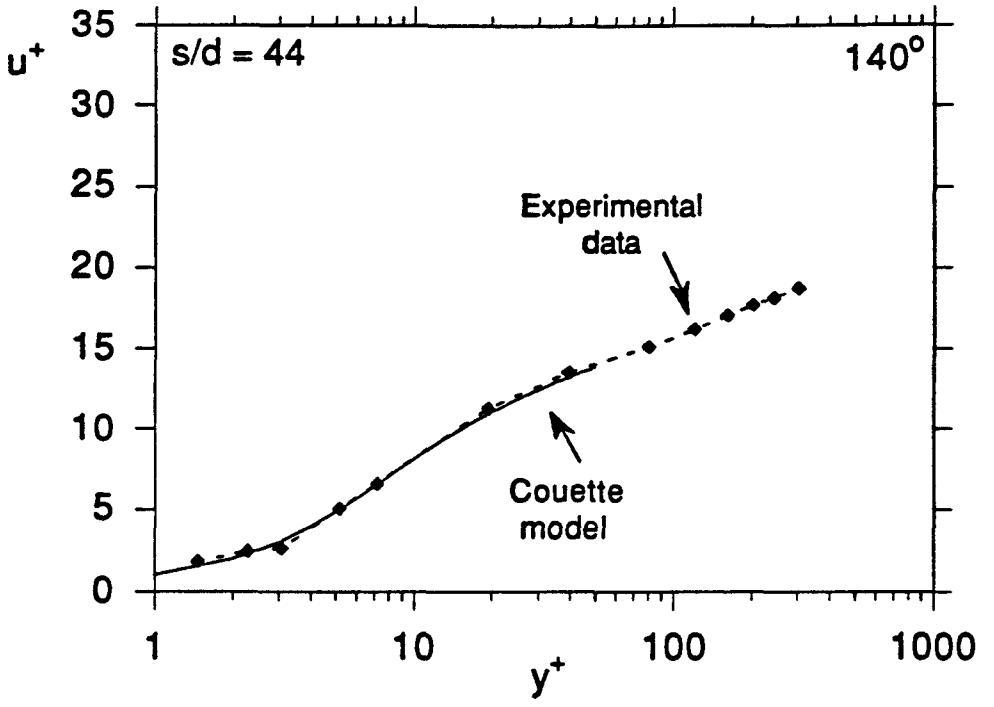

Figure 71: Velocity profile in wall coordinates at 140° for s/d = 44.

s/d	$-\overline{u'v'}$ max	$-\overline{u'v'}$ min	$-\overline{u'v'}$ ave	$-\overline{u'v'}$ ave
0.33	0.0327	-0.0032	0.010 (30° - 70°)	0.008 (72° - 150°)
16	0.1043	-0.0038	0.004 (2° - 58°)	0.022 (60° - 120°)
30	0.1464	-0.0131	0.006 (0° - 84°)	0.038 (86° - 150°)
44	0.1789	-0.0043	0.008 (30° - 90°)	0.034 (92° - 160°)

Table 8: Maximum, minimum, and average Reynolds shear stress, in m^2/sec^2

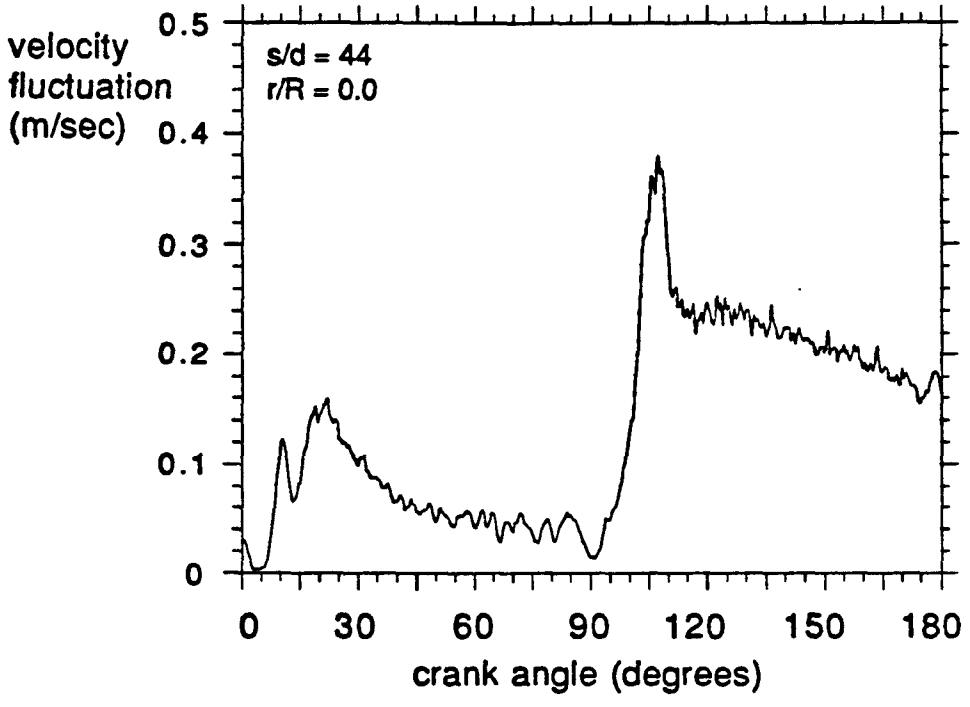

Figure 72: Centerline streamwise velocity fluctuation at s/d = 44.

Important to the analysis of turbulent oscillating flow is a comparison to turbulence in unidirectional flow. Figure 74 is a plot of profiles of Reynolds shear stress, normalized by the square of the instantaneous friction velocity. Although the profile data are not completely converged, as discussed in Section 3.1.2., a comparison to steady flow is useful. As the flow passes through transition, the profiles more closely approximate what would be expected in a mature, unidirectional, turbulent flow; specifically, a profile extending from 1 at the wall to 0 at the centerline (straight line -- from present measurements and Laufer, 1953). Prior to transition, the profiles are flatter, while post-transition sees the effect of enhanced cross-stream transport, as evidenced by the profiles at 120° and 140°, which more closely emulate turbulent flow. The reason for the rather high normalized values in the tube center at crank position (θ = 100°) prior to transition is unknown. It should be noted, however, that this profile has a very low normalizing shear velocity (see Fig. 78) and, thus, is one with much lower shear stresses than those in post-transition cycle positions.

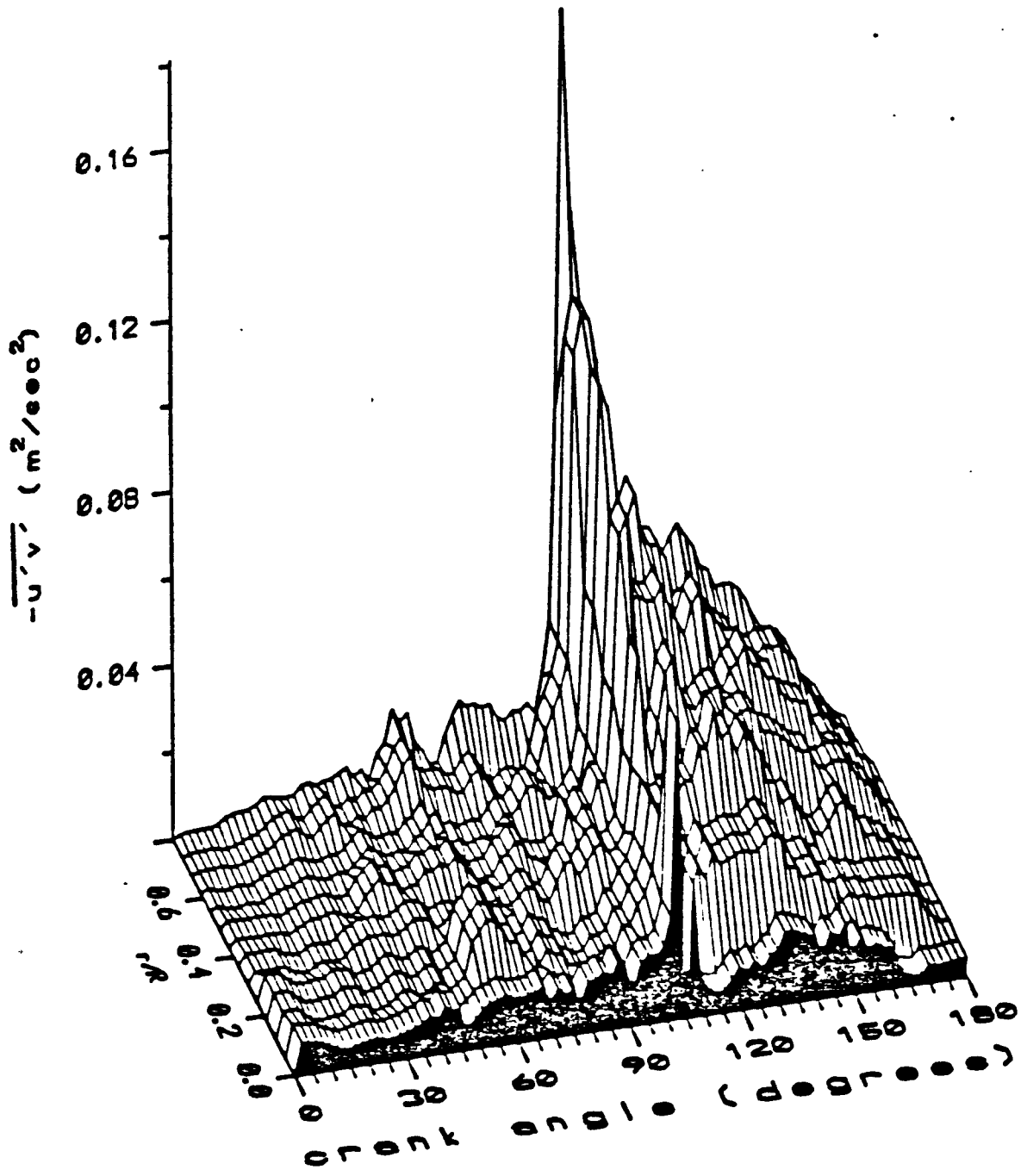

Figure 73: 3D view of Reynolds shear stress at s/d = 44 (smoothed).

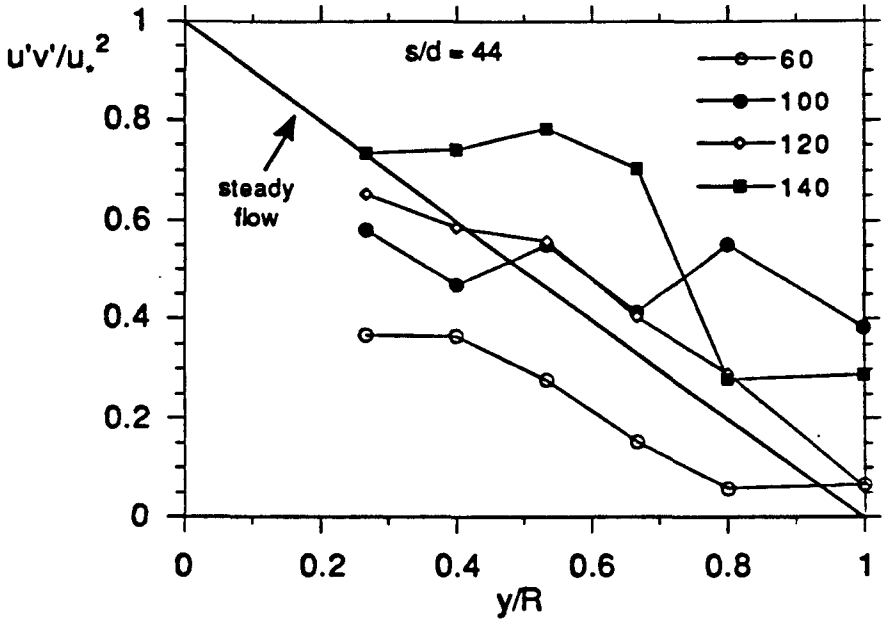

Figure 74: Profiles of normalized Reynolds shear stress at s/d = 44.

Note: Profile data are not completely converged, as shown in Figure 13 and discussed in Section 9.2

Figure 75 is a three-dimensional plot of the correlation coefficient, $-\overline{u'v'} / u' \cdot v'$, which is denoted by the symbol ψ. The plot was generated from the smoothed cross-wire data for the Reynolds shear stress and the streamwise and axial rms-velocity fluctuations. Note that the first 18 degrees of data are not plotted since there is significant scatter for this early portion of the cycle. The average correlation coefficient for the range $r/R \leq 0.8$ is 0.42 for the turbulent flow portion of the cycle, $106° \leq \theta \leq 180°$. This value compares well to that measured in the relatively flat core-flow region of fully-developed turbulent pipe flow. The average correlation coefficient calculated by Laufer (1953) for $r/R \leq 0.6$ is approximately 0.41 for $Re_d = 50{,}000$ and 0.50 for $Re_d = 500{,}000$. For $r/R > 0.6$, the correlation coefficient decreases steadily to a value of zero at the wall.

It is worth noting that the correlation coefficient is quite high for the laminar-like portion of the cycle. The average correlation coefficient for the portion of the cycle, $20° \leq$

$\theta < 106°$, is 0.63. This suggests the presence of some coherent, large-scale structures in the flow.

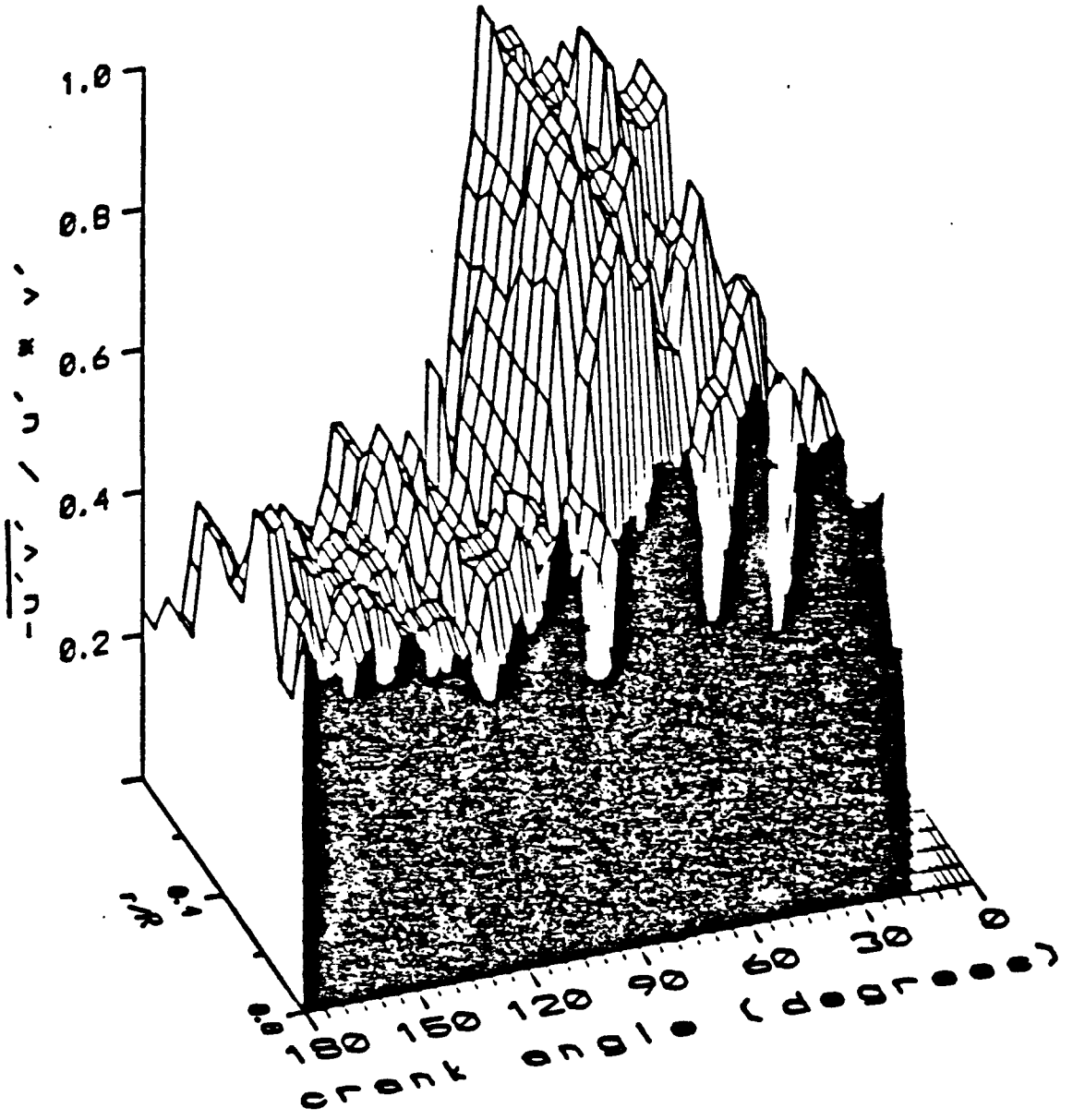

Figure 75: 3D plot of the correlation coefficient at s/d = 44.

3.3.6. Comparison to Computational Data

To test the accuracy of the pressure-gradient-influenced model for the laminar portion of the cycle, a unidirectional, unsteady flow analysis was performed by Ahn and Ibrahim, 1991. For the computation, the flow is accelerated from rest and occupies a

computational domain modelled on a pipe sufficiently long to avoid end effects. Thus, the velocity profiles develop independent of the axial position and can be used to isolate the effect of acceleration.

Figure 76 compares the computational results with the experimental data and the Couette model used in processing the data at 30°, a crank position of strong favorable pressure gradient. The Couette model and numerical model curves diverge near $y^+ = 8$, where the Couette flow assumption becomes suspect and, perhaps, the assumption that past acceleration history is unimportant breaks down. Over the range used for determining the friction velocity ($0 < y^+ < 10$), the Couette model and computation agree.

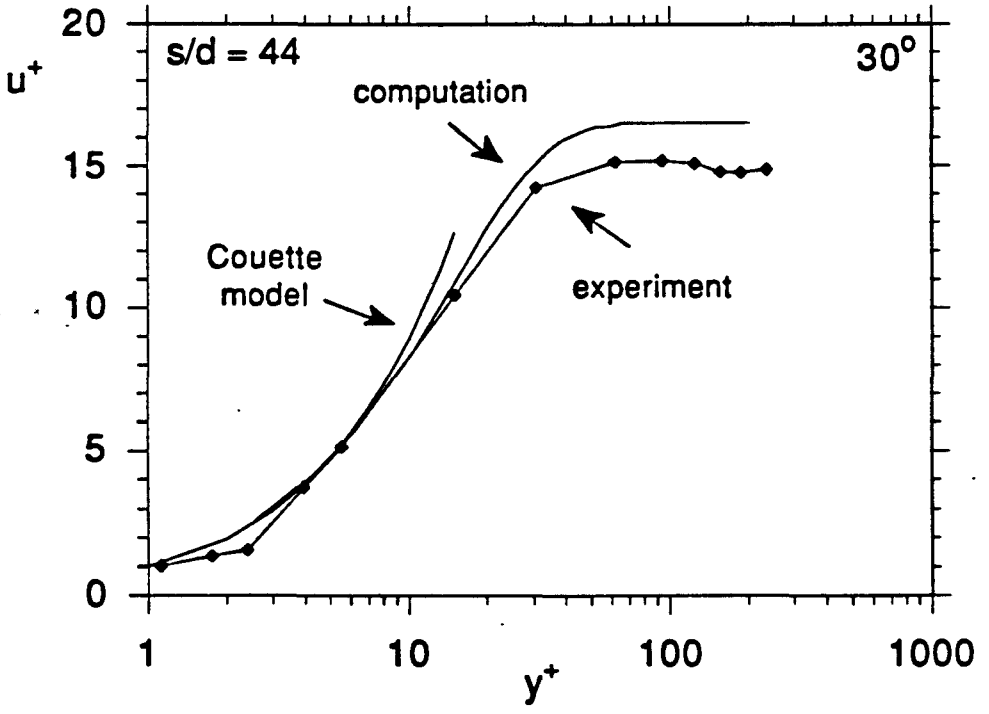

Figure 76: Velocity profiles in wall coordinates at 30° for s/d = 44.

The cause of the low u^+ value at $y^+ = 2.4$ is known. It was acquired after the probe was accidentally deformed at the wall. Since the orientation of the sensor after touching the wall was more in line with the flow, the effective cooling may have been reduced. Thus, it is expected that the correct value should be higher, in agreement with the two models to which the data are being compared. Note that this error is also seen at $y^+ = 3.1$ in Figure 71. The other data are considered to not be in error because they were acquired (in a randomized sequence) prior to this point.

Figure 77 illustrates profiles of nondimensionalized velocity at 80° for s/d = 44. This point, late in the acceleration phase but still in the laminar regime, is one with a small pressure gradient effect. Once again, the models agree over the y^+ range where the Couette flow model was used for data reduction, and the data agree with the models out to $y^+ =$ 10. The skin friction plot (Fig. 78) appears much like that of s/d = 30 (Fig. 67), although the post-transition values are as much as 21% higher for s/d = 44 in the range of crank position, $120° \leq \theta \leq 160°$.

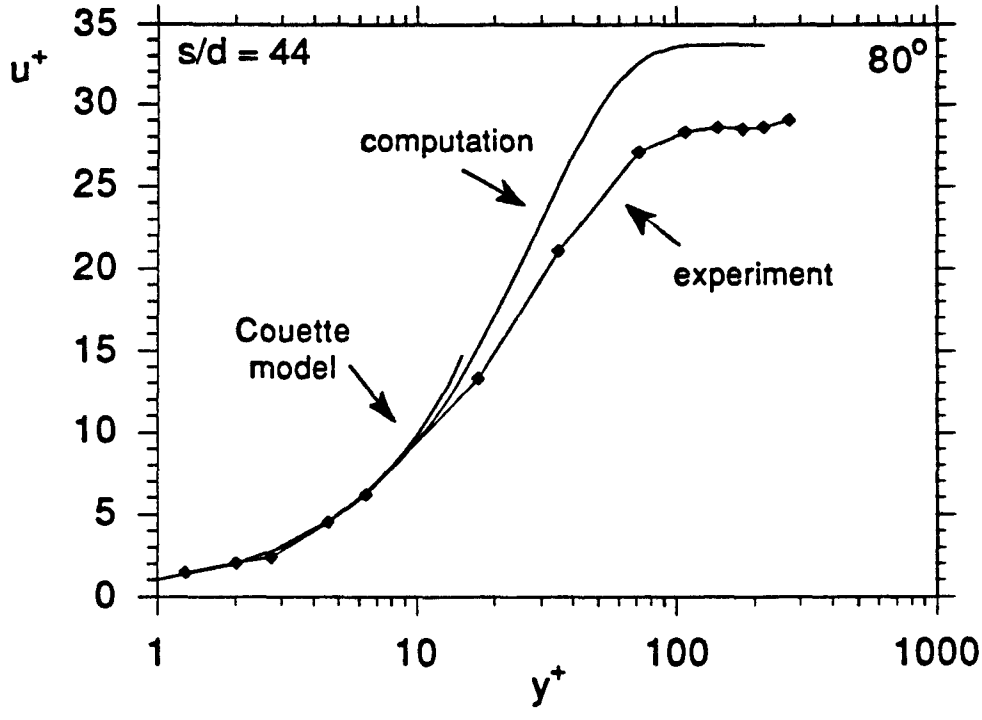

Figure 77: Velocity profiles in wall coordinates at 80° for s/d = 44.

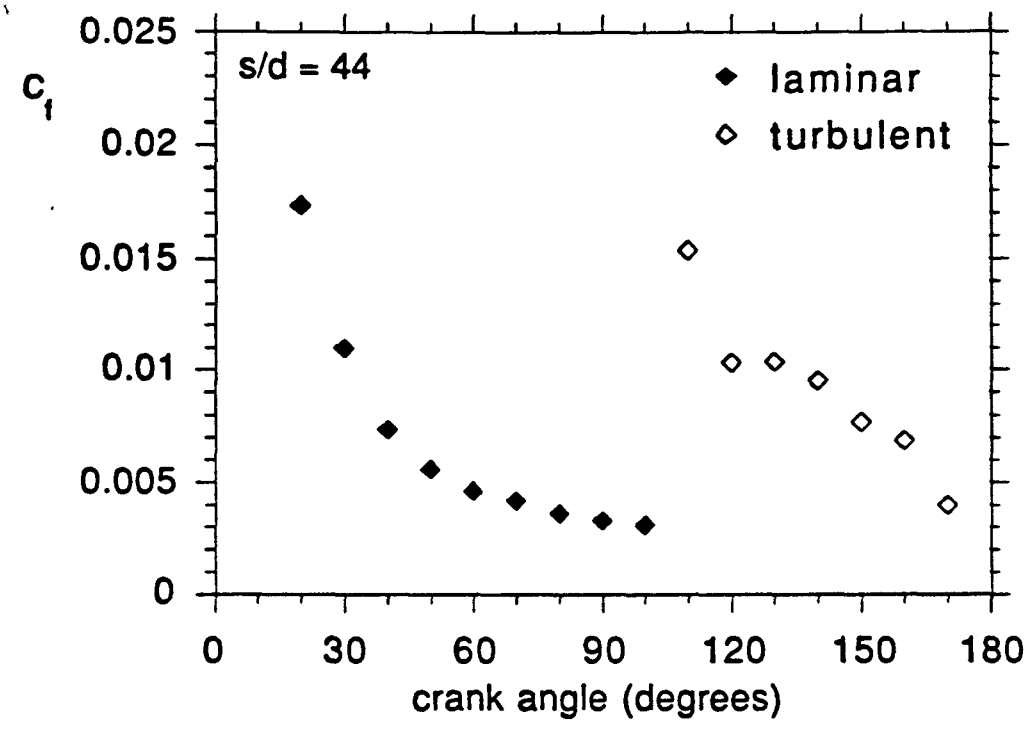

Figure 78: Skin friction coefficient for s/d = 44.

Figure 79 is a cumulative plot of skin-friction coefficients for all four axial stations. The diagonal coordinate, s, is the streamwise distance measured from the open end of the duct. The plot helps to illuminate the passage of the convected turbulent slug and its effect on boundary layer transition.

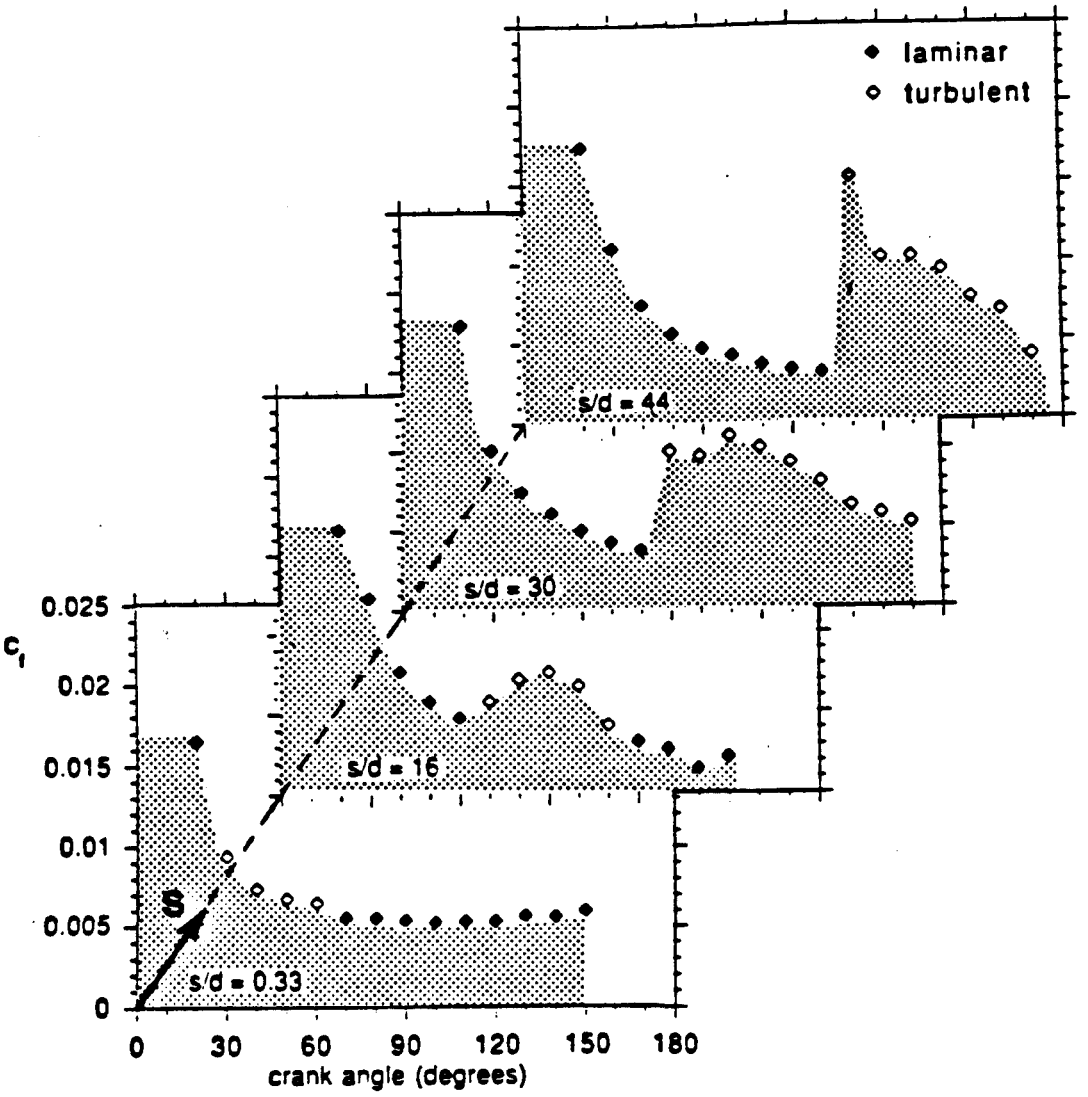

Figure 79: Skin-friction coefficient for all four axial stations.

3.3.7. Modeling with Steady, Fully-developed Pipe Flow Correlations

A comparison was made between actual experimental data for skin friction coefficients and values computed from quasi-steady, fully-developed tube-flow correlations. Two different correlations were used, one laminar, the other turbulent. When experimental data indicated a laminar flow, the laminar correlation was used for comparison. Likewise, the turbulent correlation was plotted when the experimental data indicated turbulent flow.

The Darcy friction factor, f, for laminar flow is given by (Fox and McDonald, 1978):

$f = \frac{64}{Re_d}$ (where Re_d represents the Reynolds number, $\frac{u_m d}{\nu}$).

Since the skin friction coefficient, C_f, is one-fourth the Darcy factor:

$$C_f = \frac{16}{Re_d} \tag{25}$$

And, for turbulent flow (Fox and McDonald, 1978)

$$C_f = 0.070(Re_d)^{-\frac{1}{4}} \quad ; \quad 4000 < Re_d < 10^5 \tag{26}$$

The diameter Reynolds number is based upon the bulk-mean velocity, u_m, at the position within the cycle that is being evaluated.

Figures 80 through 83 show that the predictions made by the turbulent correlation are in better agreement with experimental results than are those predictions made by its laminar counterpart. It should be noted, however, that the turbulent correlation tends to diverge from the experimental values as the fluid approaches flow reversal.

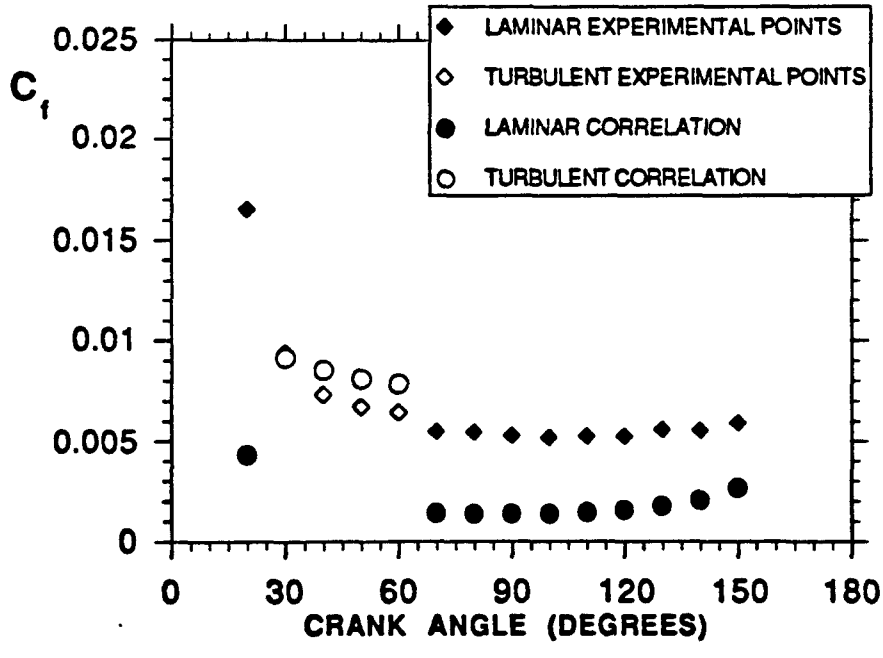

Figure 80: Comparison of the measured skin friction coefficients with values computed from steady, fully-developed tube flow correlations. The experimental data was used to determine flow regime, laminar or turbulent. s/d = 0.33.

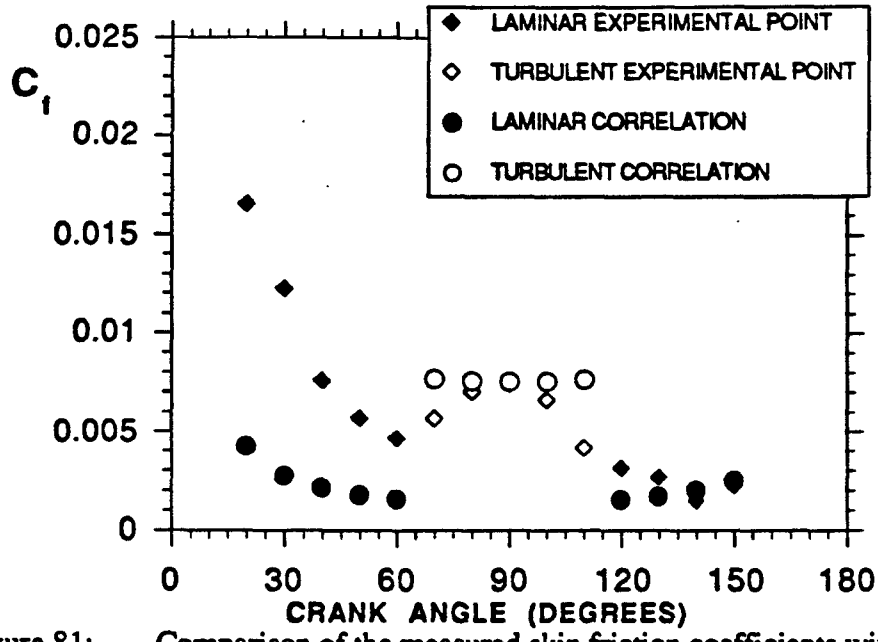

Figure 81: Comparison of the measured skin friction coefficients with values computed from steady, fully-developed tube flow correlations. The experimental data was used to determine flow regime, laminar or turbulent. s/d = 16.

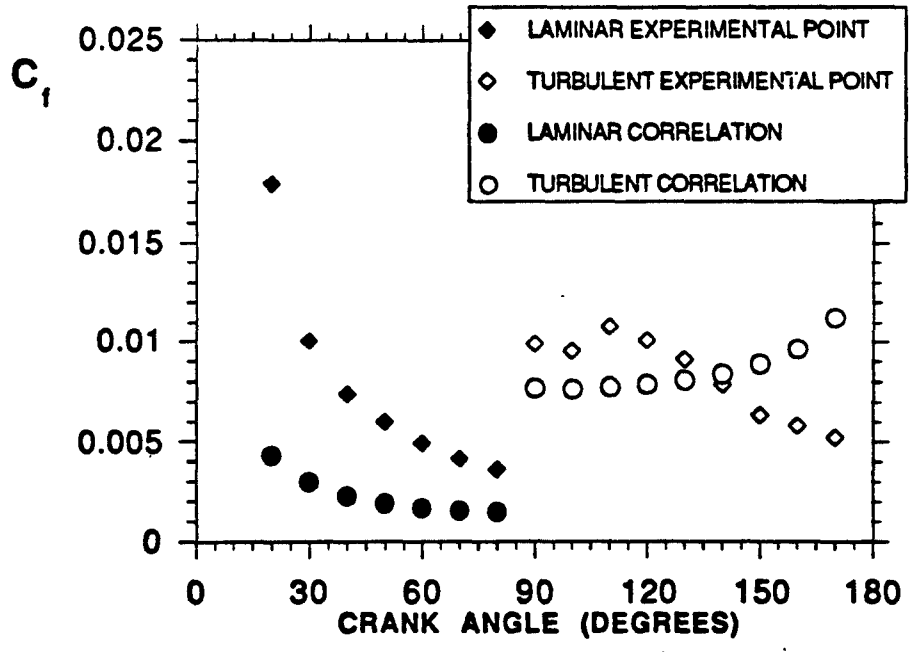

Figure 82: Comparison of the measured skin friction coefficients with values computed from steady, fully-developed tube flow correlations. The experimental data was used to determine flow regime, laminar or turbulent. s/d = 30.

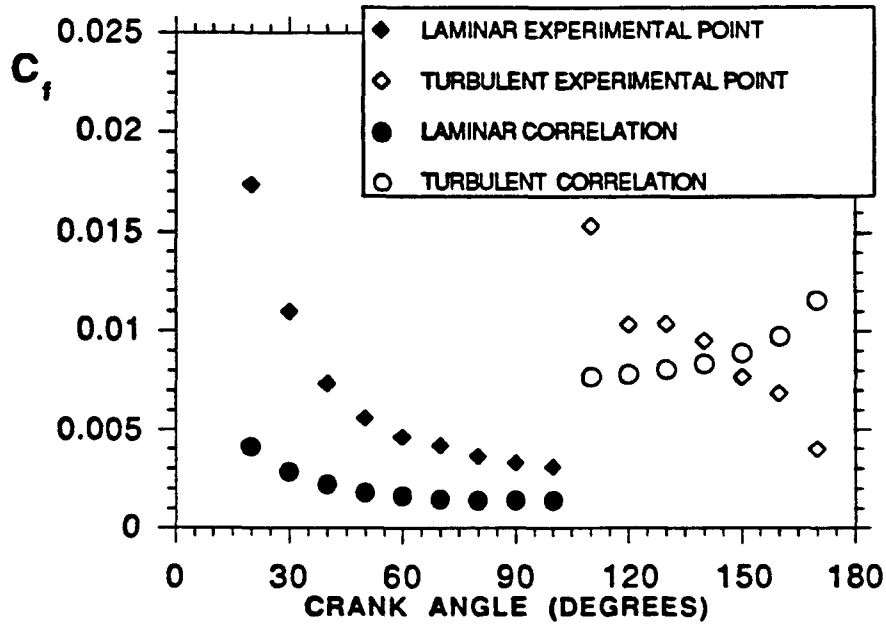

Figure 83: Comparison of the measured skin friction coefficients with values computed from steady, fully-developed tube flow correlations. The experimental data was used to determine flow regime, laminar or turbulent. s/d = 44.

Using GLIMPS (Gedeon,1990) to Determine the Transition Point

Comparisons were made between prediction and data using GLIMPS to determine the point in the cycle of transition to turbulence and the point of return to laminar-like flow. In the model the following criteria are used:

Condition 1 - The "always laminar" condition:

$$R_e/R_o < \max\left(\sqrt{\frac{V_s}{V_c}}\ ,1\right) \qquad (27)$$

Where R_o=2000 is a critical Reynolds number, and V_c=25 a critical Valensi number.

Condition 2 - The "always turbulent" condition:

$$R_e/R_1 > \max\left(\sqrt{\frac{V_s}{V_c}}\ ,1\right) \qquad (28)$$

Where R_1=18000 represents a critical Reynolds number.

Condition 3 - The "convected triggering" condition:

This condition is concerned with the arrival of the "turbulent slug" at the axial position in question. The flow is presumed to be turbulent when the leading edge of the slug arrives at a given axial position. The following is used to find an expression for the point in the cycle at which a particular axial position will receive the leading edge of the slug:

$$U_{mean}(\theta) = U_{max}\mathrm{Sin}(\theta)$$

Substitute $\theta = \omega t$, $Re_{max} = U_{max} d / \nu$ and $s_{le}(t) = \int_0^t U_{mean} dt'$ gives:

$$s_{le}(t) = \frac{Re_{max}\,\nu}{d}\int_0^t \sin(\omega t)\, dt$$

where $s_{le}(t)$ is the position of the turbulent slug leading edge.

or

$$s_{le}(\theta) = \frac{Re_{max}\,\nu}{d\omega}\int_0^\theta \sin(\theta')\, d\theta'$$

s_{le} as a function of crank position, is given by:

$$s_{le}(\theta) = \frac{Re_{max}\,\nu}{d\omega}\left[\cos(\theta_{le}) - 1\right]$$

Solving for the crank angle, θ_{le}, at which the leading edge of the turbulent slug arrives at a given distance, s_{le}, downstream:

$$\theta_{le} = \mathrm{ArcCos}\left\{1 - \frac{sd\omega}{Re_{max}\,\nu}\right\} \qquad (29)$$

Thus:

A. If condition 1 holds, the flow is assumed laminar.

B. If condition 2 holds, the flow is considered to be turbulent.

C. If neither condition 1 nor condition 2 holds, the flow is considered turbulent if and only if condition 3 holds.

By observing Figs. 84 through 87, one can see that the GLIMPS model is fairly effective at predicting transition to turbulence. This can best be seen in the graphs of s/d=30 and 44. However, the model seems to fall short in correctly predicting the point of

relaminarization. For instance, in the s/d=0.33 graph, one may observe that the experimental data indicate a return to laminar-like flow at approximately 70° while the GLIMPS model predicts no relaminarization. The model assumes the turbulent slug to have a sharp leading edge, which is not true. This may account for the error in the predicted transition at s/d=0.33 and 16.

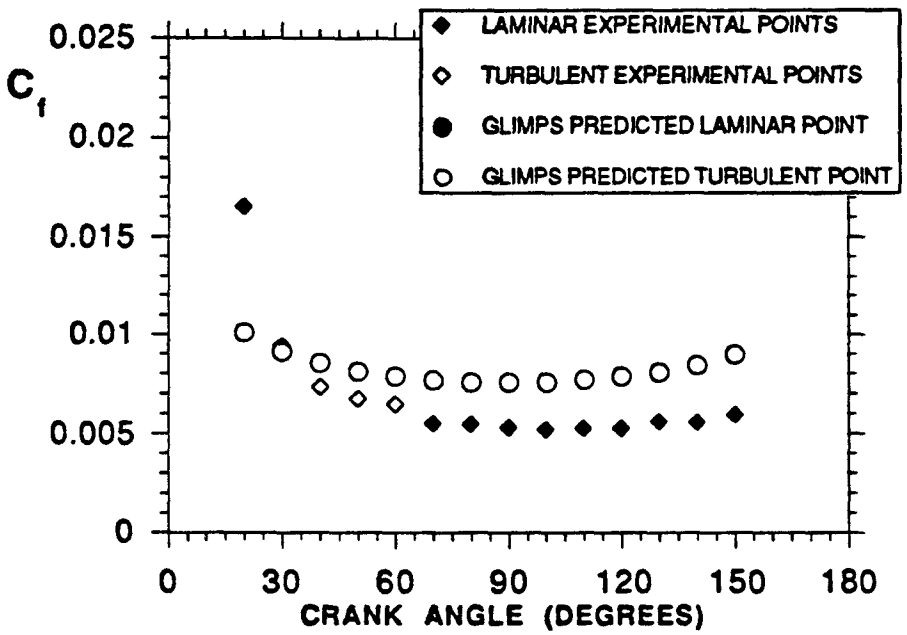

Figure 84: Comparison of skin friction data with values computed from steady-flow, fully-developed laminar and turbulent pipe flow correlations. Transition to turbulence by the GLIMPS Model, s/d = 0.33.

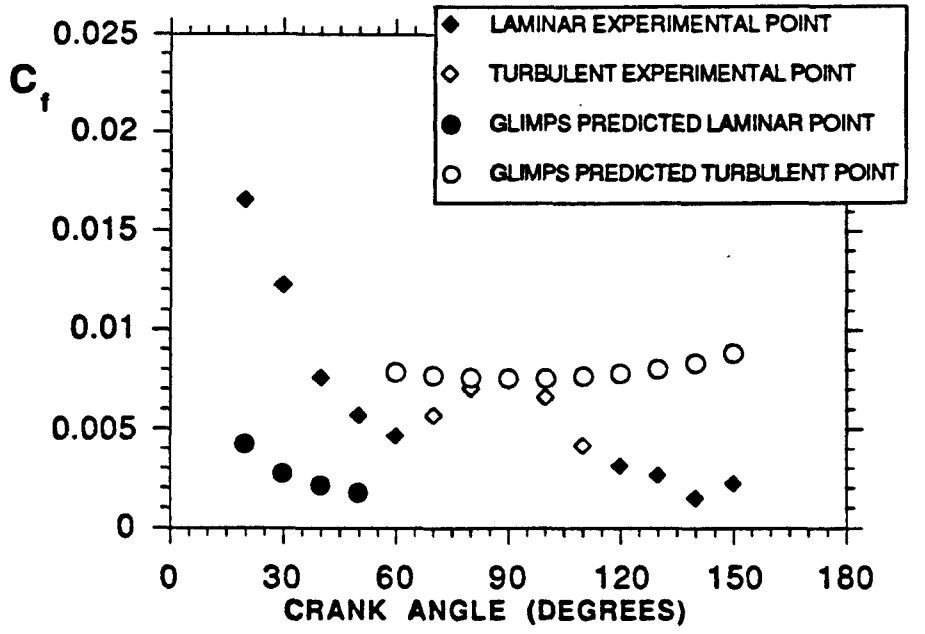

Figure 85: Comparison of skin friction data with values computed from steady-flow, fully-developed laminar and turbulent pipe flow correlations. Transition to turbulence by the GLIMPS Model, s/d = 16.

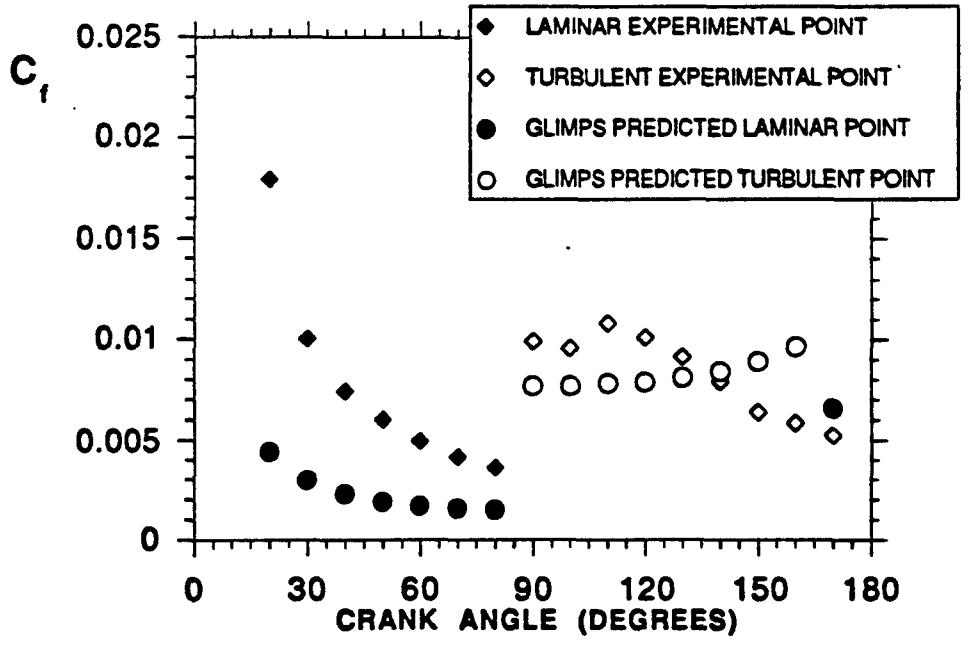

Figure 86: Comparison of skin friction data with values computed from steady-flow, fully-developed laminar and turbulent pipe flow correlations. Transition to turbulence by the GLIMPS Model, s/d = 30.

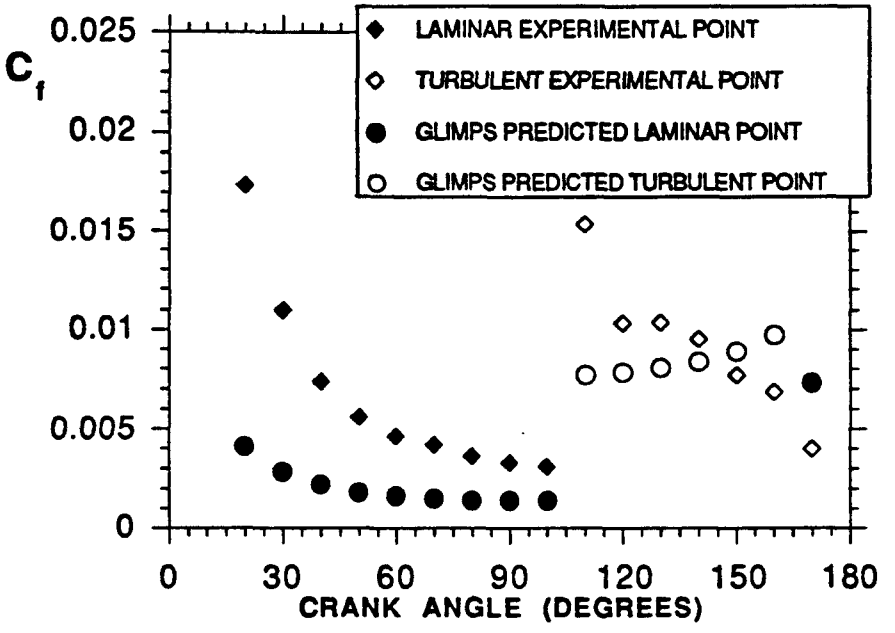

Figure 87: Comparison of skin friction data with values computed from steady-flow, fully-developed laminar and turbulent pipe flow correlations. Transition to turbulence by the GLIMPS Model, s/d = 44

Using a Modified GLIMPS Model

In this analysis, the GLIMPS model has been modified in an attempt to enhance its ability to predict the point of flow relaminarization. The modification was to allow for a trailing edge of the turbulent slug. The flow was assumed to relaminarize after the departure of the turbulent slug (if allowed by condition 2).

Because the volume of the turbulent slug is known, it is easiest to allow for its departure in terms of volume of flow that must be purged before the trailing edge arrives. This is similar to the leading edge calculation:

$$\theta_{te} = \text{ArcCos}\left\{1 - \frac{\left(\frac{s\pi d^2}{4} + V_o\right)d\omega}{\frac{\pi d^2}{4} Re_{max}\, \nu}\right\} ,$$

where V_o represents the turbulent slug volume, and θ_{te} is the position within the cycle of the arrival of the trailing edge of the turbulent slug.

In three of the four axial positions considered (Figs. 88 through 91), relaminarization is predicted too early in the cycle. Success can be seen in the first of the graphs, s/d=0.33, however.

Relaminarization does not necessarily coincide with the calculated turbulent slug departure. The slug would not have a flat trailing edge profile; the near-wall trailing edge of the slug would lag the calculated value.

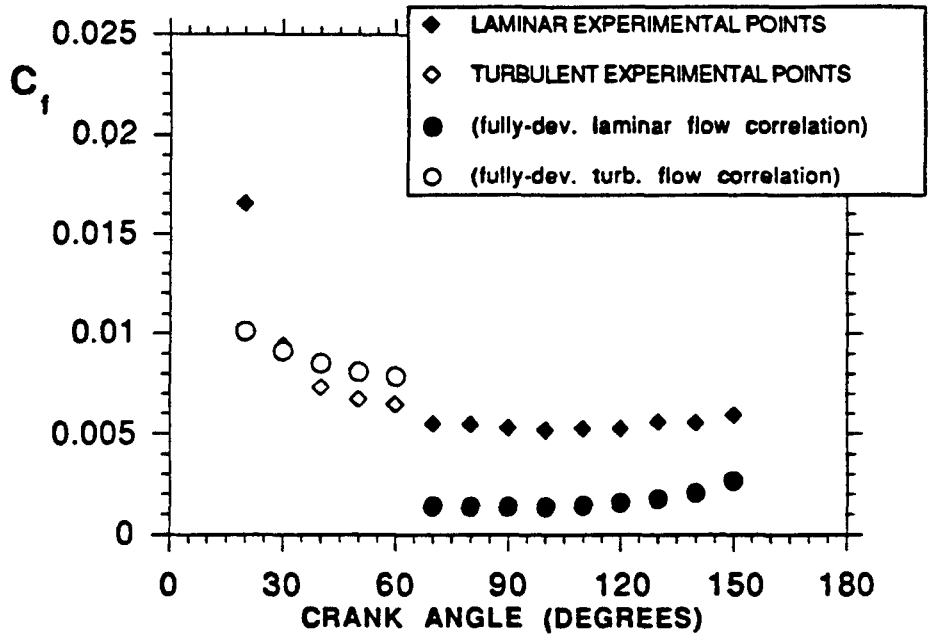

Figure 88: Comparison of skin friction data with values computed from steady-flow, fully-developed laminar and turbulent pipe flow correlations. Transition by the modified GLIMPS Model, s/d = 0.33.

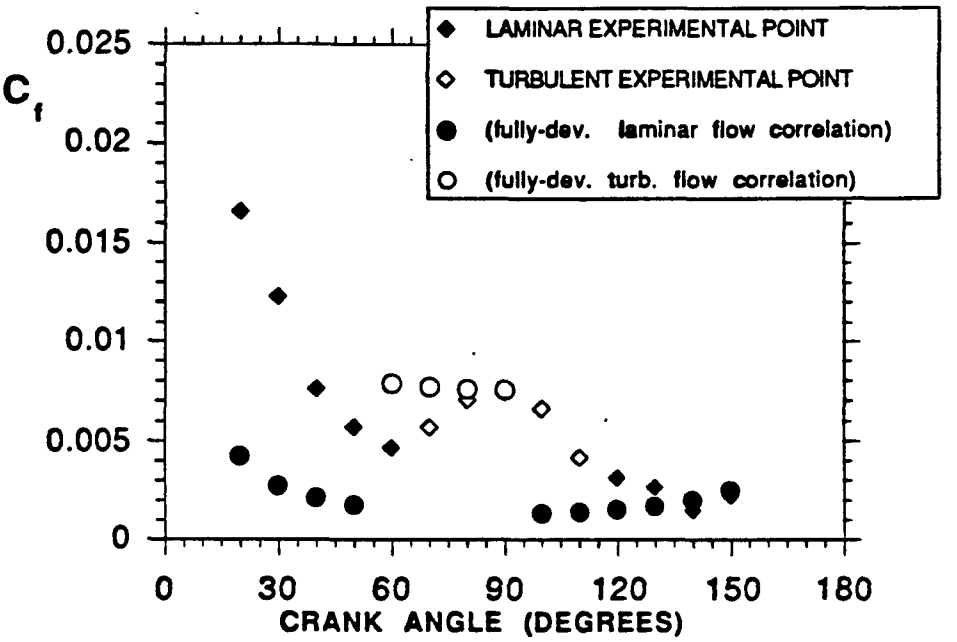

Figure 89: Comparison of skin friction data with values computed from steady-flow, fully-developed laminar and turbulent pipe flow correlations. Transition by the modified GLIMPS Model, s/d = 16.

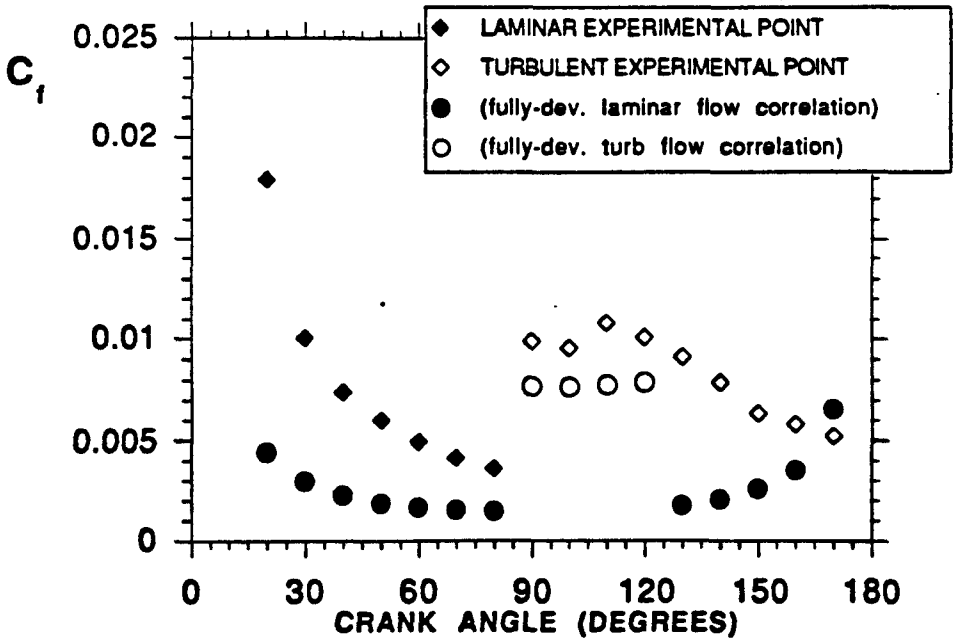

Figure 90: Comparison of skin friction data with values computed from steady-flow, fully-developed laminar and turbulent pipe flow correlations. Transition by the modified GLIMPS Model, s/d = 30.

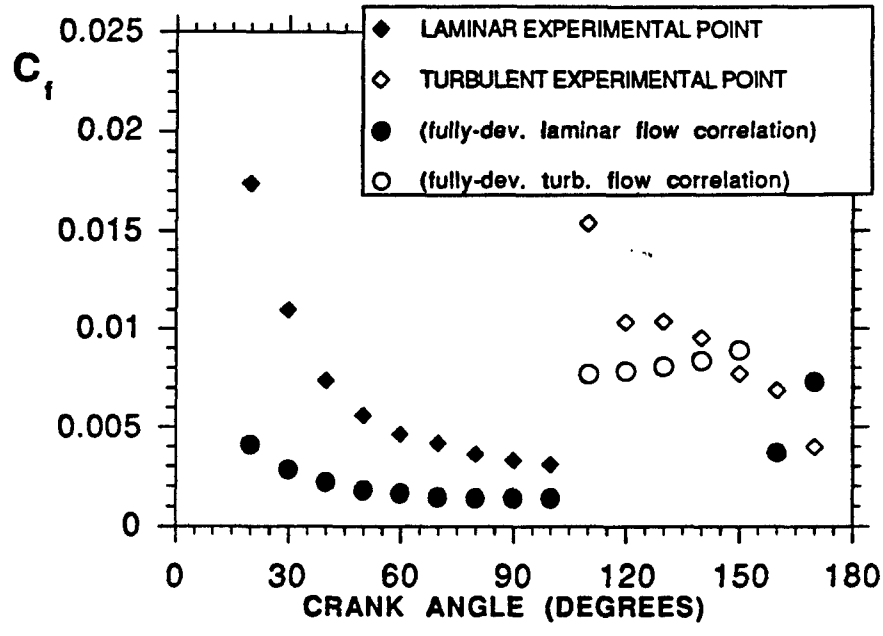

Figure 91: Comparison of skin friction data with values computed from steady-flow, fully-developed laminar and turbulent pipe flow correlations. Transition by the modified GLIMPS Model, s/d = 44.

Using a Boundary Layer Transition Model

The following applies a boundary layer correlation which is based upon the momentum thickness Reynolds number (Re_{δ_2}) for predicting transition in oscillating flow. Actual momentum thickness values are computed from the data as:

$$-\delta_2 \bar{u}^2 \rho 2\pi R = \int_{r_e}^{R} \rho \bar{u}\left(\frac{r}{R}\right)\left[\bar{u}_c - \bar{u}\left(\frac{r}{R}\right)\right] 2\pi r dr$$

a modification of the flat-plate boundary layer form. In this expression, r_e represents the edge of the boundary layer (or the edge of the core) $\bar{u}$ represents the streamwise component of the ensemble averaged velocity, and $\bar{u}_c$ represents the core velocity.

Critical values of the momentum thickness Reynolds number are calculated from the following expression presented by Mayle, 1991:

$$Re_{\delta 2,crit} = 400(Tu\%)^{-5/8}$$

where Tu is the core-average turbulence intensity, computed from:

$$Tu(\theta, s/d) = \frac{U'_{mean}(\theta, s/d)}{U_m(\theta, s/d)} \times 100$$

where U'_{mean} represents the rms-velocity fluctuation averaged over the cross-sectional area of the core, and u_m is the bulk-mean velocity. Figures 92 through 95 show the measured momentum thickness Reynolds numbers compared with critical Re_{δ_2} values at certain points throughout the half-cycle. When the measured values exceed the critical values, the flow is assumed to be turbulent. It can also be seen that at s/d=16, the lines intersect a second time as the actual values dip back below the critical line, indicating a return to laminar-like flow.

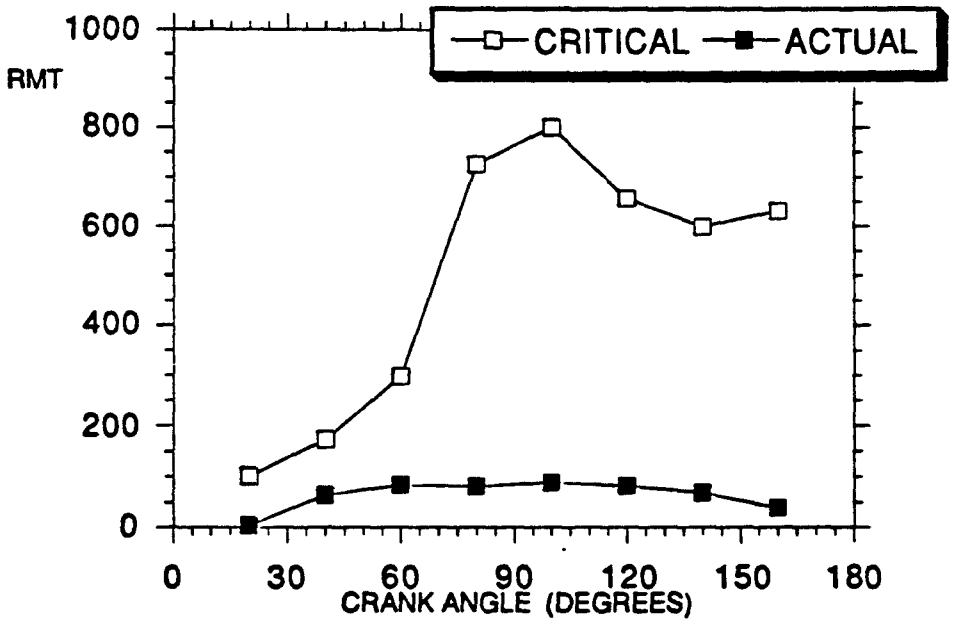

Figure 92: Measured and critical momentum thickness Reynolds numbers for the SPRE operating point, s/d=0.33.

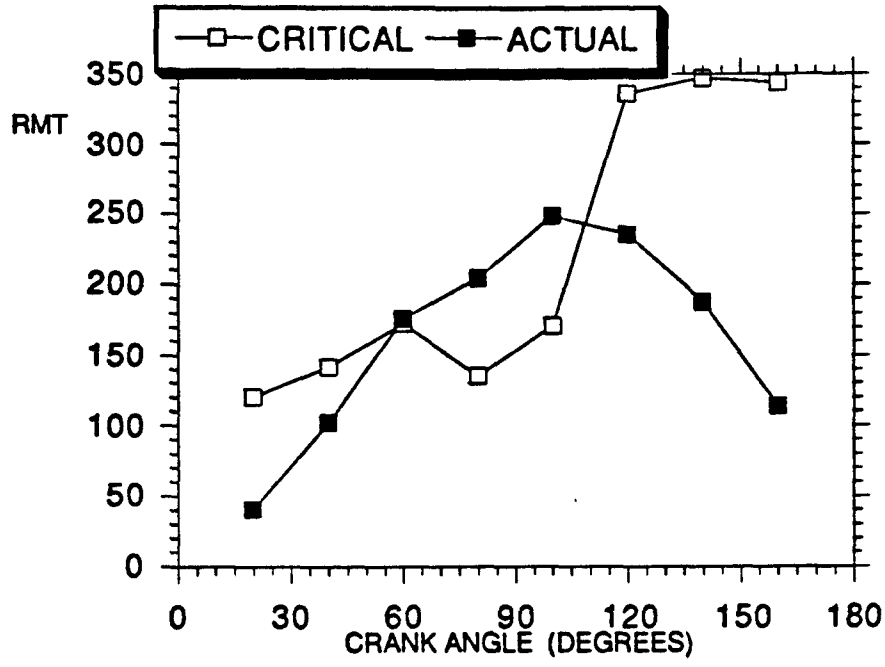

Figure 93: Measured and critical momentum thickness Reynolds numbers for the SPRE operating point, s/d=16.

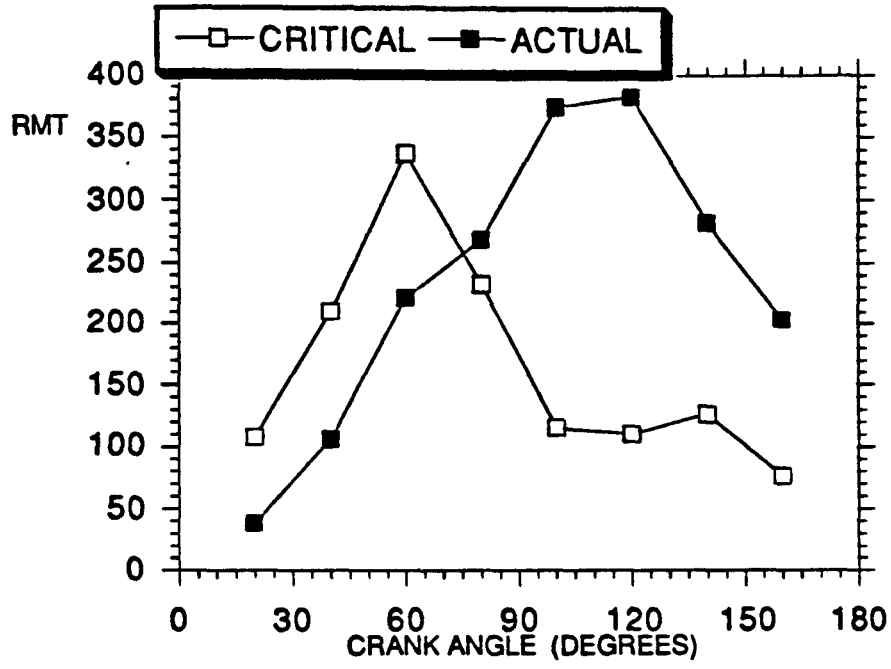

Figure 94: Measured and critical momentum thickness Reynolds numbers for the SPRE operating point, s/d=30.

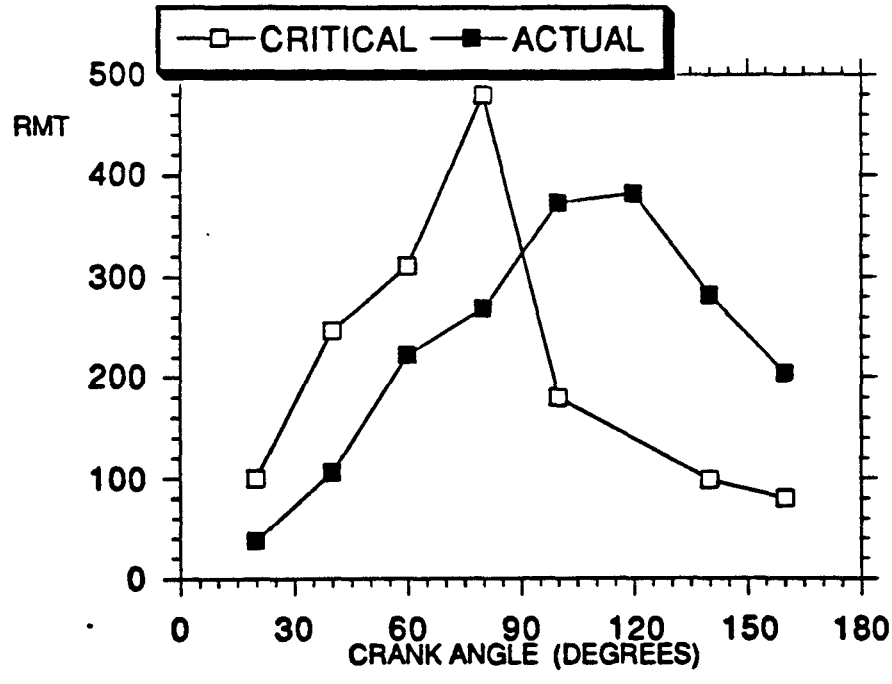

Figure 95: Measured and critical momentum thickness Reynolds numbers for the SPRE operating point, s/d=44.

Figures 96 through 99 show the same correlation values for C_f (as used above) compared to experimental data. Application of the flat-plate correlation shows promise. The correlation did not allow for relaminarization at s/d=30 and 44, even after the calculated time of turbulent slug departure from these axial positions. This is in agreement with experiments. Furthermore, the predictions do allow for relaminarization at s/d=16, again, the experimental results concur.

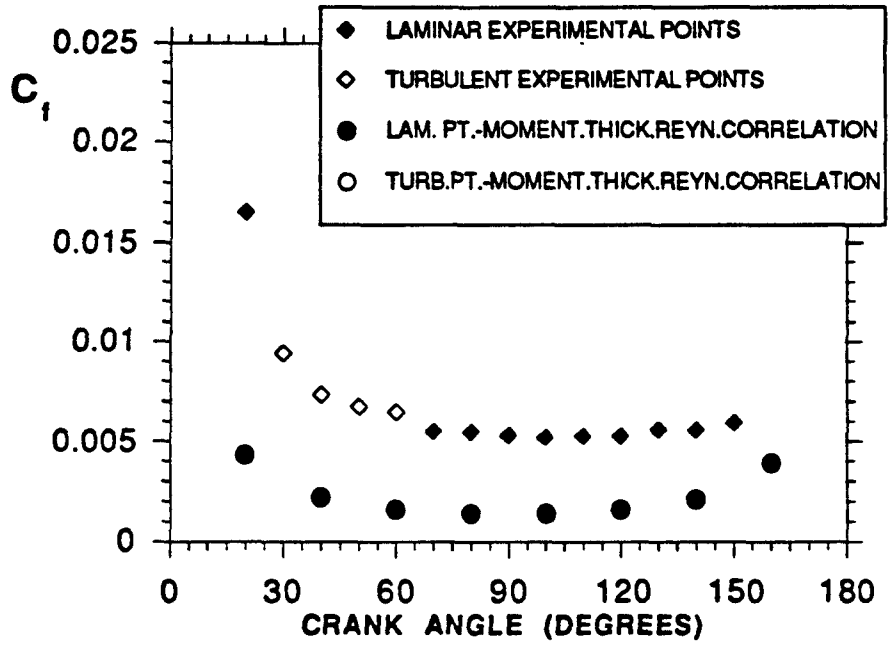

Figure 96: Comparison of skin friction data with values computed from steady-flow, fully-developed laminar and turbulent pipe flow correlations. Transition by the modified Boundary Layer Model, s/d = 0.33.

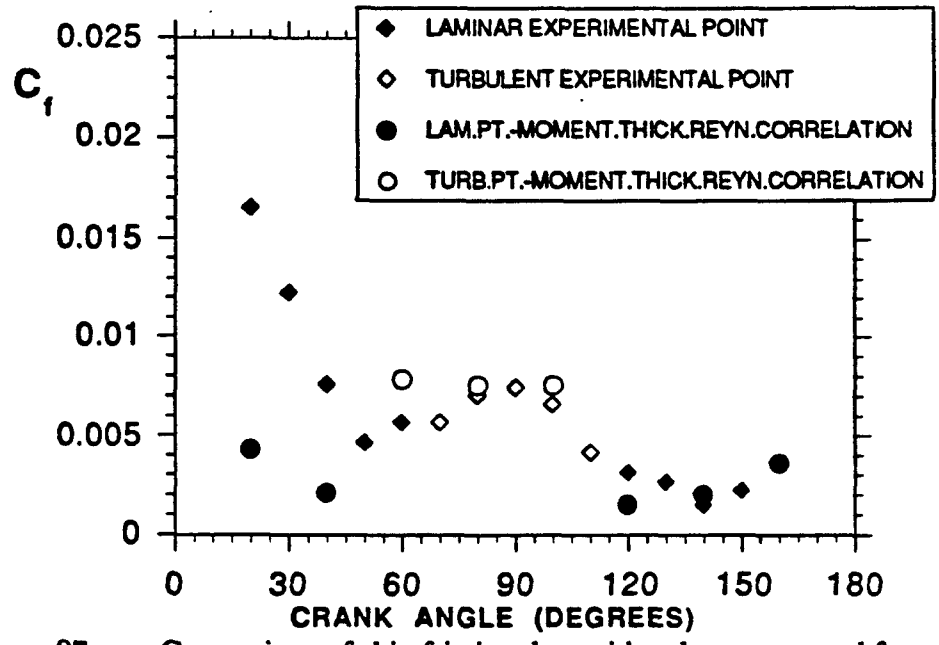

Figure 97: Comparison of skin friction data with values computed from steady-flow, fully-developed laminar and turbulent pipe flow correlations. Transition by the modified Boundary Layer Model, s/d = 16.

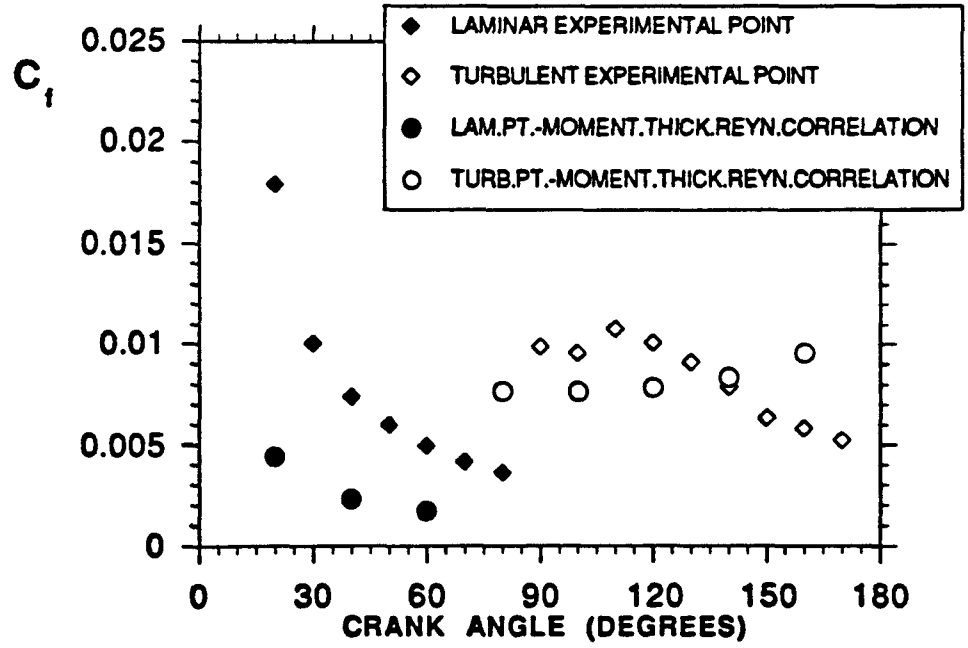

Figure 98: Comparison of skin friction data with values computed from steady-flow, fully-developed laminar and turbulent pipe flow correlations. Transition by the modified Boundary Layer Model, s/d = 30.

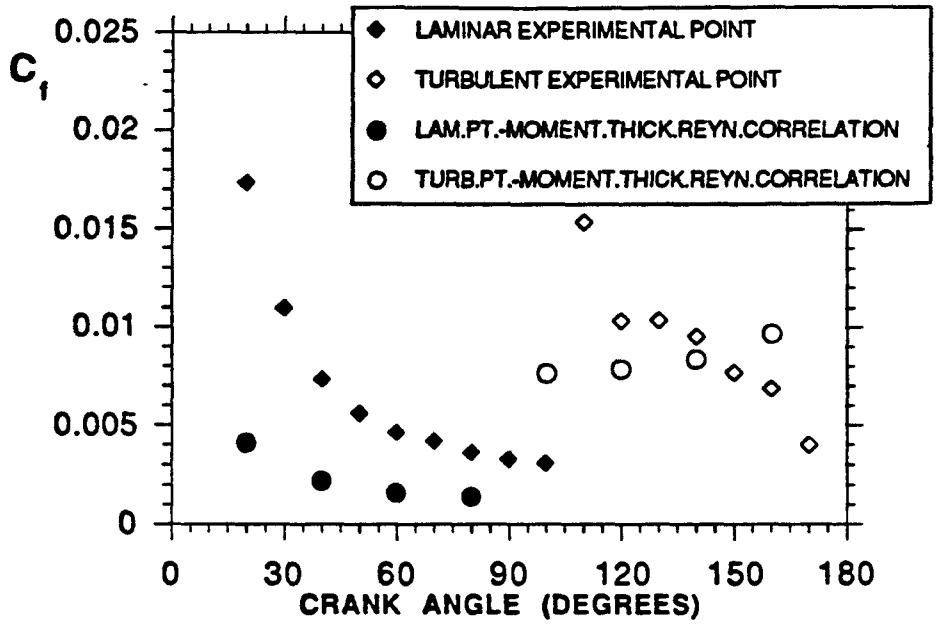

Figure 99: Comparison of skin friction data with values computed from steady-flow, fully-developed laminar and turbulent pipe flow correlations. Transition by the modified Boundary Layer Model, s/d = 44.

3.4. TEST RESULTS WITH A FLUSH-SQUARE ENTRY

As is evident from the above, transition is strongly dependent on upstream flow conditions which, in turn, are largely a function of the inlet geometry. While smooth nozzles were employed in the above experiments to avoid separation upon inflow to the test section, they are not representative of the inlet geometries of Stirling engine heat exchangers. For the introductory study of oscillating flow, it was decided that separation should be eliminated until a better understanding of the basic characteristics of oscillating flow was in hand. In order to more closely model flow conditions in actual engines, and in conjunction with pressure drop work in oscillating flow (Koester, et al., 1990), a continuation program was initiated to test the effects of various inlet geometries. The following discussion documents the first stage of that study.

In this section, test results from experiments with a flush-square entry (Fig. 100) are presented and compared with data from the smooth nozzle entry study. For the present study, the flow nozzles and heat exchanger cores were removed. The entry at the room end of the test section consisted of a 0.254 m (10 inch) diameter disk mounted flush with the

end of the pipe. At the drive end, the test section was attached to the mounting plate via a 12.7 cm (5 inch) flange and rubber gasket for sealing. Note that the flow at the drive end was constrained by a cross-section which opened up from the test section diameter of 3.81 cm (1.5 inch) to the piston diameter of 12.7 cm (5 inch). Measurements were taken at three axial stations, s/d = 16, 30 and 44. Ensemble averaging was performed for 50 cycles since the aim of the test was to illuminate the qualitative differences between inlet geometries.

Figure 101 is a plot of near-wall, streamwise velocity traces at r/R = 0.96 and r/R = 0.959 for the flush square and nozzle inlets, respectively, at the s/d = 16 station. Note that the flush square trace is offset by 2 m/sec. Although the velocity trace for the nozzle is interrupted between 25° and 40° by the passage of higher-velocity flow, the two traces are very similar prior to the arrival of the slug of turbulence, near 65°. The arrival of advected turbulence near 65° is evident in both traces, although the flush square velocity rises more steeply. As is evident in Figure 102, near-wall traces of rms-velocity fluctuation for which the flush square trace offset is 0.35 m/sec, high levels of fluctuation persist through flow reversal. This is due to turbulence generated in the free shear layer of the separation zone, near the point of flow entry, which is continuously advected downstream during this portion of the cycle.

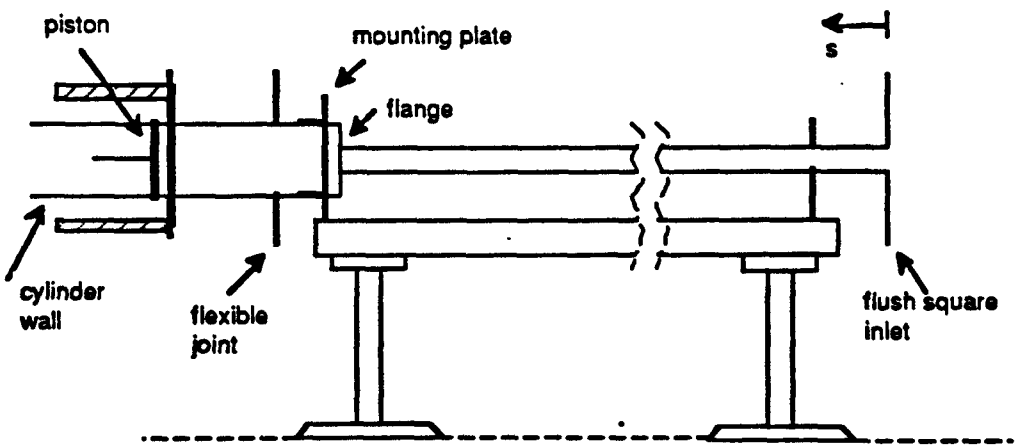

Figure 100: Flush square inlet geometry.

The nozzle and the flush-square geometries differ in their effects on turbulence generation upon inflow. The nozzle introduces a slug of turbulence which arose from separation during outflow of the previous cycle. This turbulence is followed by quiet flow supplied via the heat exchanger passages upstream of the nozzle. This passing disturbance can be seen in the centerline velocity fluctuation traces of Figure 103, taken at s/d = 16 (flush square offset is 0.35 m/sec). On the other hand, for the flush square entry, the flow is unable to negotiate the abrupt 90° turn at inflow and hence, separates at the inlet plane. The result is that the flush square inlet serves as a continuous source of turbulence, feeding disturbed flow to the developing boundary layer, after the arrival of the leading edge of the turbulent flow, for the remainder of the half-cycle.

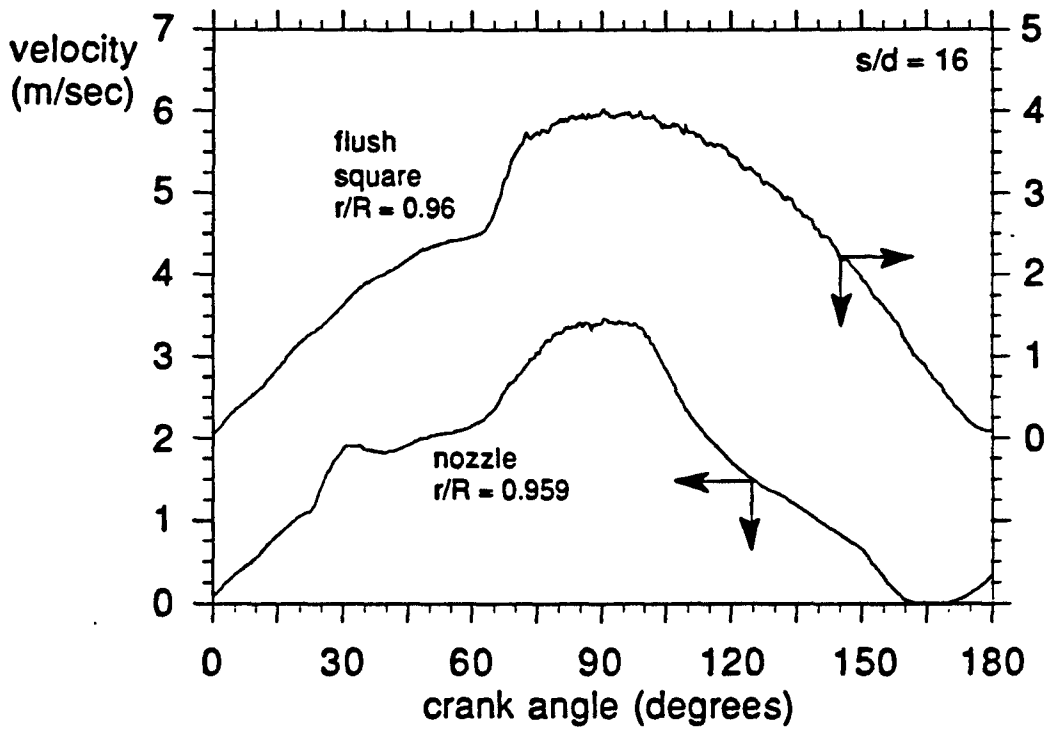

Figure 101: Near-wall ensemble-averaged velocity at s/d = 16.

Further downstream, at s/d = 30, the influence of inlet geometry is less pronounced since the boundary layer is unstable and undergoes transition for both cases. Traces of velocity fluctuation in the near-wall (r/R = 0.96 for the flush square, r/R = 0.970 for the nozzle; flush square offset by 0.35 m/sec) are nearly identical (Fig. 104), as high levels of fluctuation persist through flow reversal. In the core (Fig. 105), both cases experience

damping of the very low levels of fluctuation throughout most of the acceleration phase. Note that the nozzle is offset by 0.35 m/sec and that the flush square data and nozzle data are based on 50 cycles and 500 cycles of ensemble averaging, respectively. The fluctuations for the flush square inlet decrease gradually as the flow decelerates, although the high level of turbulent activity persists through flow reversal. Fluctuation levels for the nozzle inlet case appear to drop off more rapidly to a local minimum around 135°, beyond which the increasingly strong adverse pressure gradient seems to destabilize the flow, boosting the production of turbulence.

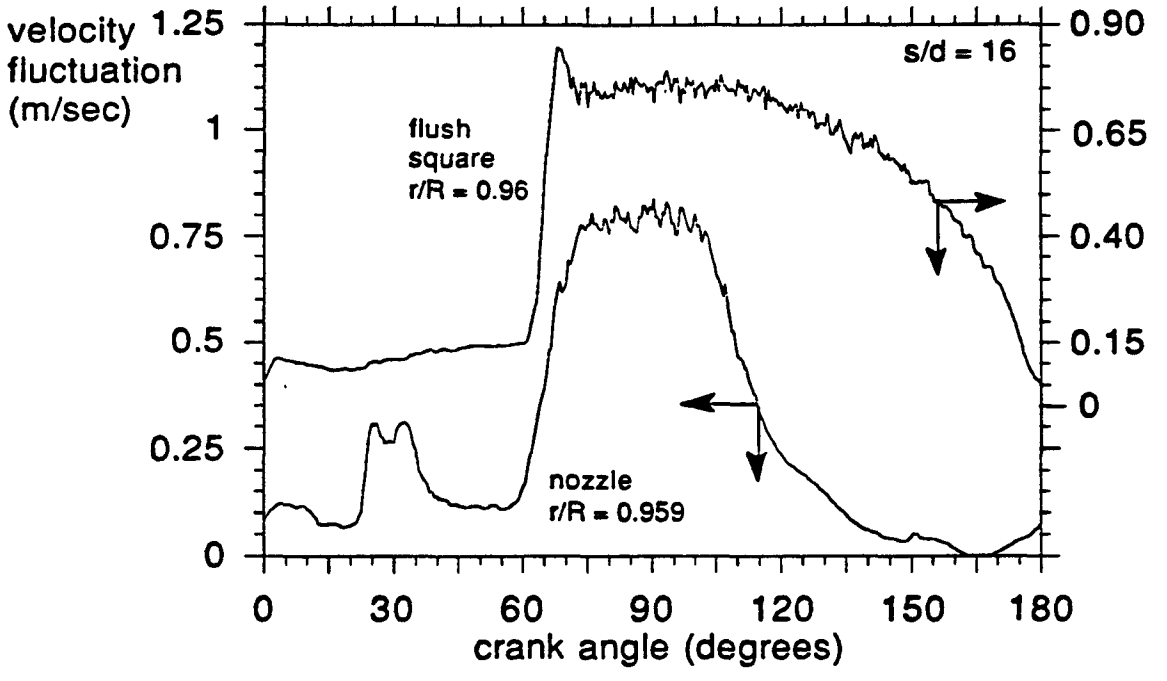

Figure 102: Near-wall velocity fluctuation at s/d = 16.

At the s/d = 44 station, the transition process is similar to that which occurs at s/d = 30, as reflected in near-wall (r/R = 0.977 for the nozzle, r/R = 0.96 for the flush square) and centerline traces of streamwise velocity fluctuation (Figs. 106 and 107). Note that the flush square trace is offset by 0.35 m/sec in Figure 106, and the nozzle trace is offset 0.3 m/sec in Figure 107. Measurements for both inlet geometries exhibit high levels of turbulent fluctuation through flow reversal.

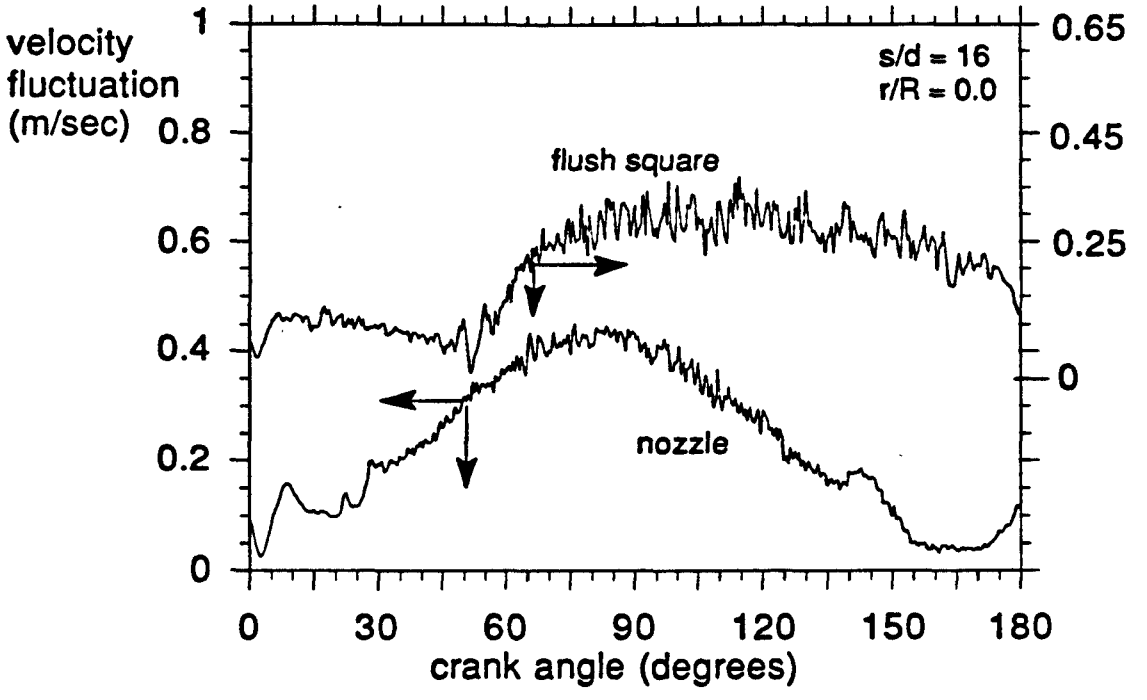

Figure 103: Centerline velocity fluctuation at s/d = 16

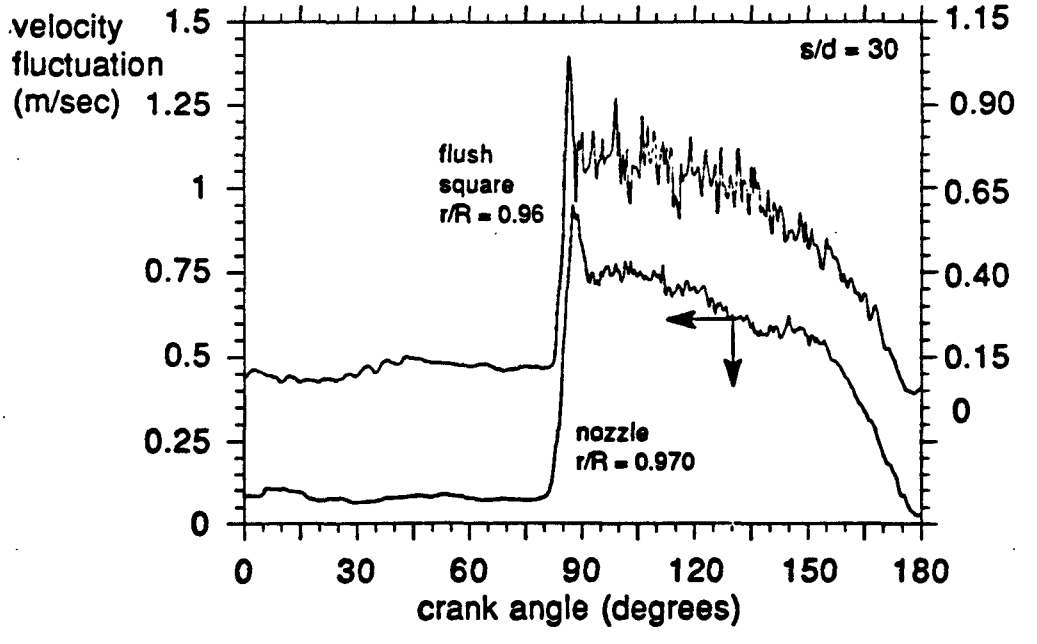

Figure 104: Near-wall velocity fluctuation at s/d = 30

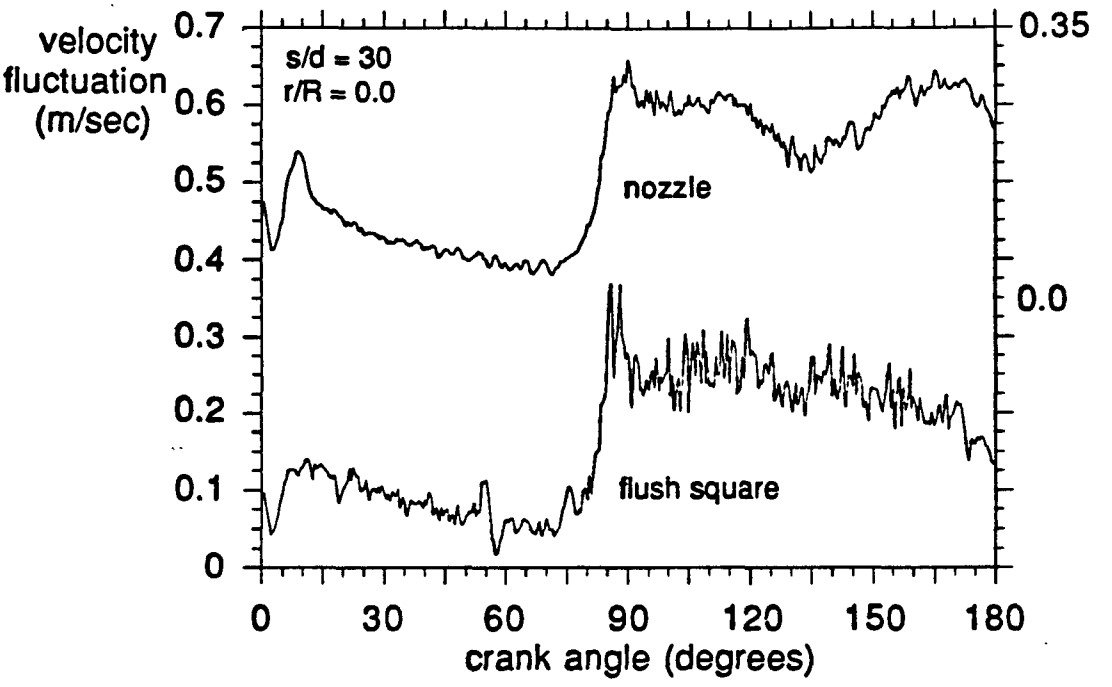

Figure 105: Centerline velocity fluctuation at s/d = 30

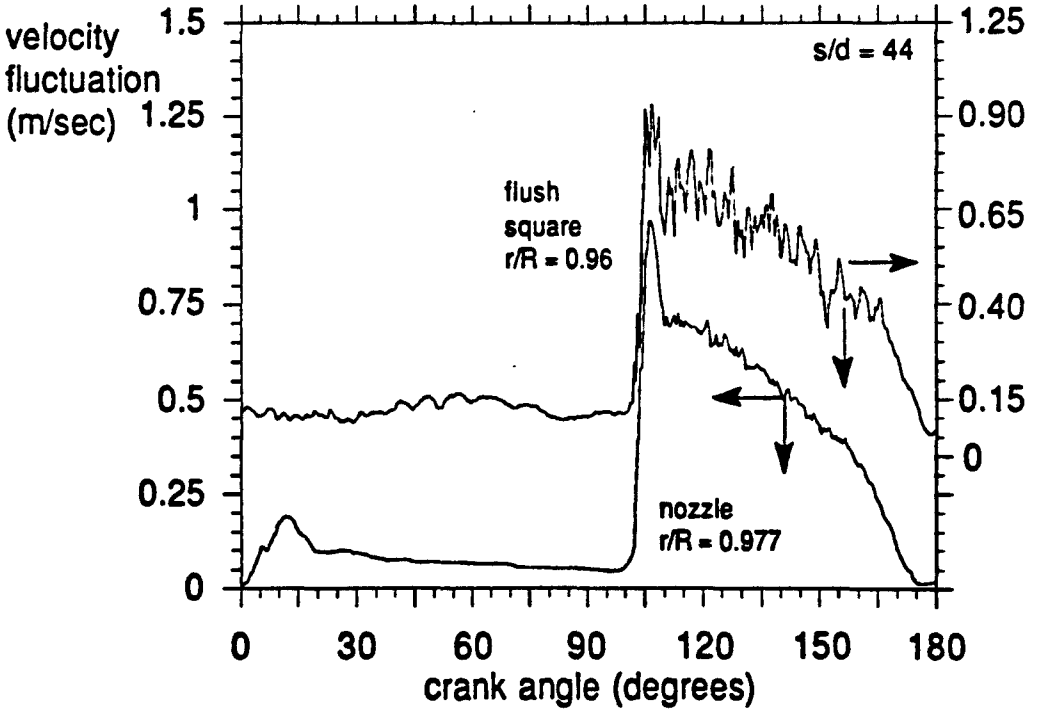

Fig. 106: Near-wall velocity fluctuation at s/d = 44

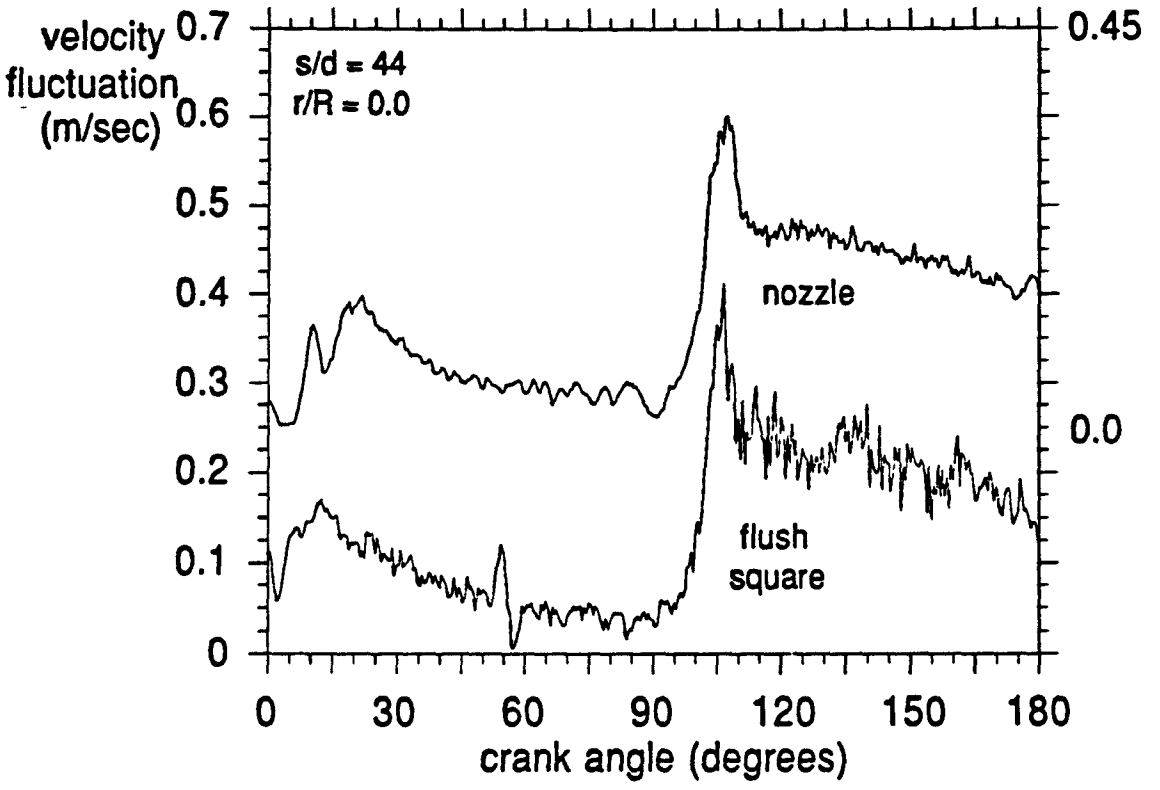

Figure 107: Centerline velocity fluctuation at s/d = 44

4. Conclusions

The observations of transition from the first part of this study are summarized in Figure 108. Laminar flow throughout the cycle was detected in the lower part of the operating regime (cases n, o, p), which is consistent with previous studies of transition discussed in section 3.2.

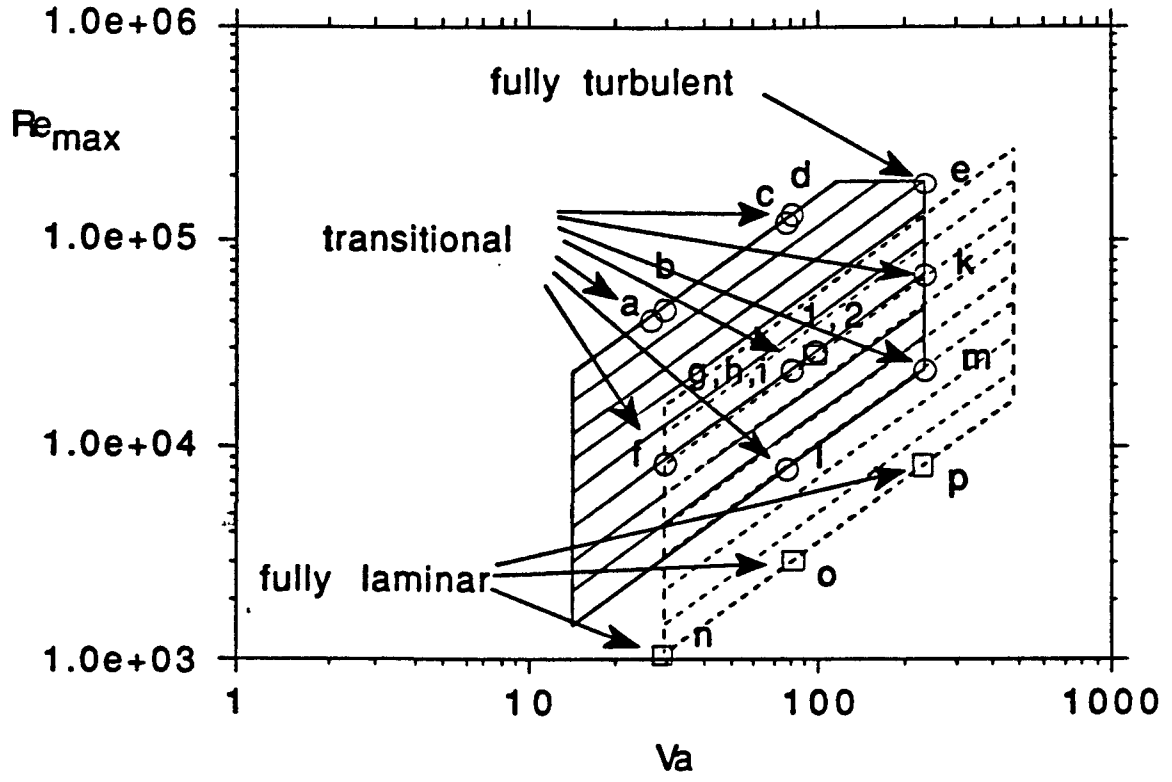

Figure 108: Operating Points Investigated and Conclusions Drawn from the Initial Transition Study

Transition to turbulent-like flow in each cycle was found in the remainder of the parameter range explored, excluding case e. This transition is either ...

(1) ... due to transition in a growing boundary layer. This event takes place either prior to the arrival of ingested turbulence or following in the low-turbulence flow behind the ingested turbulent slug (if the slug did not trip transition); or it is ...

(2) ... due to that turbulent fluid which resided outside the pipe during flow reversal and entered the pipe after flow reversal.

If both mechanisms are present, two steps of transition are observed: first, the boundary layer undergoes transition; then, the incoming turbulent fluid further increases turbulent activity.

Once the incoming turbulent fluid has triggered transition, the flow may remain turbulent or it may revert to its laminar state, as happens in case f, throughout the pipe. From the present results, it appears that the flow near the inlet and at lower values of Re_{max} tends to revert to the laminar state after the turbulent fluid has passed.

These cases from the present study raise questions about the circumstances under which the flow reverts to the laminar state, once turbulent incoming fluid has passed. The

behavior of boundary layers that are periodically subjected to strong free-stream disturbances (bypass transition – Morkovin (1978)) is currently being investigated by several researchers. These studies are motivated by the need to understand transition in gas turbine cascades. Here, the boundary layers on the blades/vanes are periodically disturbed by vortices and wakes being shed by the upstream vanes/blades. A comparison with models presently being developed in this area for predicting the response of the boundary layer to passing fluid of high turbulent kinetic energy levels was made herein and appears to be quite successful.

In case e, the fluid remained turbulent throughout the cycle, but there were in-cycle variations of velocity fluctuation. Perhaps, a quasi-turbulent behavior can be assumed but the level of turbulent kinetic energy of the incoming fluid must be taken into account.

In the case where transition occurred before the arrival of the turbulent slug, a transition criterion was not developed. Models developed for steady flows with spatially-varying pressure gradients, such as that applied herein to the SPRE operating point data, may be fruitful. This mode of transition was observed infrequently in the present study but would become prominent if the tube AR values were larger.

A transition criterion for the case in which the flow is convectively triggered, was developed. Turbulent kinetic energy is advected from the pipe entrance and triggers transition as it moves through the pipe. With good approximation, it may be assumed to move at the bulk-mean velocity. In long tubes, it becomes evident that the core-fluid which advects the turbulent kinetic energy actually moves faster due to the blockage of the tube cross-section by the boundary-layer. While the near-wall fluid moves more slowly due to the lower convection velocities there. This transition time within the cycle depends on the amplitude of the fluid motion, the length of the tube, and the position of interest within the tube. It may occur any time during the cycle; but, if it does not occur during the strong acceleration phase of the cycle, it will probably be preceded by transition of the boundary layer. Such a model for transition via the advected turbulent slug has been incorporated in GLIMPS (Gedeon, 1990). It was applied to the SPRE data set herein and found to be rather successful.

A second phase of the experimental investigation consisted of a detailed study at a single operating point, the SPRE operating point. Based on this work, the following confirmations and conclusions can be drawn about the flow:

- Whether the flow undergoes transition or merely experiences a passing disturbance is a function of both the natural development of the boundary layer and the advection of turbulence introduced to the test section through the inlet

- The inlet geometry strongly influences flow conditions downstream. For the nozzle inlet, separation upon outflow forms large-scale eddies which are advected during inflow, while a flush-square geometry continuously feeds turbulence to the boundary layer
- The anisotropy of the flow is strongly influenced by the stabilizing and destabilizing effects of the temporally-varying pressure gradient, the damping effect of the wall, the straining effect of the nozzles, amplification in the boundary layer, and the structure of advected turbulence
- Lower inertia near-wall flow responds more readily to an imposed pressure gradient than does the core flow
- Acceleration is stabilizing, reducing fluctuation levels, whereas deceleration destabilizes, boosting production.

These detailed data for the SPRE operating point flow will serve as comparison data for evaluating the performance of computational models.

Comparisons of correlation values for steady, fully-developed tube flow skin friction to measured values show considerable error in the laminar regime (where profile development is immature) but a surprisingly good correlation is found in the turbulent regime. Application of these correlations with a boundary-layer-type transition model was shown to be quite successful.

Important topics for upcoming experimental work include the continuation of a hot-wire investigation of the influence of inlet geometry on transition and the structure of the flow, a flow visualization study of the separation zone immediately downstream of the flush-square inlet and oscillating flow heat transfer.

5. References

Ahn, K.H., and Ibrahim, M. (1991): Private communication and submission of computational results. Institute for Computational Mechanics in Propulsion. Cleveland: NASA Lewis Research Center.

Akhavan, R., Kamm, R.D. and Shapiro, A.H. (1991a): An Investigation of Transition to Turbulence in Bounded Oscillatory Stokes Flows, Part 1, Experiments. Journal of Fluid Mechanics, Vol. 225, pp. 395-422.

Akhavan, R., Kamm, R.D. and Shapiro, A.H. (1991b): An Investigation of Transition to Turbulence in Bounded Oscillatory Stokes Flows, Part 2, Numerical Simulations. Journal of Fluid Mechanics, Vol. 225, pp. 423-444.

Bhatia, J.C., Durst, F., and Jovanovic, J. (1982): Corrections of hot-wire anemometer measurements near walls. Journal of Fluid Mechanics, Vol. 122, pp. 411-431.

Cayzac, R., Fauchas, J., and Clarion, C. (1985): Stability of unsteady parallel flows by the energy method. In: Kozlov, V.V. (ed.): Laminar-turbulent transition. 2nd IUTAM symposium on laminar-turbulent transition, Novosibirsk 1984. Berlin: Springer-Verlag.

Champagne, F.H., Sleicher, C.A., and Wehrmann, O.H. (1967): Turbulence Measurements with Inclined Hot-Wires. Journal of Fluid Mechanics, Vol. 28, part 1, pp. 153-175.

Davis, S. H. (1976): The Stability of Time-Periodic Flows.
In: VanDyke, M., Vincenti, W. and Wehausen, J. V. (eds.): Annual Review of Fluid Mechanics, Vol. 8, p. 57-74.

Dijkstra, K. (1984): Non-stationary Heat-transfer in Heat Exchangers. Proceedings of the 19th Intersociety Energy Conversion Engineering Conference, pp. 1888-1891. LaGrange, Il: American Nuclear Society.

Eckmann, D.M., and Grotberg, J.B. (1991): Experiments on Transition to Turbulence in Oscillatory Pipe Flow. Journal of Fluid Mechanics, Vol. 222, pp. 329-350.

Fox, R.W. and McDonald, A.T. (1978): Introduction to Fluid Mechanics. New York: Wiley.

Friedman, G.T. (1991): Experimental Investigation of Fluid Mechanics in Oscillatory Flow: A Detailed Study at a Single Operating Point. M.S. Thesis, University of Minnesota, Minneapolis, Minnesota, U.S.A.

Gedeon, D. (1990): GLIMPS, Version 3.0, User's Manual, Gideon Associates, 16922 South Canaan Road, Athens, OH 45701.

Grassmann, P., and Tuma, M. (1979): Kritische Reynolds-Zahlen bei Oszillierenden und Pulsierenden Rohrströmungen (Critical Reynolds Numbers in Oscillating and Pulsating Tube Flow; in German). Wärme- und Stoffübertragung, Vol. 12, p. 203-209.

Hino, M., Kashiwayanagi, M., Nakayama, A., and Hara, T. (1983): Experiments on the turbulence statistics and the structure of a reciprocating oscillatory flow. Journal of Fluid Mechanics, Vol. 131, pp. 363-400.

Hino, M., Sawamoto, M., and Takasu, S. (1976): Experiments on the Transition to Turbulence in an Oscillatory Pipe Flow. Journal of Fluid Mechanics, Vol. 75, Part 2, pp. 193-207.

Iguchi, M., Ohmi, M., and Maegawa, K. (1982): Analysis of Free Oscillating Flow in a U-shaped Tube. Nihon Kikaigakkai (Bulletin of the JSME), Vol.25, No. 207, pp. 1398-1405, September.

Kays, W.M., and Crawford, M.E. (1980): Convective Heat and Mass Transfer. New York: McGraw-Hill.

Kirmse, R.E. (1979): Investigation of Pulsating Turbulent Pipe Flow. Transactions of the ASME, Journal of Fluids Engineering, Vol. 101, pp. 436-442.

Kim, J. (1990): Freestream Turbulence and Concave Curvature Effects on Heated Transitional Boundary Layers. PhD Thesis, University of Minnesota.

Koester, G., Howell, S., Wood, G., Miller, E., and Gedeon, D. (1990): Oscillating Flow Loss Test Results in Stirling Engine Heat Exchangers. Sunpower, Inc. NASA CR-182288.

Köhler, W.J. (1990): Numerical Prediction of Turbulent Oscillating Flow and Associated Heat Transfer. Ph.D. Thesis, University of Minnesota, Minneapolis, Minnesota/USA.

Kurzweg, U.H. (1985): Enhanced heat conduction in oscillating viscous flows within parallel-plate channels. Journal of Fluid Mechanics, Vol. 156, pp. 291-300.

Laufer, J. (1953): The Structure of Turbulence in Fully Developed Pipe Flow. NACA Report 1174.

Mayle, R.E. (1991): The Role of Laminar-Turbulent Transition in Gas Turbine Engines, ASME Paper 91-GT-261, Presented at the International Gas Turbine and Aeroengine Congress and Exposition, Orlando, FL, June 1991.

Morkovin, M.V. (1978): Instability, Transition to Turbulence and Predictability, AGARDograph-AG-236.

Merkli, P. and Thomann, H. (1975): Transition to Turbulence in Oscillating Pipe Flow. Journal of Fluid Mechanics, Vol. 68, Part 3, pp. 567-575.

Ohmi, M., Iguchi, M., and Urahata, I. (1982): Flow Patterns and Frictional Losses in an Oscillating Pipe Flow. Nihon Kikaigakkai (Bulletin of the JSME), Vol. 25, No. 202, pp. 536-543, April.

Park, J., and Baird, M. (1970): Transition Phenomena in an Oscillating Manometer. Canadian Journal of Chemical Engineering, Vol. 48, pp. 491-495.

Richardson, E. G., and Tyler, E. (1929): The Transverse Velocity Gradient near the Mouths of Pipes in which an Alternating or Continuous Flow of Air is Established. Proc. Phys. Soc. London, Vol. 42, Part 1.

Schlichting, H. (1979): Boundary Layer Theory.
New York: McGraw-Hill.

Sergeev, S. (1966): Fluid Oscillations at Moderate Reynolds Numbers. Fluid Dynamics, Vol. 1, No. 1, pp. 121-122.

Sexl, T. (1930): Über den von E. G. Richardson entdeckten 'Annulareffekt'. Zeitschrift für Physik, Vol. 61, pp. 349-362.

Seume, J.R. (1988): An Experimental Investigation of Transition in Oscillating Pipe Flow. Dissertation. University of Minnesota, Minneapolis, Minnesota/USA.

Seume, J.R., and Simon, T.W. (1986): Oscillating Flow in Stirling Engine Heat Exchangers. Proceedings of the 21st Intersociety Energy Conversion Engineering Conference, pp.533-538.
Washington: American Chemical Society.

Seume, J.R., and Simon, T.W. (1988a): Flow Oscillation Effects in Tubes and Porous Material: Unresolved Issues.
In: Morel, T.E., Dudenhoefer, J.E., Uzkan, T., and P.J. Singh (eds.): Fluid Flow and Heat Transfer in Reciprocating Machinery. Proceedings, ASME Winter Annual Meeting, Boston, MA, December 1987. FED-Vol. 62, HTD-Vol. 93, pp. 55-62.
New York: American Society of Mechanical Engineers.

Seume, J.R., and Simon, T.W. (1988b): Effect of Transition on Oscillating Flow Losses in Stirling Engine Coolers and Heaters. Proceedings of the 23rd Intersociety Energy Conversion Engineering Conference. pp. 127-132.
New York: American Society of Mechanical Engineers.

Simon, T.W., and Seume, J.R. (1986): A Survey of Oscillating Flow in Stirling Engine Heat Exchangers. NASA Contractor Report 182108. Cleveland: Lewis Research Center.

Taylor, D.R., and Aghili, H. (1984): An investigation of oscillating flow in tubes. Proceedings of the 19th Intersociety Energy Conversion Engineering Conference. pp. 2033-2036.
American Nuclear Society.

Tew, R.C., Thieme, L.G., and Dudenhoefer, J.E. (1990): Recent Stirling Engine Loss-Understanding Results. Proceedings of the 25th IECEC, Reno, Nevada: Vol. 5, pp. 377-385.

Uchida, S. (1956): The Pulsating Viscous Flow Superposed on the Steady Laminar Motion of Incompressible Fluid in a Circular Pipe.
Zeitschrift für Angewandte Mathematik und Physik, Vol. 7, pp. 403-422.

Valensi, J. (1947): Oscillations d'un liquide pesant et visqueux dans un tube in U de faible diamètre. Comptes Rendus de la Académie des Sciences de Paris, Vol. 224, pp. 446, 532, 893 and 1695.

Vasiliev, O. F., and Kvon, V. I. (1971): Friction Forces of Unsteady Flows in Open Channels and Pipes. International Association for Hydraulic Research, Proceedings of the 14th Conference, Vol. I, Subject B.

Von Kerczek, C., and Davis, S. H. (1972): The Stability of Oscillatory Stokes Layers. Studies in Applied Mathematics, Vol. LI, No. 3.

White, F. M. (1974): Viscous Fluid Flow.
New York: McGraw-Hill.

Wills, J.A.B. (1962): The Correction of Hot-Wire Readings for Proximity to a Solid Boundary. Journal of Fluid Mechanics, Vol. 12, Part 3, pp. 388-396.

Wilson, D.J. (1970): An Experimental Investigation of the Mean Velocity, Temperature and Turbulence Fields in Plane and Curved Two-Dimensional Wall Jets: Coanda Effect. PhD Thesis, University of Minnesota.

Womersley, J. R. (1955): Method for the Calculation of Velocity, Rate of Flow and Viscous Drag in Arteries when the Pressure Gradient is Known. Journal for Physiology, Vol. 127, pp. 553-563.

APPENDIX A

I. Positions of Single-Wire Measurements

s/d = 0.33

y (inch)	y(mm)	r/R
0.0043	0.1092	0.994
0.0053	0.1346	0.993
0.0073	0.1854	0.990
0.0093	0.2362	0.988
0.0118	0.2997	0.984
0.0143	0.3632	0.981
0.0193	0.4902	0.974
0.0243	0.6172	0.968
0.0393	0.9982	0.948
0.0543	1.3792	0.928
0.1043	2.6492	0.861
0.2043	5.1892	0.728
0.3043	7.7292	0.594
0.4043	10.2692	0.461
0.5043	12.8092	0.328
0.6043	15.3492	0.194
0.7543	19.1592	- 0.006

s/d = 16

y (inch)	y(mm)	r/R
0.0037	0.0940	0.995
0.0057	0.1448	0.992
0.0127	0.3226	0.983
0.0307	0.7798	0.959
0.0457	1.1608	0.939
0.0957	2.4308	0.872
0.1957	4.9708	0.739
0.2957	7.5108	0.606
0.3957	10.0508	0.472
0.4957	12.5908	0.339
0.5957	15.1308	0.206
0.7457	18.9408	0.006

s/d = 30

y (inch)	y(mm)	r/R
0.0026	0.0660	0.997
0.0036	0.0914	0.995
0.0066	0.1676	0.991
0.0106	0.2692	0.986

s/d = 44

y (inch)	y(mm)	r/R
0.0006	0.0152	0.999
0.0016	0.0406	0.998
0.0036	0.0914	0.995
0.0056	0.1422	0.993

0.0126	0.3200	0.983	0.0076	0.1930	0.990
0.0176	0.4470	0.977	0.0126	0.3200	0.983
0.0226	0.5740	0.970	0.0176	0.4470	0.977
0.0376	0.9550	0.950	0.0476	1.2090	0.937
0.0526	1.3360	0.930	0.0976	2.4790	0.870
0.1026	2.6060	0.863	0.1976	5.0190	0.737
0.2026	5.1460	0.730	0.2976	7.5590	0.603
0.3026	7.6860	0.597	0.3976	10.0990	0.470
0.4026	10.2260	0.463	0.4976	12.6390	0.337
0.5026	12.7660	0.330	0.5976	15.1790	0.203
0.6026	15.3060	0.197	0.7476	18.9890	0.003
0.7526	19.1160	0.004			

* An r/R < 0 represents a radial position beyond the centerline (0.75 inch)

II. Positions of Cross-wire Measurements

s/d = 0.33, 16, 30, and 44

y (inch)	y(mm)	r/R
0.150	3.81	0.800
0.200	5.08	0.733
0.300	7.62	0.600
0.400	10.16	0.467
0.500	12.70	0.333
0.600	15.24	0.200
0.750	19.05	0.000

APPENDIX B

UNCERTAINTY DOCUMENTATION

I. Wall distance

As discussed in Section 4.1, the wall-finding process consists of the following steps:

(1) Positioning the probe by visual means
(2) Ensemble averaging over fifty cycles and extrapolating near-wall profiles to the wall

The uncertainty in wall position which remains after step 1 is 0.127 mm (0.005 inch). The residual uncertainty which remains after step 2 is 0.025 mm (0.001 inch). The latter is the standard deviation of the y-intercepts computed from near-wall velocity profiles, as detailed in Section 8.1. Minimum and maximum y-intercepts were also determined from the near-wall profiles for later use in defining the range of uncertainty in skin-friction coefficient.

II. Velocity

The uncertainty in velocity is attributable to both calibration and data acquisition uncertainties. The sensitivity analyses are performed for a nominal velocity of 3 m/sec at standard temperature and pressure.

Calibration uncertainties:

(1) The uncertainty of the micromanometer scale readings, used to determine the static pressure, and hence, the dynamic pressure, is 0.0254 mm (0.001 inch) of water.

$$dh = 0.001 \text{ inch of water}$$

The sensitivity of velocity to the micromanometer readings is:

$$\left(\frac{\delta u}{\delta h}\right) = 660 \ \frac{\text{m/sec}}{\text{inch of water}}$$

(2) The uncertainty associated with the reading of the ambient air pressure from a barometer is 0.249 Pa (0.001 bar).

$dp = 0.249$ Pa

The sensitivity of velocity to the barometer readings is:

$$\left(\frac{\delta u}{\delta p}\right) \doteq 0 \quad \text{(negligible)}$$

(3) The uncertainty associated with the reading of the ambient temperature from a thermometer is 0.1°C.

$dT = 0.1°C$

The sensitivity of velocity to the temperature readings is:

$$\left(\frac{\delta u}{\delta T}\right) \doteq 0 \quad \text{(negligible)}$$

(4) The uncertainty in angular alignment of the probe in the calibration jet is approximately 1°. A test of angular alignment demonstrated that, for angles within ±2° of alignment, a 0.1% change in voltage is measured for a misalignment of 1°.

$d\theta = .1°$

The sensitivity of velocity to the angular alignment is:

$$\left(\frac{\delta u}{\delta \theta}\right) = 0.0375 \frac{m/sec}{°}$$

Data Acquisition uncertainties:

(1) The uncertainty in angular frequency is 0.0113 sec^{-1}, corresponding to a ±2% variation in ω during the cycle.

$d\omega = 0.0113\ sec^{-1}$

The sensitivity of velocity to angular frequency is:

$$\left(\frac{\delta u}{\delta \omega}\right) = 5.333 \frac{\text{m/sec}}{\text{sec}^{-1}}$$

(2) The uncertainty in angular alignment of the probe in the test section is approximately 1°. Applying the same test as mentioned above for the calibration jet alignment, a 0.1% change in voltage is measured for a misalignment of 1°.

$$d\theta = 1°$$

The sensitivity of velocity to the angular alignment is:

$$\left(\frac{\delta u}{\delta \theta}\right) = 0.0375 \frac{\text{m/sec}}{°}$$

The cumulative uncertainty is:

$$du = \left[\left(\left(\frac{\delta u}{\delta h}\right) dh\right)^2 + \left(\left(\frac{\delta u}{\delta \theta}\right) d\theta\right)^2 + \left(\left(\frac{\delta u}{\delta \omega}\right) d\omega\right)^2 + \left(\left(\frac{\delta u}{\delta \theta}\right) d\theta\right)^2 \right]^{0.5}$$

$$du = 0.665 \text{ m/sec}$$

The uncertainty introduced by the micromanometer reading dominates the cumulative uncertainty in velocity.

III. Skin-friction coefficient

The uncertainty in skin-friction coefficient arises from three sources, the uncertainty in wall distance, the uncertainty in velocity, and the uncertainty associated with fitting the experimental data to models of Couette flow.

(1) The uncertainty in wall position is 0.025 mm (0.001 inch).

$$dy = 0.025 \text{ mm}$$

The sensitivity of skin-friction coefficient to wall position is:

$$\left(\frac{\delta c_f}{\delta y}\right) = 0.02939 \text{ mm}^{-1}$$

(2) The uncertainty in velocity is 0.665 m/sec.

$du = 0.665$ m/sec

The sensitivity of skin-friction coefficient to velocity is:

$$\left(\frac{\delta c_f}{\delta u}\right) = 0.0005 \text{ (m/sec)}^{-1}$$

(3) A representative uncertainty in u_* associated with fitting the data to the turbulent model is 0.004 m/sec.

$du_* = 0.004$ m/sec

The sensitivity of skin-friction coefficient to the fitting process is:

$$\left(\frac{\delta c_f}{\delta u_*}\right) = 0.1299 \text{ (m/sec)}^{-1}$$

The cumulative uncertainty in skin-friction coefficient is:

$$dc_f = \left[\left(\left(\frac{\delta c_f}{\delta y}\right) dy\right)^2 + \left(\left(\frac{\delta c_f}{\delta u}\right) du\right)^2 + \left(\left(\frac{\delta c_f}{\delta u_*}\right) du_*\right)^2 \right]^{0.5}$$

$$dc_f = 0.00096$$

This uncertainty corresponds to an average uncertainty of 11% for c_f values in the turbulent-like flow regime. Similar analysis for the laminar-like flow regime leads to an uncertainty, $dc_f = 0.00084$, corresponding to an average uncertainty of 12% for c_f.

REPORT DOCUMENTATION PAGE

Form Approved
OMB No 0704-0188

1. AGENCY USE ONLY (*Leave blank*)	2. REPORT DATE	3. REPORT TYPE AND DATES COVERED
	March 1992	Final Contractor Report

4. TITLE AND SUBTITLE

Fluid Mechanics Experiments in Oscillatory Flow
Volume I–Report

5. FUNDING NUMBERS

WU–590–13–11
G–NAG3–598

6. AUTHOR(S)

J. Seume, G. Friedman, and T.W. Simon

7. PERFORMING ORGANIZATION NAME(S) AND ADDRESS(ES)

University of Minnesota
Dept. of Mechanical Engineering
Minneapolis, Minnesota 55455

8. PERFORMING ORGANIZATION REPORT NUMBER

None

9. SPONSORING/MONITORING AGENCY NAMES(S) AND ADDRESS(ES)

National Aeronautics and Space Administration
Lewis Research Center
Cleveland, Ohio 44135–3191

10. SPONSORING/MONITORING AGENCY REPORT NUMBER

NASA CR–189127

11. SUPPLEMENTARY NOTES

Project Managers, Roy C. Tew and James E. Dudenhoefer, Power Technology Division, NASA Lewis Research Center, (216) 433–8471.

12a. DISTRIBUTION/AVAILABILITY STATEMENT

Unclassified - Unlimited
Subject Category 34

12b. DISTRIBUTION CODE

13. ABSTRACT (*Maximum 200 words*)

Results of a fluid mechanics measurement program in oscillating flow within a circular duct are presented. The program began with a survey of transition behavior over a range of oscillation frequency and magnitude and continued with a detailed study at a single operating point. Such measurements were made in support of Stirling engine development. Values of three dimensionless parameters, Re_{max}, Re_w, and A_R, embody the velocity amplitude, frequency of oscillation and mean fluid displacement of the cycle, respectively. Measurements were first made over a range of these parameters which included operating points of all Stirling engines. Next, a case was studied with values of these parameters that are representative of the heat exchanger tubes in the heater section of NASA's Stirling cycle Space Power Research Engine (SPRE). Measurements were taken of the axial and radial components of ensemble-averaged velocity and rms-velocity fluctuation and the dominant Reynolds shear stress, at various radial positions for each of four axial stations. In each run, transition from laminar to turbulent flow, and its reverse, were identified and sufficient data was gathered to propose the transition mechanism. Models of laminar and turbulent boundary layers were used to process the data into wall coordinates and to evaluate skin friction coefficients. Such data aids in validating computational models and is useful in comparing oscillatory flow characteristics to those of fully-developed steady flow. Data were taken with a contoured entry to each end of the test section and with flush square inlets so that the effects of test section inlet geometry on transition and turbulence are documented. The following is presented in two volumes. Volume I contains the text of the report including figures and supporting appendices. Volume II contains data reduction program listings and tabulated data (including its graphical presentation).

14. SUBJECT TERMS	15. NUMBER OF PAGES
Fluid mechanics; Oscillating flow; Stirling engines	160
	16. PRICE CODE: A08

17. SECURITY CLASSIFICATION OF REPORT	18. SECURITY CLASSIFICATION OF THIS PAGE	19. SECURITY CLASSIFICATION OF ABSTRACT	20. LIMITATION OF ABSTRACT
Unclassified	Unclassified	Unclassified	